Trigger Development with dijet veto at $\sqrt{s} = 13\,TeV$ for the CMS experiment

Basile Vermassen

Promoter: Prof. Didar Dobur
Supervisor: Willem Verbeke, Dr. Tom Cornelis

Master's dissertation submitted in order to obtain the academic degree of Master of Science in Engineering Physics

Vakgroep Fysica en Sterrenkunde
Chair: Prof. dr. Dirk Ryckbosch
Faculty of Engineering and Architecture
Academic year 2016-2017

GHENT
UNIVERSITY

Acknowledgements

I would like to thank a few people without whom I would never have gotten to this point. Firstly and foremost, prof. Didar Dobur for giving me the opportunity to work on a subject that truly interests and inspires me. I want to thank you for your guidance and your active involvement in my thesis over the past year. It has been a marvelous experience being part of this research group and the CERN community and I have you to be grateful for.

A proper thanks is also in place for Willem Verbeke, who helped me a lot by answering my questions, being available for discussion and providing great insights on many occasions. And a big thank you for proof-reading my thesis.

Thanks to Laurent Thomas and Tom Cornelis for answering my questions or making time for me when I was stuck on something. It means a lot to me.

Finally, I want to thank Laurens, Giel, Benoît, Wannes and Jorne for the many moments that made the past year that much more enjoyable.

Contents

List of Figures

List of Tables

Chapter 1

Introduction

The Standard Model (SM) of particle physics combines our present knowledge of nature at its most fundamental level. All of its predictions have been experimentally verified, proving it to be a successful and consistent theory. The recent discovery of a scalar boson matching the properties of the Higgs boson[10, 11] provided the final piece to the puzzle, making it a fully coherent theory. But despite its successes, the SM is far from a complete theory of nature. Several existing problems find no satisfying answer. It is therefore imperative to keep searching for new physics beyond the SM.

One of the most compelling questions is the nature of neutrinos. While all other fundamental particles have Dirac nature, meaning they are distinguishable from their anti-particle, there is no conclusive evidence that neutrinos possess this nature as well. It is equally probable that neutrinos are Majorana particles, thus being their own anti-particle. This scenario is appealing since it would solve the problem of the neutrino masses, which originated with the observation of neutrino oscillations by the SNO[1] and Kamiokande[2] experiments. Experiment confines the masses to below the eV scale however, and consequently the coupling constant from Dirac-Yukawa coupling would be unnaturally small. The Majorana nature provides a much more elegant mechanism. By introducing one or more sterile potentially heavy Majorana neutrinos, the coupling constants can be reduced to more natural values through the seesaw mechanism. Being sterile, these particles would only interact with the SM by mixing with the other neutrinos, thus being very hard to detect.

This thesis is carried out as part of the Majorana neutrino analysis performed by the Ghent experimental particle physics group, in close collaboration with the CMS experiment at the Large Hadron Collider (LHC) in CERN, Geneva [3]. The LHC is a particle accelerator and collider complex, designed to perform measurements of proton-proton collisions at unprecedented energies. Their goal is to solve the mysteries still surrounding the fundamental structure of our universe. The CMS experiment constitutes one of the four detectors around the LHC. This thesis is carried out using data from the CMS detector.

In the next chapter, we begin by explaining the basic principles of the SM. It is the underlying theory for the remainder of the dissertation. Then the seesaw mechanism, a possible extension of the SM, is explained. The technicalities of the LHC and CMS follow next. They detail the beam properties, the detector layout and the triggers, a relevant subject for this thesis. The Heavy Neutral Lepton search strategy is laid out. This gives a brief overview of the framework in which the trigger study of this thesis is performed. The last two chapters detail the work done by the writer of this dissertation. A trigger study is performed where a new concept trigger is analyzed and lastly, the triggers of the Majorana neutrino analysis are studied in detail.

Chapter 2

The Standard Model of Particle Physics

This chapter details the core concepts of the SM of particle physics [4]. A first section is dedicated to the fundamental particles that appear in nature. After that, the theory is explained. The SM incorporates the electromagnetic, weak and strong interactions in a comprehensive theory, conventionally expressed in the Lagrangian formalism. The electroweak unification and the Brout-Englert-Higgs(BEH) mechanism are discussed, as well as the Yukawa coupling of the Higgs field to the fermions. This immediately introduces a problem relevant to this thesis, namely the extremely small masses of neutrinos. Chapter 3 presents an in-depth discussion of the seesaw mechanism, an elegant solution to this problem.

2.1 Fundamental Particles

The concept that the world around us is constructed out of tiny indivisble building blocks can be traced back all the way to ancient Greece. The philosopher Democritus already toyed with the idea of an atomic theory in the 5th century BC. But it would have to wait until the beginning of the 19th century before John Dalton gathered the empirical evidence from which he could conclude that matter consisted of identical indivisible particles, then known as 'chemical elements'. As technology advanced, experiments grew more elaborate and managed to show that these elements were not fundamental but consisted of an internal structure of smaller particles. The trend was set and physicists began to probe ever deeper into the fundamental structure of matter. The culmination of all this work resulted in the Standard Model of particle physics, which consists of 12 distinct matter particles, 4 distinct 'force carrying' particles, and one particle related to the origin of mass, the Higgs Boson (Figure 2.1).

2.1.1 The matter particles

All fundamental particles that are considered to be 'matter' are fermions, meaning they always have half-integer spin and satisfy Pauli's exclusion principle. The matter particles

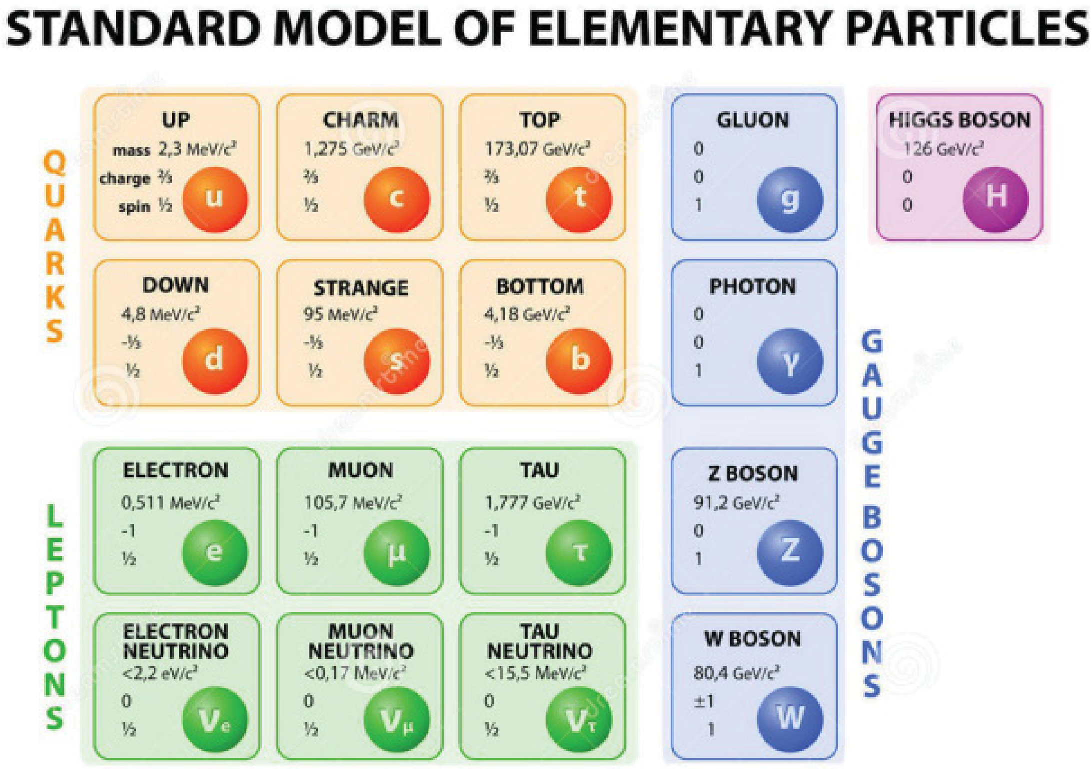

Figure 2.1: The fundamental particles of the standard model.

can be subdivided in 2 categories according to their properties, quarks and leptons. There are 6 quark flavours and 6 lepton flavours. When referring to a specific type of particle, the term flavour is used, e.g. an up and down quark have different flavour. Both quarks and leptons can be categorized further into 3 generations of paired particles. The first generation quarks are the up (u) and down (d) quarks, respectively the lightest and most stable quarks. The second generation quarks are the strange (s) and charm (c) quark and the third are the bottom (b) and top (t) quarks. The mass of these particles increases rapidly with each generation. As a result, they are decreasingly stable and have very short lifetimes. A similar scenario is true for the leptons. Each generation consists of a lepton and a corresponding neutrino. This gives in order of increasing mass the electron (e), the muon (μ) and the tau (τ), with respectively the electron-, muon- and tau-neutrino. The statement that mass increases across generations does not really apply to neutrinos, because their mass eigenstates and flavour eigenstates are heavily mixed. Moreover, their masses are extremely small compared to the other SM fermions. The peculiar case of neutrinos is discussed in-depth further on.

2.1.2 The fundamental interactions

Particles interact with each other through four fundamental interactions or forces. The matter particles transfer energy by 'emitting and absorbing' force-carrying particles. Different forces are relevant at different energy and length scales.

The weakest interaction is gravity by several orders of magnitude, but it is contradictorily the most important force at large scale. The solar system, galaxies and most astronomical phenomena are entirely governed by gravity. This is explained by gravity being a purely attractive force for all particles with mass, resulting in constructive behavior everywhere. Its force-carrying particle, the gravition, is hypothesized to exist but has never been observed by experiment. Gravity is the only one of the four interactions that is not described by the SM. It appears to be very difficult to reconcile the general theory of relativity, which governs the large scale behavior of gravity, with quantum field theory at the smallest scale [5]. Being so weak compared to the other interactions, it can be neglected completely in high energy physics experiments. But this is a mixed blessing, as consequently it is very hard to study gravity in these experiments the same way the other forces are studied [6].

For the three other interactions a successful theory has been built and their force-carrying particles have been experimentally verified to exist. Unlike the matter particles, the force-carriers are all bosons, which have integer spin and do not have to satisfy Pauli's exclusion principle. First off, the electromagnetic interaction can act, like gravity, over an infinite distance. Its corresponding particle is the photon, a massless boson. Except for neutrinos that have no charge for the electromagnetic interaction, all SM fermions carry charge and interact through this force. The weak interaction is weaker than the electromagnetic at low energy interactions, although it becomes comparable in strength for high energy processes. All matter particles interact weakly. The corresponding force-carriers are the Z, W^+ and W^- bosons. They are all massive, which explains why this interaction is weak as it takes a lot of energy to produce these massive particles. The corresponding charge is the weak isospin. Finally the strong interaction remains, a force that only couples to the quarks. As its name suggests, it is a lot stronger than the other forces. It couples to a quantity called colour. Every flavour of quarks appears in 3 distinct colours; red, green and blue. As a result of the nature and strength of this interaction, quarks are never stable as a single, bare quark . They always appear in bound, colourless combinations e.g. mesons consisting of a quark and anti-quark or baryons consisting of three quarks. The force-carries are the massless gluons.

The final particle that completes the SM is the Brout-Englert-Higgs particle, or Higgs boson [7, 8]. It is a boson just like the photon, gluon, Z and W. But while these all have spin 1, the Higgs boson has spin 0, making it the only scalar particle in the entire SM. The Higgs boson is a result of the presence of the Higgs field, an interaction field that is responsible for the mass of the W and Z bosons and the fermions. The BEH mechanism is explained further on in this chapter. The Higgs boson was the final SM particle to be discovered. In july of 2012, the CMS and ATLAS experiments at the LHC, CERN in

Geneva [10, 11] presented evidence of its existence. The LHC continues to investigate the properties of this unique particle.

2.2 Quantum Field Theory

Quantum Field Theory (QFT) [14] constitutes the quantized version of classical field theory. It is the framework in which the SM is expressed. The particles are no longer the fundamental objects, but merely excitations of their respective fields, building further on the concept of probability density functions from classical quantum mechanics. QFT combines quantum mechanics and the principles of special relativity. This means time and space are treated on equal footing, as coordinates, which was a problem for classical quantum mechanics, where time was merely a parameter and was not treated equal to the spatial dimensions. Quantum mechanics is a nonrelativistic theory, neatly illustrated by the time-dependent Schrödinger equation

$$i\hbar\frac{\partial}{\partial t}\left|\psi(\mathbf{r},\mathbf{t})\right\rangle = \hat{H}\left|\psi(\mathbf{r},\mathbf{t})\right\rangle = \left[-\frac{\hbar^2}{2\mu}\nabla^2 + V(\mathbf{r},\mathbf{t})\right]\psi(\mathbf{r},\mathbf{t}) \tag{2.1}$$

which is not Lorentz-invariant. This can easily be shown. The hamiltonian $\hat{H}$ represents the total energy of the system and for a free particle, the resulting kinetic energy is equal to $E = p^2/2m$. The correct relativistic expression for the energy of a free particle is however $E = \sqrt{p^2c^2m^2c^4}$. The non-relativistic approach remains valid as long as low energy excitations are considered. But in subatomic physics, the energies are of a scale where a relativistically valid theory is absolutely necessary. This is provided by quantum field theory.

The simplest example of a field is the Klein-Gordon field, representing relativistic particles of spin 0 and mass m. The Klein-Gordon field expression was derived from Einstein's energy-momentum relation:

$$E^2 = \mathbf{p}^2c^2 + m^2c^4 \tag{2.2}$$

If we regard these quantities as operators, it is possible to constitute an equation for a single scalar wavefunction $\phi(x)$ (where $x = (\mathbf{x}, t)$). The expressions for energy and momentum operators in coordinate space are $\mathbf{p} \to -i\hbar\nabla$ and $E \to i\hbar\partial/\partial t$ which gives

$$\left(\Box + \mu^2\right)\phi\left(x\right) = 0 \tag{2.3}$$

using the d'Alembertian symbol $\Box = \partial^\mu\partial_\mu$. It is important not to look at this as a single particle equation, but as a dynamical equation for the Klein-Gordon field, an unphysical field [15] that is just used as an example. The corresponding particles can be found through the mechanism of canonical quantization, which will be shortly discussed for the Dirac equation.

The Lagrangian formalism is an elegant way to start writing down a field theory. Based on the principle of least action, it allows for a compact and straightforward interpretation of the theory. A Lagrangian density is introduced that depends only on the fields and their derivatives

$$\mathcal{L} = \mathcal{L}\left(\phi, \partial_\alpha \phi\right) \tag{2.4}$$

For an arbitrary region Ω of the four dimensional space-time continuum, the action $S\left(\Omega\right)$ can now be defined as the four dimensional integral of the Lagrangian density over Ω

$$S\left(\Omega\right) = \int_\Omega d^4x \mathcal{L}\left(\phi, \partial_\alpha \phi\right) \tag{2.5}$$

The variational principle dictates that the action will be minimized when the variation δS is zero for all variations of the field $\delta\phi$ and $\delta\partial_\alpha\phi$. Boundary conditions are necessary, saying that the variation vanishes on the boundary of the region: $\delta\phi = 0$ on $\delta\Omega$. Variation of the action gives, after some calculation:

$$\delta S\left(\Omega\right) = \int_\Omega d^4x \left[\frac{\partial \mathcal{L}}{\partial \phi} - \frac{\partial}{\partial^\alpha}\frac{\partial \mathcal{L}}{\partial \partial_\alpha \phi}\right]\delta\phi + \int_\Omega d^4x \frac{\partial}{\partial^\alpha}\left(\frac{\partial \mathcal{L}}{\partial \partial_\alpha \phi}\delta\phi\right) \tag{2.6}$$

The second term can be converted into a surface integral over $\delta\Omega$ using Gauss's divergence theorem. The boundary conditions then tell that this term will not contribute anywhere. The variation of the action has to be zero for all variations $\delta\phi$. As a consequence the integrand of the remaining integral is required to be zero, resulting in the Lagrangian equation of motion

$$\frac{\partial \mathcal{L}}{\partial \phi} - \frac{\partial}{\partial_\alpha}\frac{\partial \mathcal{L}}{\partial \partial_\alpha \phi} = 0 \tag{2.7}$$

Taking the example of the Klein-Gordon field up again, the lagrangian density, or simply the lagrangian, that results in the correct equation of motion is

$$\mathcal{L} = \frac{1}{2}\left(\partial_\alpha \phi \partial^\alpha \phi - \mu^2 \phi^2\right) \tag{2.8}$$

The next sections will introduce the most important parts of the SM. It will be seen that the Lagrangian formalism is quite convenient to include new aspects in an overseeable manner.

2.3 The Dirac field

The correct field that represents the spin 1/2 SM fermions is the Dirac field, proposed by Paul Dirac [16]. He started from Schrödinger's equation for a free particle (in natural units)

$$i\frac{\partial}{\partial t}\psi\left(x\right) = \frac{1}{2m}\nabla^2\psi\left(x\right) \tag{2.9}$$

A relastivitically correct theory can not be of this form as discussed earlier. Dirac proposed that a solution is possible where the derivatives in space only appear in 1st degree. His solution has the form

$$i\frac{\partial}{\partial t}\psi\left(x\right) = \left[\alpha\cdot\left(-\nabla\right) + \beta\mathbf{m}\right]\psi\left(x\right) \tag{2.10}$$

using $\gamma^0 = \beta$ and $\gamma^i = \beta\alpha^i$ it can be written shorter as

$$i\gamma^\mu \partial_\mu \psi(x) - m\psi(x) = 0 \tag{2.11}$$

This solution should of course satisfy the Pauli exclusion principle if it wants to represent fermions. As it turns out the simplest solution requires γ^μ, the gamma matrices to be $4x4$ matrices, that satisfy the anticommutation relations

$$[\gamma^\mu, \gamma^\nu]_+ = 2g^{\mu\nu}\mathbb{1}_{4x4} \tag{2.12}$$

and the hermeticity conditions

$$\gamma^{\mu\dagger} = \gamma^0\gamma^\mu\gamma^0 \tag{2.13}$$

These conditions completely define the gamma matrices. The corresponding four component wavefunctions $\psi(x)$ are called Dirac spinors. In order to derive a lagrangian that brings 2.11 about, the adjoint field of ψ needs to be defined:

$$\overline{\psi}(x) = \psi^\dagger(x)\gamma^0 \tag{2.14}$$

The Lagrangian that leads to the Dirac equation is then

$$\mathcal{L} = \overline{\psi}(x)\not{\partial}\psi(x) - m\overline{\psi}(x)\psi(x) \tag{2.15}$$

The notation was simplified even more by $\not{\partial} = \gamma^\mu\partial_\mu$.

Dirac fermions consist of complex fields, because the gamma matrices are complex too. A complex field implicates the existence of anti-particles, which can be shown in a brief derivation. The complex field ψ annihilates particles and creates anti-particles, while its complex conjugate will annihilate anti-particles and create particles. To see this explicitly, the fields can be decomposed into creation and annihilation operators $a^s_{\mathbf{p}}$, $a^{s\,\dagger}_{\mathbf{p}}$, $b^s_{\mathbf{p}}$ and $b^{s\,\dagger}_{\mathbf{p}}$:

$$\psi(x) = \int \frac{d^3p}{(2\pi)^3}\frac{1}{\sqrt{2E_{\mathbf{p}}}}\sum_s \left(a^s_{\mathbf{p}}u^s(p)\,e^{-ip\cdot x} + b^{s\,\dagger}_{\mathbf{p}}v^s(p)\,e^{ip\cdot x}\right) \tag{2.16}$$

$$\overline{\psi}(x) = \int \frac{d^3p}{(2\pi)^3}\frac{1}{\sqrt{2E_{\mathbf{p}}}}\sum_s \left(b^s_{\mathbf{p}}\overline{v^s}(p)\,e^{-ip\cdot x} + a^{s\,\dagger}_{\mathbf{p}}\overline{u^s}(p)\,e^{ip\cdot x}\right) \tag{2.17}$$

The creation and annihilation operators have to obey the anticommutation relations

$$\left[a^r_{\mathbf{p}}, a^{s\,\dagger}_{\mathbf{p}}\right]_+ = \left[b^r_{\mathbf{p}}, b^{s\,\dagger}_{\mathbf{p}}\right]_+ = (2\pi)^3\,\delta^{(3)}(\mathbf{p}-\mathbf{q})\,\delta^{rs} \tag{2.18}$$

From equations 2.16 and 2.17 it follows that $a^{s\,\dagger}_{\mathbf{p}}$ creates a fermion and $b^{s\,\dagger}_{\mathbf{p}}$ creates an anti-fermion with energy $E_{\mathbf{p}}$ and momentum $\mathbf{p}$ in both cases. For example the one electron state or one-positron state can be created by operating with the creation operators on the vacuum state:

$$\begin{aligned}
|e^-, \mathbf{p}, \mathbf{s}\rangle &= \sqrt{2E_{\mathbf{p}}}a^{s\,\dagger}_{\mathbf{p}}|0\rangle \\
|e^+, \mathbf{p}, \mathbf{s}\rangle &= \sqrt{2E_{\mathbf{p}}}b^{s\,\dagger}_{\mathbf{p}}|0\rangle
\end{aligned}$$

Particles and anti-particles thus have their own creation and annihilation operators. For the SM quarks and charged leptons this is perfect as they have been shown to behave like Dirac fermions, they are clearly distinct from their anti-particle. However, a different solution exists for the gamma matrices, where they are purely imaginary. As a consequence the field can be real and the resulting creation operators for particles and anti-particles are identical, as complex conjugation has no effect. Particles and anti-particles are created and annihilated by the same operators, there is no distinction between them. This idea was first realized by Ettore Majorana [17]. Therefore these hypothetical particles bear the name Majorana fermions. An important characteristic of Majorana fermions is that they have to be neutral for all interactions, as anti-particles have opposite charge from particles. This means that from the fundamental SM fermions, only the neutrinos are left as a possibility. It has not yet been established if neutrinos are Dirac or Majorana, but extensive research is being done in order to uncover the truth.

2.4 Gauge Invariance

The electromagnetic, weak and strong interactions are all examples of gauge theories. The interaction terms are naturally introduced in the lagrangian by requiring local gauge invariance for the total Lagrangian. This principle can be best illustrated using QED [18], the simplest gauge theory. The free lagrangian of a fermion

$$\mathcal{L} = \overline{\psi}(x)\left(i\partial\!\!\!/ - m\right)\psi\left(x\right) \tag{2.19}$$

is invariant under a global phase transformation of the field

$$\begin{aligned}\psi(x) \to \psi'(x) &= \psi(x)e^{-i\alpha}\\ \overline{\psi}(x) \to \overline{\psi}'(x) &= \overline{\psi}(x)e^{i\alpha}\end{aligned} \tag{2.20}$$

The global gauge invariance is responsible for current conservation and charge conservation, essential aspects of the theory. It is now possible to go a step further. Since action at a distance is something unphysical and should be avoided, the fields at a certain position in space and time can only be influenced by interactions at the same position. The global gauge invariance can therefore be generalized to local gauge invariance at every point in space and time.

$$\begin{aligned}\psi(x) \to \psi'(x) &= \psi(x)e^{-iqf(x)}\\ \overline{\psi}(x) \to \overline{\psi}'(x) &= \overline{\psi}(x)e^{iqf(x)}\end{aligned} \tag{2.21}$$

where $f(x)$ is a real differentiable function. But the Lagrangian is no longer invariant under these transformations, as

$$\mathcal{L} \to \mathcal{L}' = \overline{\psi}(x)\left(i\partial\!\!\!/ - m\right)\psi\left(x\right) + q\overline{\psi}(x)\gamma^{\mu}\psi(x)\partial_{\mu}f(x) \tag{2.22}$$

The invariance can be restored by associating a gauge field $A_\mu(x)$ with the matter field $\psi(x)$ that transforms in such a way under the gauge transformation that the additional term in 2.22 is canceled out. The gauge field is introduced by changing the derivative ∂_μ into a covariant derivative D_μ.

$$D_\mu \psi(x) = \left(\partial_\mu + iqA_\mu\right)\psi(x) \tag{2.23}$$

While $A_\mu(x)$ transforms as

$$A_\mu(x) \rightarrow A'_\mu(x) = A_\mu(x) - \partial_\mu f(x) \tag{2.24}$$

The augmented Lagrangian

$$\mathcal{L} = \overline{\psi}(x)\left(i\not{D} - m\right)\psi\left(x\right) \tag{2.25}$$

is again invariant under the gauge transformation. The interaction term that governs the electromagnetic force

$$\mathcal{L}_I = -q\overline{\psi}(x)\gamma^\mu\psi(x)A_\mu(x) \tag{2.26}$$

has appeared in a natural way in the model.

An argument that can be made against the previous reasoning is that the minimal substitution of the gauge field is one of many ways to introduce the gauge fields to obtain local gauge invariance. But as it appears, the minimal substitution is the only method that leads to a renormalizable theory. all non-minimal interactions will lead to divergences in the UV region and are thus unphysical [14].

A kinetic term is still necessary for the gauge field A_μ. The kinetic term governs the propagating behavior of the gauge field. The correct form is

$$\mathcal{L}_{kin} = F_{\mu\nu}F^{\mu\nu} \qquad \text{with } F_{\mu\nu} = \partial_\mu A_\nu - \partial_\nu A_\mu \tag{2.27}$$

The gauge invariance under the transformations in 2.21 constitutes a $U(1)$ symmetry of the field. The method can be generalized to other symmetry groups and their respective gauge transformations. The electroweak unification for example is represented by the symmetry group $SU(2)_L \times U(1)_Y$, while the strong interaction is represented by $SU(3)_c$. $SU(n)$ is the group of $n \times n$ unitary matrices with determinant 1. It is aptly called the special unitary group of order n. There are a myriad of other symmetry groups that can constitute gauge theories, i.e. the symplectic groups $Sp(n)$ or the special orthogonal groups $SO(n)$, but apparently nature chose for the three first groups; $U(1)$, $SU(2)$ and $SU(3)$ [4]. Of course it is entirely possible that nature is hiding symmetry in the form of more exotic groups, but currently we are left with mere speculation.

2.5 Electroweak unification

The Unification of the electromagnetic and weak interaction [20], while an essential part of the SM, is not particularly relevant for this dissertation. Therefore it is only summarized in broad terms and it will not be calculated in detail.

2.5.1 The Weak interaction

It might first be useful to delve a little deeper into the properties of the weak interaction, as it is more intricate than the electromagnetic interaction. The force is transferred through three massive vector bosons, the charged W^+ and W^- and the neutral Z boson. The W's were discovered much earlier than the Z, being responsible for nuclear β-decay, which was already studied at the end of the 19th century. The Z boson was predicted theoretically when a consistent theory of the weak interaction was formed. This happened a couple years before neutral currents were detected for the first time by the Gargamel detector at CERN in the 70's [21, 22], giving indirect evidence of its existence. The weak bosons are the only gauge bosons with mass, acquiring their mass through the spontaneous symmetry-breaking of the Higgs field. The mass of the W's, according to experiments gathered by the particle data group [9] is $80.385 \pm 0.015 GeV$, while the mass of the Z is $91.1876 \pm 0.0021 GeV$. The fact that they are so massive is the reason why the weak interaction is so much weaker than the electromagnetic interaction at low energies. At higher energies they become comparable in strength.

The W^+ and W^- are the only interactions that change the flavour of the particles they interact with. This is necessitated by charge conservation as these bosons are charged themselves. flavour changing can happen across different generations but these couplings all differ in strength. They are characterized by the CKM matrix for quarks and by the PMNS matrix for leptons. Flavour changing neutral currents through the Z boson do not take place according to our current understanding.

The weak interaction is a parity violating interaction [23]. Parity is essentially a transformation in space where the three spatial coordinates are flipped in sign. Parity conservation was tought to be a fundamental trait of nature before the weak force spoiled this. It turns out that the W-bosons even violate parity maximally, resulting in an interaction term in the lagrangian of the following form (for coupling of the W to leptons)

$$\frac{-g}{2\sqrt{2}} \overline{\Psi}(\nu_l) \not{W} \left(1 - \gamma^5\right) \Psi(l) \tag{2.28}$$

The vector part $(\overline{\Psi}(\nu_e) \not{W} \Psi(l))$ and axial vector part $(\overline{\Psi}(\nu_l) \not{W} \gamma^5 \Psi(l))$ have respectively parity 1 and -1. The factor $-g/2\sqrt{2}$ entails the coupling between the fermions and the W bosons. The factor $(1 - \gamma^5)/2$ can be interpreted as a projection operator of so called chirality. It projects fields onto their left-handed state. Similarly, $(1 + \gamma^5)/2$ projects onto the right-handed chiral state.

$$P_L = \frac{1-\gamma^5}{2} \tag{2.29}$$

$$P_R = \frac{1+\gamma^5}{2} \tag{2.30}$$

These projection operators obey the relations

$$P_L^2 = P_L,\ P_L P_R = 0,\ P_L + P_R = 1 \tag{2.31}$$

When operating on a field, they leave the left- or right-handed part behind

$$\psi_L = P_L\psi,\ \psi_R = P_R\psi \tag{2.32}$$

There is an interesting link between chirality and helicity of a particle. Helicity of a particle is the projection of its spin onto the direction of its momentum

$$\sigma_{\mathbf{p}} = \frac{\sigma \cdot \mathbf{p}}{|\mathbf{p}|} \tag{2.33}$$

For massless particles it can be shown that chirality and helicity are always equal. For massive particles this holds up to terms of order $O(m/|\mathbf{p}|)$, so for high energy (or low mass) particles it holds approximately [14].

A new problem arises from the fact that the weak interaction couples differently to the left-handed and right-handed parts of the fields. The invariance of the mass term is not valid under gauge transformation that violate parity. This can be illustrated quickly by decomposing the mass term in left and right handed fields:

$$\begin{aligned}
m\overline{\psi}\psi &= m\overline{\psi}\left(P_L + P_R\right)\psi && (2.34)\\
&= m\overline{\psi}\left(P_L^2 + P_R^2\right)\psi && (2.35)\\
&= \frac{m}{2}\left(\psi^\dagger\gamma^0\left(1-\gamma^5\right)\psi_L + \psi^\dagger\gamma^0\left(1+\gamma^5\right)\psi_R\right) && (2.36)\\
&= \frac{m}{2}\left(\psi^\dagger\left(1+\gamma^5\right)\gamma^0\psi_L + \psi^\dagger\left(1-\gamma^5\right)\gamma^0\psi_R\right) && (2.37)\\
&= m\left(\overline{\psi}_R\psi_L + \overline{\psi}_L\psi_R\right) && (2.38)
\end{aligned}$$

And it is seen directly that if left and right handed fields transform differently that gauge invariance is lost. Fortunately the Higgs field will allow to salvage the fermion masses through Yukawa coupling.

2.5.2 Spontaneous Symmetry-breaking

Electroweak unification can be summarized by saying that the initial symmetry present in nature, namely the symmetry group $SU(2)_L \times U(1)_Y$, is broken. The subscript of $SU(2)_L$ means it couples only to left-handed states. The subscript of $U(1)_Y$ stands for hypercharge, a new charge that is introduced. $SU(2)_L \times U(1)_Y$ is spontaneously broken into the symmetry groups that characterize the weak and electromagnetic interaction, namely $SU(2)_L$ and $U(1)_{EM}$. The left-handed part of lepton and quark generations are placed in a doublet that transforms under $SU(2)_L$ while the right-handed parts are left as singlets that transform identical under $SU(2)_L$. E.g. for leptons this becomes

$$\Psi_L = \begin{pmatrix} \nu_l^L \\ l^L \end{pmatrix},\ l^R,\ \nu_l^R \tag{2.39}$$

The gauge fields are written out using the pauli matrices σ_a.

$$\hat{W}_\mu = \frac{1}{2}\sum_{a=1}^{3} W_\mu^a(x)\sigma_a = \frac{1}{2}\begin{pmatrix} W_\mu^3(x) & W_\mu^1(x) - iW_\mu^2(x) \\ W_\mu^1(x) + iW_\mu^2(x) & W_\mu^3(x) \end{pmatrix} \tag{2.40}$$

It can be seen W_μ^1 and W_μ^2 are responsible for the flavour changing interactions as they constitute the off-diagonal terms. The $U(1)_Y$ gauge field is represented by $B_\mu(x)$. Together with the neutral W_μ^3 it will transform into the weak Z_μ and electromagnetic A_μ. The only linear transformation that keeps the Lagrangian invariant is a rotation

$$W_\mu^3 = sin\theta_W A_\mu + cos\theta_W Z_\mu \tag{2.41}$$

$$B_\mu = cos\theta_W A_\mu - sin\theta_W Z_\mu \tag{2.42}$$

The angle θ_W is called the weak angle. The flavour changing interactions are formed by combining W_μ^1 and W_μ^2

$$W_\mu = \frac{1}{\sqrt{2}}\left(W_\mu^1 + iW_\mu^2\right) \tag{2.43}$$

$$W_\mu^\dagger = \frac{1}{\sqrt{2}}\left(W_\mu^1 - iW_\mu^2\right) \tag{2.44}$$

The coupling constants that come along with the interactions can be determined by fitting the interaction terms to the known forms of the weak and electromagnetic interaction. These will not be discussed here. A last thing to note is that the weak theory is a non-abelian gauge theory, due to the flavour changing interactions. As a consequence, self-interacting terms appear, two examples of which are shown in figure **??** as well as interaction terms with the electromagnetic ield.

The electroweak unification elegantly combines the two interactions in one theory. It only depends on a minimal amount of parameters and manages to make profound predictions. But as mentioned before, the theory does not explain how the gauge bosons acquire their masses. This is where the BEH mechanism comes into play.

2.6 The Strong Interaction

The strong interaction is expressed in a theory called quantum chromodynamics (QCD). The theory was developed on the basis of the new quantum number 'colour' [24]. There

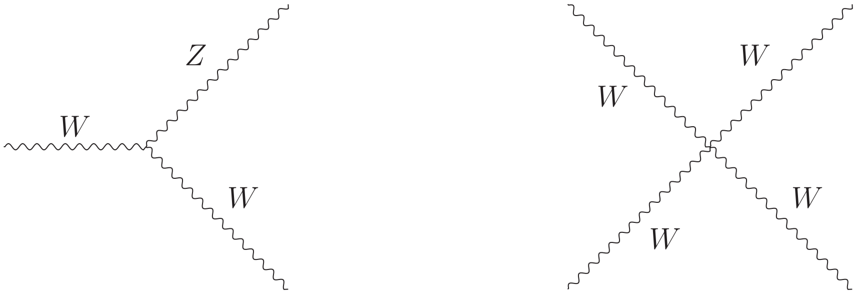

(a) WWZ vertex **(b)** WWWW vertex

Figure 2.2: Two examples of self interaction processes.

were two features of quarks that led to its conception. Firstly, quarks never appear as free particles in nature, but only as bound states of more composite particles, the hadrons. Hadrons can be subdivided into baryons and mesons. Baryons are bound states of three quarks and mesons consist of a quark and antiquark. Recently, a new class of hadrons was discovered by the LHCb experiment at the Large Hadron Collider, pentaquarks, that are basically bound states of a baryon and a meson [25]. But quarks never appear as free particles or as fractionally charged bound states. Secondly, baryons with same flavour quarks have a symmetric space and spin wavefunction with regard to interchange of these quarks. This is not allowed by Pauli's exclusion principle. The introduction of colour was able to provide a satisfying answer to both questions. Colour can essentially be seen as the charge of the strong interaction in the same way that the electric charge is the charge for the EM interaction. The quarks can have one of three colours; red, green and blue. Through the strong interaction, total colour is always conserved. The colour spinors χ^c can be represented in matrix form

$$\chi^r = \begin{pmatrix}1\\0\\0\end{pmatrix} \quad \chi^g = \begin{pmatrix}0\\1\\0\end{pmatrix} \quad \chi^b = \begin{pmatrix}0\\0\\1\end{pmatrix} \tag{2.45}$$

These colour wavefunctions can be acted upon by colour operators, three-dimensional hermitian matrices. It turns out that there are eight linearly independent hermitian matrices in three dimensions, labeled as $\lambda_i,\ (i = 1, ...8)$. They generate the operators

$$\hat{F}_i = \frac{1}{2}\lambda_i \tag{2.46}$$

The operators with off-diagonal terms are able to change the colour of the wavefunction they act upon. Multiquark states should be described by the product of their wavefunctions, for the colours this gives

$$\chi^c_{tot} \equiv \chi^c_1 \chi^c_2 \cdots \chi^c_n \tag{2.47}$$

Action of the operators on the combined state is governed by the distributive law.

$$\hat{F}_i \chi^c_1 \chi^c_2 = \left(\hat{F}_i \chi^c_1\right) \chi^c_2 + \chi^c_1 \left(\hat{F}_i \chi^c_2\right) \tag{2.48}$$

The unexplainable properties of hadrons can now be solved by introducing the concept of colour confinement. The requirement is set that hadrons must exist only in colour states that satisfy

$$\hat{F}_i \chi_h^c = 0 \quad \forall i \tag{2.49}$$

Hadrons can only be found in colorless states. It follows that only baryons and mesons are possible combinations according to colour confinement. The problem with the symmetric wavefunction has also been cleared as the extra colour wavefunction part is added.

The strong interactions can be introduced through the gauge mechanism. It is seen that the matrices λ_i generate the symmetry group $SU(3)$. By first introducing the global phase invariance of the fields and then localizing it, eight real gauge fields $A^j_\mu(x)$ are naturally generated. They are called the gluon fields. Because of the previously mentioned capability of the strong interaction to change the colour of quarks, it follows that the gauge bosons carry colour charge themselves. Self-interacting terms will thus be present in the model. These will flow out of the kinetic term for the gluon fields. With this final step, the theory of quantum chromodynamics is complete.

2.7 Brout-Englert-Higgs mechanism

The BEH mechanism [7, 8] starts by introducing a complex scalar field to the lagrangian. It's lagrangian density is

$$\mathcal{L} = \partial_\mu \phi^\dagger \partial^\mu \phi - V(\phi) \tag{2.50}$$

where $V(\phi)$ is the potential corresponding to the field. By proposing a specific form for the potential, spontaneous symmetry-breaking is introduced:

$$\mathcal{L} = \partial_\mu \phi^\dagger \partial^\mu \phi + \mu \left(\phi^\dagger \phi\right) - \lambda \left(\phi^\dagger \phi\right)^2 \tag{2.51}$$

If we look for the stable minima of this field, compared to which we can use perturbation theory, it turns out they are not located at the origin of the field $\phi = 0$ but at points that satisfy $|\phi| = v/\sqrt{2}$ where $v = \sqrt{m^2/\lambda}$. All points that satisfy these conditions are equally qualified to be the actual physical ground state where the field resides. Choosing one value rather than another has no physical implications whatsoever. Therefore an easy choice is the field value

$$\phi_0 = \frac{v}{\sqrt{2}} \tag{2.52}$$

The value v is called the vacuum expectation value (VEV), because if the field acts on the vacuum state $|0\rangle$ it gives a nonzero expectation value. The VEV is essential to the BEH mechanism. For small field excitations it is possible to perturb the field around its minimum, using the real-valued fields $\sigma(x)$ and $\eta(x)$

$$\phi(x) = \frac{1}{\sqrt{2}} \left(v + \sigma(x) + i\eta(x)\right) \tag{2.53}$$

Substituting this expression into the lagrangian it eventually gives a free lagrangian for the scalar fields

$$\mathcal{L}_0 = \frac{1}{2}\partial_\mu\sigma\partial^\mu\sigma - \frac{1}{2}\left(\sqrt{2}m\right)^2\sigma^2 + \frac{1}{2}\partial_\mu\eta\partial^\mu\eta \tag{2.54}$$

As well as three- and fourpronged interaction terms for both fields that are not looked at in detail here.

It can now be illustrated how this field can provide mass for the gauge fields. The example shown next is for a $U(1)$ gauge field, but can just as easily be extended to other gauge fields. Imagine the lagrangian has been made gauge invariant by introducing the new field

$$\mathcal{L} = D_\mu\phi^\dagger D^\mu\phi + m^2\phi^\dagger\phi - \lambda\left(\phi^\dagger\phi\right)^2 - \frac{1}{4}F_{\mu\nu}F^{\mu\nu} \tag{2.55}$$

The gauge transformation transforms the fields as follows

$$\phi(x) \to \phi'(x) = e^{iqf(x)}\phi(x) \tag{2.56}$$

$$A_\mu(x) \to A'_\mu(x) = A_\mu(x) - \partial_\mu f(x) \tag{2.57}$$

Remember that the choice of any of the minima of the scalar field was just as valid as any. From all possible field values (in a slightly different notation)

$$\phi = (v + \sigma(x))\, e^{\frac{i}{v}\eta(x)} \tag{2.58}$$

we therefore choose the so called unitary gauge for which holds $qf(x) = -\eta(x)/v$. The unitary gauge gives then

$$\phi = \frac{1}{\sqrt{2}}(v + \sigma(x)) \tag{2.59}$$

Where the real valued field $\eta(x)$ has disappeared. $\eta(x)$ was a Goldstone boson which was eliminated by breaking the symmetry and providing mass to the gauge field. It is 'absorbed' into the extra degree of freedom that is introduced for the gauge field, a longitudinal polarization is now possible, unlike with massless gauge fields. The boson has indeed acquired mass, which can be seen clearly after executing the straigthforward calculations. Again we write down just the free lagrangian without the interaction terms which will not be discussed.

$$\mathcal{L}_0 = \frac{1}{2}\partial_\mu\sigma\partial^\mu\sigma - \frac{1}{2}\left(\sqrt{2}m\right)^2\sigma^2 - \frac{1}{4}F_{\mu\nu}F^{\mu\nu} + \frac{q^2}{2}v^2A_\mu A^\mu \tag{2.60}$$

The last term is the mass term for the gauge field. The same method can be applied to the $SU(2)$ theory of the weak bosons. Their masses are generated by the BEH mechanism. Additionally, a new particle has been introduced to the standard model, commonly known as the Higgs boson. The Higgs boson was the last particle of the standard model to be detected. Only in 2012 were the CMS and ATLAS experiments at the Large Hadron Collider (LHC) in CERN, Geneva, finally able to experimentally verify its existence.

2.8 Yukawa coupling

After the bosons have acquired their mass from the BEH field, it is also possible to recover the masses of the fermions, lost by introducing different couplings for left- and right-handed fermion fields. The following terms have to be added to the lagrangian

$$\mathcal{L} = -\lambda\phi\overline{\Psi}^R\Psi^L - \lambda\phi^\dagger\overline{\Psi}^L\Psi^R \tag{2.61}$$

The fields transforms as follows (under again the example of a $U(1)$ interaction, it holds as well under $SU(2)$)

$$\Psi^R \to e^{iq_R f(x)}\Psi^R \tag{2.62}$$
$$\Psi^L \to e^{iq_L f(x)}\Psi^L \tag{2.63}$$
$$\phi \to e^{iqf(x)}\phi \tag{2.64}$$

if now the coupling $q = q_R - q_L$ the terms in 2.61 are gauge invariant, so they are allowed to be added to the lagrangian. If we write the scalar field in the unitary gauge again ($\phi = 1/\sqrt{2}\,(v + \sigma(x))$) and work out the lagrangian, we get

$$\begin{aligned}\mathcal{L} &= -\frac{\lambda v}{\sqrt{2}}\overline{\Psi}\Psi - \frac{\lambda\sigma}{\sqrt{2}}\overline{\Psi}\Psi \\ &= -m_\Psi\overline{\Psi}\Psi - \frac{m_\Psi}{v}\sigma\overline{\Psi}\Psi \end{aligned}\tag{2.65}$$

And a mass term is safely introduced for the fermion fields, as well as an interaction term between the scalar field and the fermion field. The mass is linearly dependent on the parameter λ which is still a free parameter. The current model is thus unable to predict why the fermions have the masses they do.

The Yukawa couplings provide a satisfying mechanism to generate the bare masses of quarks and leptons. There is however one fact still bothering people, the neutrino masses. After the electron with a mass of approximately $511\,keV$ there is a mass gap of several orders of magnitude where no particles are found before the neutrinos appear with masses at the sub-eV scale. This means the neutrinos require extremely small values for the parameter λ, of the order of 10^{-10}, that is seen as unphysical. For the other fermions the values of λ are of similar orders of magnitude. As discussed before, it is still entirely possible for the neutrinos to be fundamentally different in nature by being Majorana particles. In this scenario, a very elegant theory exists to explain why the masses of the SM neutrinos are so low: the Seesaw Mechanism.

Chapter 3

The Seesaw Mechanism

3.1 C-symmetry

It might first be important to specify how particles are transformed into their antiparticles[26]. This happens through a charge conjugation transformation. If interactions do not change under charge conjugation, it is said that they conserve C-symmetry. The strong and electromagnetic interaction both respect C-symmetry, but the weak interaction does not. An expression for the charge conjugation transformation can be written using the gamma-matrices. It can be deduced that the charge conjugated field of a spinor is equal to

$$\psi_c = i\gamma^2\psi^\star \tag{3.1}$$

The weak interaction violates C-symmetry because it couples differently to left- and right-handed fields [23]. Left-handed fields are transformed into left-handed anti-fields by charge conjugation. It is clear that the weak interaction does not remain invariant.

3.2 Effect of a Majorana mass term

If the neutrinos turn out to be Majorana [27] meaning their field is real and the spinors are identical to their charge conjugated part $\psi_c = \psi$, then it is possible to include another mass term in the standard model for the right-handed neutrinos. Since the right-handed neutrinos are uncharged under $SU(3)_c \times SU(2)_L \times U(1)_Y$, the gauge invariance will not be disrupted by adding an additional mass term to the lagrangian, next to the mass term generated by the Yukawa coupling. The following reasoning holds for one flavour of neutrino but can be extended to three flavours that mix through neutrino oscillations.

$$\mathcal{L} = i\overline{\nu}\not{\partial}\nu - m\overline{\nu}\nu - \frac{M}{2}\left(\overline{\nu}_R\nu_R c + \overline{\nu}_R c\nu_R\right) \tag{3.2}$$

where m is the mass generated by the higgs field and M is the mass coming from the Majorana term. Rewriting the spinors as

$$\chi = \frac{1}{\sqrt{2}} \left(\nu_R + \nu_R c\right)$$
$$\omega = \frac{1}{\sqrt{2}} \left(\nu_L + \nu_L c\right)$$

Then we can rewrite the lagrangian using matrix notation (calculations are straightforward and thus left out).

$$\mathcal{L} = i\overline{\chi}\partial\!\!\!/\chi + i\overline{\omega}\partial\!\!\!/\omega + \begin{pmatrix} \overline{\chi} & \overline{\omega} \end{pmatrix} \begin{pmatrix} M & m \\ m & 0 \end{pmatrix} \begin{pmatrix} \chi \\ \omega \end{pmatrix} \tag{3.3}$$

The mass matrix is not diagonal in this basis, so in order to get the mass eigenstates it should be diagonalized. Solving the eigenvalue problem gives the solutions

$$m_\pm = \frac{M}{2} \left(1 \pm \sqrt{1 + \frac{4m^2}{M^2}}\right) \tag{3.4}$$

As we know, the masses of the neutrinos are confined to the sub-eV scale. This gave an extremely small value for the Yukawa coupling. If in this model, we assume that the mass $m \sim 10^2 GeV$, in the same order of magnitude of the other fermions. Suppose the Majorana mass M is on a much higher scale, for example on the GUT-scale where new physics is expected to appear, $M \sim 10^{15} - 10^{16} GeV$. An approximation can then be made for the two mass solutions

$$m_+ \approx M$$
$$m_- \approx -\frac{m^2}{M}$$

At first sight it seems a problem that the second mass is negative. But this can be resolved by rescaling the field to positive value of the mass, since the field is defined up to a constant. The essential part is that, because the Majorana mass M is so large, it pulls the other mass down to lower values. This is why it is called the seesaw mechanism. The low masses of the neutrinos could be explained very elegantly in this manner. It would not require improbably low coupling parameters and on top of that, it predicts that high mass neutrinos might be found at high energies. If a particle matching the properties of this heavy neutrino would be found in an experiment, it might be inferred that the SM neutrinos are in fact Majorana particles. This dissertation is part of the larger research going on at the experimental particle physics group at UGent [62]. The aim is to use the CMS detector that is located at one of the four collision points of the LHC at CERN, Geneva to either confirm the existence of the heavy neutrinos or place boundaries on the parameter space it could appear in. It is important to note that the form of the seesaw mechanism prescribed here, is not the one that will be searched for at the LHC. It is only meant to give an indication of the mechanism without going into too much theoretical detail. There exist other mechanisms that LHC can probe [27].

Chapter 4

The Large Hadron Collider and CMS

The research in this dissertation has been carried out in collaboration with and specifically for the Compact Muon Solenoid (CMS) experiment [30], one of the four experiments at the Large Hadron Collider (LHC) [28]. The LHC is a circular proton-proton collider, located underground at the European Centre for Nuclear Research (CERN) near Geneva, precisely at the border between France and Switzerland. It has a circumference of 27 km, by far the largest of its kind. This allows it to reach unprecedentedly high centre-of-mass energies in collisions, making it an ideal experiment for particle physics research.

This chapter details the workings of the LHC and more specifically of CMS, one of the four detectors located at a point where the collisions happen. The properties of the proton beams that go around the ring are elucidated, as well as the reconstruction algorithms that are used to process the raw data collected by the detector into useful and condensed information for analysis. The research in this thesis revolves around the online data selection mechanisms that CMS adopts, called triggers. A little more time is spent elaborating on them. Lastly, simulation techniques are discussed, which are indispensable as they allow to test theory against experiment. Ultimately the ambition of the LHC can be expressed in two objectives: to test the rigidness of the SM and to probe for new phenomena beyond the SM.

4.1 The Large Hadron Collider

The LHC is a hadron accelerator ring built in the tunnel complex under Geneva. Previously this tunnel was home to the LEP accelerator ring. LEP used electron and positron beams for their experiments, while the LHC uses hadrons, meaning proton beams or Pb ion beams. Beams are accelerated around the ring in opposite directions in separate tubes. There are four collision points where the lines cross and the beams are focused to let them collide. Around the four points, dedicated detectors are built that aim to capture the physical phenomena that are going on. But how are the proton beams maintained inside the ring?

4.1.1 Superconducting magnets

The particles are guided properly around the circuit through the use of superconducting electromagnets [32]. Firstly, dipole magnets aim to curve the beams around the circular path. At peak performance these magnets can produce a magnetic field of $8.3T$, limiting the energy of protons that can still follow the curvature to $7\,TeV$,resulting in the upper limit in terms of centre-of-mass energy that can be reached: $14\,TeV$. In total, 1232 dipoles are spaced around the ring, each measuring $15m$ and having a weight of 35 tonnes. Secondly, the beam has to be kept compact, since a beam of particles with equal charge would not be stable on its own and quickly dissipate. This is accomplished by quadrupole magnets that confine the beam to an area with a diameter of approximately $0.2mm$. Right before the collision points, three additional quadrupole magnets, a so called 'inner triplet', confine the beams to even smaller areas in order to make collisions even more probable. The beam diameter is reduced drastically, to $16\mu m$ across. The magnets can only maintain their superconducting state in extremely low temperatures. Therefore the entire complex is cooled by a state of the art cryogenics system using liquid helium. The magnets are cooled to $1.9K$, even cooler than outer space at $2.7K$.

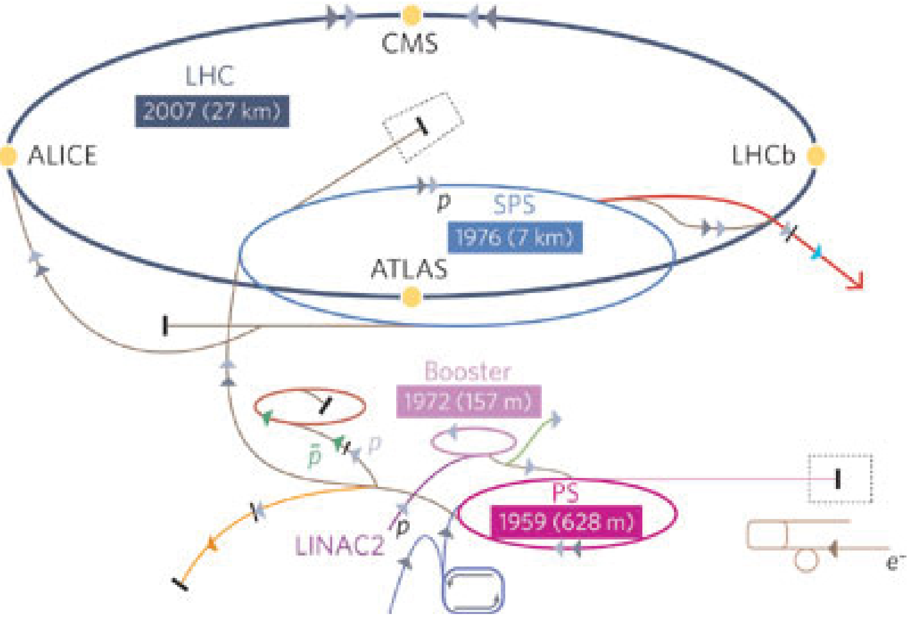

Figure 4.1: The CERN accelerator complex. The stages that the LHC beam passes through are all indicated [29].

4.1.2 Beam injection and acceleration

The acceleration of the beam happens in several stages, as can be seen in figure 4.1. Before being injected into the LHC, they have actually been through a series of other accelerators in the CERN accelerator complex. Each accelerator increases the beam energy before injecting it into the next ring. The protons start in LINAC2 [33], one of CERN's linear particle accelerators. Hydrogen gas is ionized before an electric field is used to accelerate it through this first stage. Continuing, it arrives in the Proton Synchroton Booster [34], the first circular stage. Oscillating electric fields are used to give the beam a boost each time it passes. After reaching a certain energy, it is injected in a larger accelerator ring, the Proton Synchrotron [35]. This cycle is repeated two times more, injecting the beam into the Super Proton Synchrotron [36] and ultimately into the LHC. The electric field is again provided by superconducting cavities. The frequency of the oscillating field lies in the radio frequency spectrum, therefore it is aptly called the RF accelerator system [37]. Each time a beam has to be extracted and injected from a ring, a drastic change in course is necessary. This is accomplished by kicker magnets [38], fast-switching dipole magnets, capable of switching on and off at high frequency and abruptly changing the trajectory of the beam.

4.2 Beam properties

4.2.1 Hadrons

Hadron colliders have a big advantage over lepton colliders, but they also come with a predicament. Their advantage is that hadrons are capable of reaching much higher energies. Charged particles that accelerate while passing through electromagnetic fields emit radiation, resulting in energy loss. This phenomenon is called brehmstrahlung and is the main limiting factor for the energy lepton colliders can reach. For radial acceleration the emitted power is equal to

$$P = \frac{e^2 E^4 \beta^2}{6\pi\epsilon_0 m^4 c^5 r^2 sin^2(\alpha)} \tag{4.1}$$

The emitted power is proportional to the fourth power of the energy and inversely proportional with the fourth power of the mass. At a certain energy threshold, the amount of radiated power will match the energy input from the RF accelerating system. Protons are about a 1000 times heavier than electrons, so they suffer from significantly smaller brehmstrahlung losses. The centre-of-mass energy at the LHC is 70 times higher than LEP. Unfortunately they are limited by the strength of the magnetic field. Otherwise a 2000-fold increase over LEP's energy would be feasible.

Hadrons are, unlike leptons, composite particles, consisting of valence quarks and a sea of gluons and quarks. These are collectively known as partons. At high energies, certainly the case at the LHC, the assumption of asymptotic freedom in QCD becomes valid, meaning an interaction with the proton can be considered to be an interaction with only one of the partons. The partons are considered to be free particles during the interaction. At each moment the total momentum of the proton is distributed over its partons. This complicates analysis as a collision between two protons is in fact a collision between two partons, of which the exact energy and momentum is unknown. This uncertainty is modeled by parton distribution functions (PDF) [39]. PDF's give the probability for each type of parton that it carries a certain fraction of the total momentum. Using these, interactions can be correctly simulated. More information on simulation techniques is discussed later.

4.2.2 Bunch separation

When the beam is traveling around the ring at full intensity, it is divided in equally spaced bunches that are separated by $7.5m$ or $25ns$ [40]. In total there are 2808 bunches for one beam. Each of these bunches consists of approximately $1.15 \cdot 10^{11}$ protons at maximum intensity. During the lifetime of a beam, this gradually decreases due to the arranged collisions at the detectors and losses around the ring. There are some holes between bunches that are larger, for example a $900m$ hole that is meant to give kicker magnets the time to charge up when the beam has run its course and needs to be dumped.

4.2.3 Centre-of-mass energy

The nominal beam energy is $7\,TeV$. Colliding two beams with this energy and opposite momentum leads to a centre-of-mass energy of $14\,TeV$. This is the maximal energy available for the interaction, as centre-of-mass energy is equal to the energy in the rest frame of the combined system of the two particles. In formula this is

$$\sqrt{s} = \sqrt{p_1^{\mu} p_{1\mu} + p_2^{\mu} p_{2\mu}} \tag{4.2}$$

where $\sqrt{s}$ is the conventional symbol that is used for the centre-of-mass energy and p_1 and p_2 are the four-momenta of the two protons. Currently the peak of $14\,TeV$ has not been reached yet. CERN has been ramping up the energy in several stages. During run I, which took place in 2012-2013, experiments took place at $\sqrt{s} = 7\,TeV$ and $\sqrt{s} = 8\,TeV$. After a series of upgrades, run II started in 2015 at $\sqrt{s} = 13\,TeV$, currently the highest energy that has been reached. The analysis in this dissertation happened with data taken at this energy. In the near future, it is planned that the LHC will finally operate at $14\,TeV$.

4.2.4 Luminosity

Finally, the LHC has another record it can boast about. It operates at the highest luminosity ever seen [41]. Luminosity is a measure for the amount of collisions that can take place per s. Collisions are generally also referred to as events. The number of events of a certain kind that happen per second can be expressed using the luminosity:

$$N_{event} = L\sigma_{event} \tag{4.3}$$

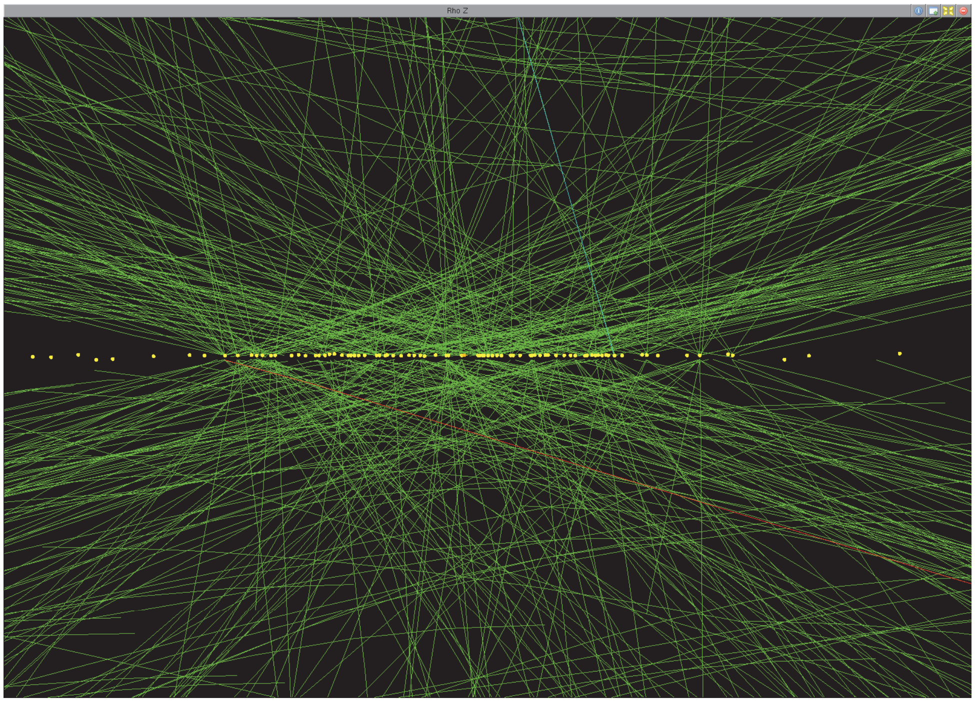

Figure 4.2: An example of pile-up during a bunch crossing. The line of highlighted interaction points make the beam line clearly visible. It can be seen that particle tracks originate from many interaction points.

where σ_{event} is the cross section for the event and L is the luminosity. If the beam is Gaussian distributed, the luminosity can be written as

$$L = \frac{N_b^2 n_b f_{rev} \gamma_r}{4\pi \epsilon_n \beta_\star} F \tag{4.4}$$

In this formula, N_b stands for the number of particles per bunch, n_b is the number of bunches per beam, $f_r ev$ is the revolution frequency, γ_r the relativistic gamma factor, ϵ_n the normalized transverse beam emmitance, $\beta_\star$ is the beta function at the collision point and F is the geometric luminosity reduction factor, which incorporates the angle at which the beams cross at the collision point. At CMS, as well as ATLAS, the aim is to use a luminosity has high as possible as this increases the chance of interactions. The peak luminosity is $L = 10^{34} cm^{-2} s^{-1}$. At luminosities of this order of magnitude, several collisions happen at each bunch-crossing, causing an unfavorable phenomenon called pile-up. During each bunch crossing, dozens of collisions between protons will happen. What this means is that when a bunch crossing gives rise to a highly diffractive, interesting, interaction, it will always be accompanied by a lot of noise in the form of particles coming from other interactions (see figure 4.2). The collision we are interested in will not be a clean signal but should be distinguishable from the noise. This is an important design parameter for the detector.

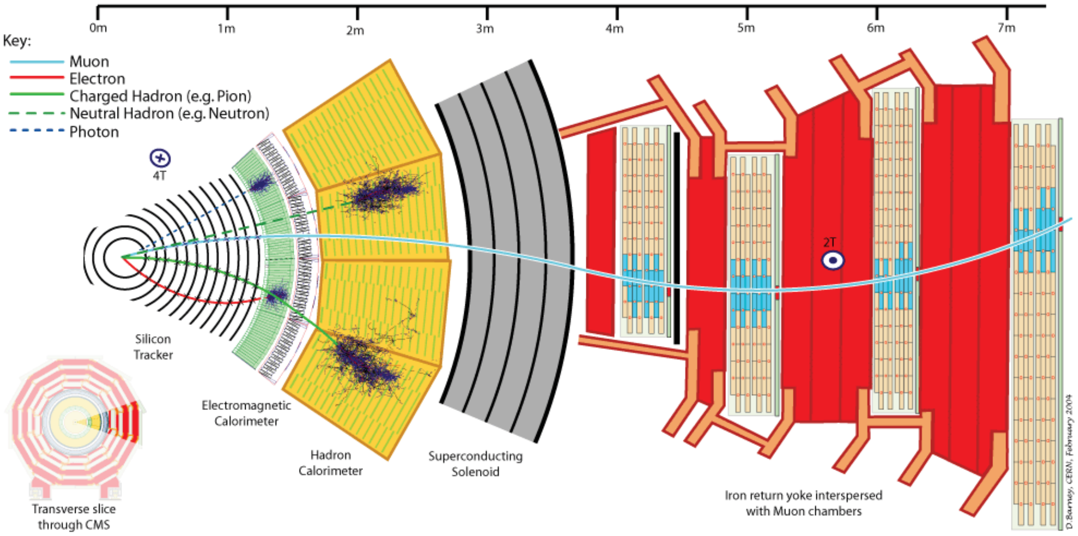

Figure 4.3: Cross section of the barell region of the CMS detector. The typical deposits that specific particles leave behind are depicted.

4.3 The CMS detector

The Compact Muon Solenoid, or CMS [30], is one of two general-purpose detectors, the other one being ATLAS [42], meant to be able to test a wide range of new physics scenarios at the TeV-scale. For that purpose, it is a hermetic detector, meaning it covers the whole space around the collision point. It is a very compact detector, weighing 12500 tonnes and being only $21.6m$ long and $14.6m$ across. The detector consists of several parts all with a specific purpose that are very closely packed, figure 4.3 shows a cross section detailing all parts in the barrel region. The barrel region is the main part of the detector, which encapsulates most of the transverse plane with respect to the beam axis. The endcap region supplements this at both ends of the beam axis.

4.3.1 The Solenoid magnet system

The detector is packed around a very powerful solenoid magnet [43]. The magnet consists of superconducting material and is able to produce a magnetic field of $4T$. Charged particle tracks will be curved when traversing the detector allowing to extract more information about the particle from the path it follows. Negatively and positively charged particles will be bent in different directions. On top of the charge, it also gives a way to measure the momentum, as high momentum particles will have a larger radius of curvature. Around the solenoid, several layers of steel return yoke aim to trap the field inside the detector volume and increase its homogeneity. They also serve a purpose in the muon detector system. The CMS collaboration has decided to operate the magnet at $3.8T$ instead of $4T$. Once the coil has aged and is better understood, this might be changed to $4T$.

4.3.2 The Silicon tracker

The inner part of the detector is home to the silicon tracker, the electromagnetic calorimeter (ECAL) and the hadron calorimeter (HCAL). CMS uses 10 layers of silicon microstrip detectors in the Silicon Tracker [44] that are able to provide high precision because of their granularity. This encloses another 3 layers of silicon pixel detectors. Only charged particles leave tracks, neutral particles traverse this part undetected. High precision is imperative in this section as it allows to determine if particles originated from a primary or secondary vertex or from unwanted pile-up events.

4.3.3 The Calorimeters

The electromagnetic calorimeter [45] consists of lead tungstate crystals. Avalanche photodiodes catch the scintillation light in the barrel region, while vacuum phototriodes are used in the endcap region. The ECAL's aim is to detect electrons and photon signals. They are completely stopped by the ECAL and deposit all their energy here. Their momentum can thus be derived from the amount of scintillated light that is produced. They are distinguished by their silicon tracker signal. While electrons leave clear tracks, photons go through undetected because they are uncharged. The hadron calorimeter [46] follows next, it is built out brass scintillating material, designed to stop hadrons. Hadrons deposit just a small part of their energy in the ECAL but deposit the remaining fraction completely in the HCAL. Neutral and charged hadrons can again be distinguished by their silicon tracker signal.

4.3.4 Neutrinos

Only two types of long-lived particles are able to traverse the entire detector, muons and neutrinos. Neutrinos are so weakly interacting that they leave the detector completely undetected. This provides a problem when particle tracks are reconstructed to determine what kind of event occurred. They are handled by constructing a variable called the transverse missing energy, or E_T^{miss}, which is minus the sum of all particle momenta during the event. Since before the collision the total momentum in the transverse plane is zero, conservation of momentum dictates that this needs to be the case after the collision too. Thus the cause of a non-zero total transverse momentum, conventionally named p_T, can only be the neutrino (within the SM).

4.3.5 The Muon system

Lastly, muons are the type of particle for which CMS was specifically built, hence why it appears in the name compact muon solenoid. Interleaved with the steel return yoke of the magnet are 4 muon stations [47]. Each station consists of several layers of aluminium drift tubes in the barrel region. In the endcap region the stations consist of cathode strip

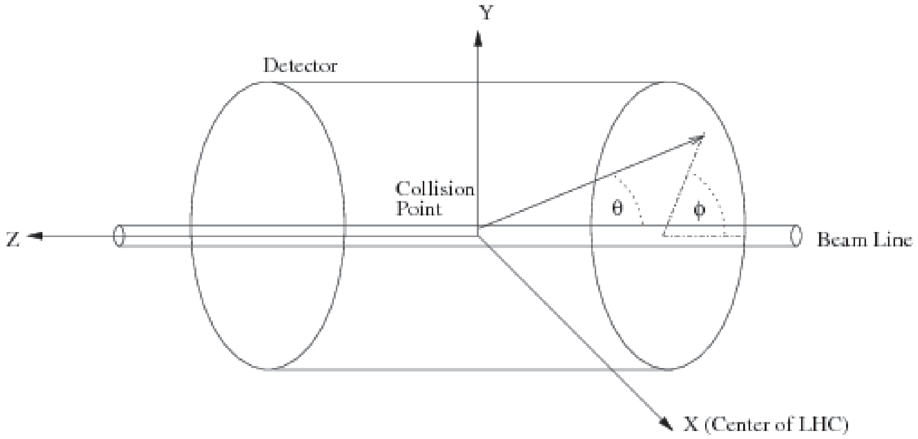

Figure 4.4: The variables in the coordinate system used by the CMS detector

chambers and resistive plate chambers. Since no other particles leave traces in the muon chambers, their signals are very clean, allowing to measure muons with high precision and making them an excellent experimental tool for analysis.

4.3.6 The Coordinate System

The direction of particle tracks is characterized in a coordinate system determined by convention (see figure 4.4). The interaction point is taken as the origin of the system. The X- and Y-axis lie in the transverse plane with respect to the beamline, with the X-axis pointing to the center of the LHC. The Y-axis is pointing upwards to the surface. The Z-axis follows the beam line in the direction that makes the coordinate system a right-handed system. A track can be fully determined by the azimuthal and polar angles, ϕ and θ. ϕ is simply the angle in the transverse plane between the X-axis and the track and is expressed in radial coordinates. Usually the pseudorapidity η is used instead of the polar angle θ. The expression for the pseudorapidity is

$$\eta = -ln\left(tan\left(\frac{\theta}{2}\right)\right) \tag{4.5}$$

This variable is more appropriate than the polar angle as the difference in pseudorapidity between two objects is a Lorentz invariant property. It will not change its value under a Lorentz boost along the beam line. With the azimuthal angle and the pseudorapidity, a third variable can be created that can quantify the difference in direction between two tracks, the angular separation ΔR

$$\Delta R = \sqrt{\Delta\phi^2 + \Delta\eta^2} \tag{4.6}$$

Since both $\Delta\phi$ and $\Delta\eta$ are invariant under boosts along the beam line, ΔR is a Lorentz invariant quantity too.

4.4 Reconstruction algorithms

Dedicated reconstruction algorithms exist for each type of particle that is stable enough to be detected directly [48]. These are only a small group of particles, i.e. photons, electrons, muons, charged hadrons and neutral hadrons. Reconstruction aims to identify each particle and measure their properties as accurately as possible. The information from all sub-detector parts needs to be combined to achieve this. Algorithms were designed and calibrated for each type of particle separately. There is a general work flow that is always followed when reconstructing signals.

4.4.1 Iterative tracking

For charged particles, the tracker is able to determine the direction and momentum with significantly greater accuracy than the calorimeters. Therefore it is used as the basis when determining properties of particles. In order to reconstruct tracks as efficiently as possible, a technique called iterative tracking is used. Iterative tracking starts by searching for tracks that pass very tight criteria, e.g. no missing hits, primary vertex very close to the beamline,... In a second step, the hits matching these tracks are removed and the algorithm starts searching again for tracks, but with slightly looser criteria now. This iterative process is repeated five times. It is able to achieve a very high efficiency, meaning very few tracks that should be reconstructed are correctly found. At the same time, the fraction of fakes, e.g. reconstructed tracks that were not left behind by an actual particle remain below the order of a per cent.

4.4.2 Calorimeter clustering

The second step is calorimeter clustering, energy deposits in the calorimeters are grouped together according to their positions and relative energy. For particles that have not left any hits in the tracker material, i.e. neutral hadrons, their calorimeter deposits will be essential for reconstruction. Calorimeter clustering is done separately for the ECAL barrel, ECAL endcap, HCAL barrel, HCAL endcap and PS barrel and endcap (PS is a part of the ECAL). It starts by finding cells with energy maxima compared to the cells surrounding them and above a certain threshold, these are cluster seeds. Then cells are aggregated to the cluster seeds if they have a side in common and have an energy above a certain threshold. This way, particle-flow clusters are created.

4.4.3 Link algorithm

Most particles are expected to give signals in several detector parts. Therefore it is imperative to combine the tracks in the silicon material, the calorimeter clusters and the tracks in the muon chambers. This is done by the Link algorithm. The best fitting tracks and clusters are combined into blocks of elements. Tracks are extrapolated for a certain distance in the calorimeters. If extrapolated positions cross energy clusters, they are matched. For electrons, the effect of Brehmstrahlung is brought into account by collecting clusters in the ECAL that are tangential to the extrapolated electron path. Clusters in ECAL and HCAL can also be combined if they are within a certain distance of each other. For muons,often several tracker tracks can be matched with a muon track and vice versa. The combination of a tracker track and muon track is called a global muon. For every muon track, the global muon with the smallest χ^2 is kept.

4.4.4 Particle reconstruction and identification

Finally, particle reconstruction and identification can take place. Currently we are left with blocks of elements that are matched. Within one block, the algorithm searches first for global muons that can be classified as particle-flow muons. For this their combined momentum from tracker and muon chamber must be within three standard deviations of the tracker momentum. If this is the case the track is removed from the block and the algorithm proceeds with electron reconstruction and identification. Several criteria are placed on the shape and size of clusters and tracks. If the criteria are satisfied, the electron is identified and the elements are removed. For the remaining tracks, tighter quality criteria are applied, as these will likely correspond to charged hadrons which pass tighter criteria more easily while remaining fakes are cut by 90% by the additional cuts. Now charged hadrons are reconstructed and identified by the algorithm, after which the remaining clusters should correspond to photons and neutral hadrons. These last three steps are a bit more complicated and would require too much explanation for this section. More information can be found in [49].

4.5 Online data selection: Triggers

The rate of the proton-proton or heavy-ion collisions is very high at the LHC. With a beam interval of only $25ns$, the collision rate is $40MHz$. With multiple proton-proton interactions per beam collision, the pp interaction rate exceeds $1GHz$. The total information of a single event amounts to approximately $1MB$ and the electronics can provide a maximal bandwidth of $1GB/s$. A quick calculation shows that the maximal rate of events that can be stored is $1kHz$. Thus for every 40 million events, a mere thousand can be stored and on top of that, the selection has to be made without causing delay to the data-taking. This is where the trigger system comes into play [51]. The work in this thesis revolved mostly around triggers. Therefore the CMS trigger system is described in detail here.

4.5.1 The CMS trigger system

The CMS trigger system consists of two steps, the Level 1 Trigger(L1), and the High Level Trigger(HLT). Their goal is to select the events of potential physics interest within the bulk of inelastic collision events. The two-tier system works sequentially to reduce the rate of events. First, the L1 trigger reduces it to $100kHz$ after which the HLT brings it down to the required $1kHz$. Both levels are completely different in design. The L1 trigger consists largely of custom-designed electronics inside the detector. It uses raw data from the calorimeters and the muon system to make its decisions. The HLT, which has to handle drastically less events per second than L1, is software based. A server farm is able to execute reconstruction algorithms that are similar to what happens offline after data-taking. All types of particles can be identified, thus very little difference exists between HLT objects and offline analysis objects. The HLT program is regularly updated with new triggers and very diverse. The L1 trigger system shows some specific differences from what happens offline, due to the fact that the trigger decisions have to be made in such a short time-window.

4.5.2 The Level 1 system

Time is of the essence in the Level 1 trigger system. A fixed latency of $3.2\mu s$ is available for processing each event and deciding whether or not to keep it. The processing time is limited by the current technical limitations of the analog pipeline memories from the subsystems [?], because they have to hold the primitive data while the decision is being made. The L1 system relies on a lot of processes running parallel. Therefore its tasks are subdivided into specific fragments. At L1, The tracker information is left out completely. Its data is too elaborate and would take up too much time to calculate. The drastically more coarse information that the calorimeters and muon system provide are accessible. The composition of the L1 trigger system can be seen in figure 4.5. The calorimeters, ECAL, HCAL and HF and the muon detectors, RPC, CSC and DT (see previous section on muon systems) all operate separately to process their data during an event. This happens in several steps before the information is finally combined in the last step of the system, the Global Trigger (GT).

The calorimeter trigger consists of two stages, the regional calorimeter trigger (RCT) and the global calorimeter trigger (GCT). The ECAL, HCAL and HF send transverse energies and quality flags to the RCT. Here it is processed to create e/γ candidates and regional transverse energie (E_T) sums. e/γ candidates are ECAL signals that could be either electrons or photons. Normally they are distinguished by their tracker signature but tracker info is not used at L1 therefore they are indistinguishable and known as e/γ. The GCT sorts the e/γ candidates by p_{T} and forms jets using the E_T sums. It also calculates the transverse missing energy E_T^{miss}. Take note that this is not the physically correct E_T^{miss} as muons are not accounted for. The GCT sends four e/γ candidates to the GT, as

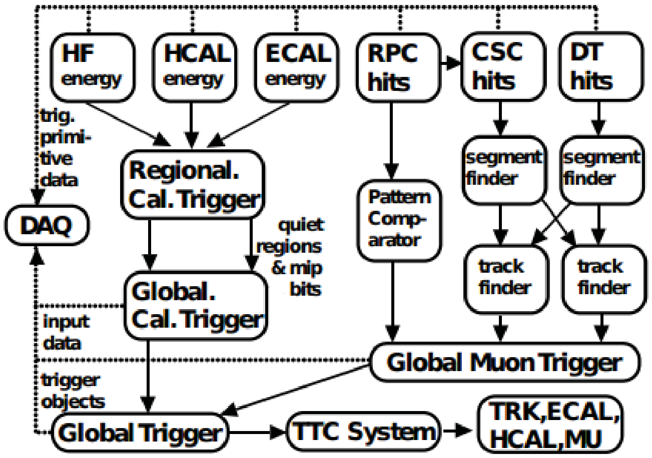

Figure 4.5: Overview of the dataflow in the CMS L1 trigger system [51].

well as four each of central jets, tau jets, forward jets and some other global quantities.

The muon detector systems operate slightly different. The Drift Chambers (DT) and Cathode Strip Chambers (CSC) send their data to regional track finders that use pattern recognition to identify muons. Their momenta is roughly measured from the curve of their track in the detectors. The Resistive Plate Chambers (RPC) are sent to pattern comparator trigger boards instead. They also identify muon candidates with their p_{T} . The DT and CSC track finder can talk to each other to find muons that overlap between the systems. The identified tracks, four tracks each from CSC and DT and eight from RPC, are sent to the Global Muon Trigger (GMT). The GMT eliminates muons that are double counted and performs further quality assurance before sending the muon candidates to the GT.

The GT is the final step of the L1 trigger system. The menu of triggers is implemented here. These consist of a set of selection requirements that are applied to the received list of objects. The requirements are based on the type of identified objects, their p_{T} , their direction in the detector and the quality they are assigned. The GT decides whether to accept or reject an event. This decision is sent to the respective detector parts that have kept their primitive data in pipelines waiting for the GT decision. If the event is accepted, the primitive data is sent off to the HLT system. If not, the information is dumped.

The available objects at L1 are limited. From the muon systems only muon candidates are collected. The calorimeter trigger system provides all the other types. This consists of the e/γ candidates, which leave their signature primarily in the ECAL, as well as central jets, tau jets which are primarily found in the HCAL, but whose ECAL deposits are counted as well. Forward jets are found in the HF calorimeter that encapsulates the end regions of the beamline. Finally E_T sums and E_T^{miss} are the last type of objects that are identifiable at L1.

The type of conditions that are applied in the GT range from the typical p_T threshold on objects to a defined range in pseudorapidity or azimuthal angle that the object has to be in, or even a certain difference in pseudorapidity or angle between two objects. A lot of these conditions return in several different triggers. Therefore they are verified separately, after which simple combinatorial logic forms the ultimate menu trigger decisions. The menu is restricted to 128 concrete algorithms. The limiting factor is the string of bits that the GT has to check before making its decision.

4.5.3 The High-level trigger system

At the High-level trigger [52], or HLT, the event selection is similar to the offline reconstruction process. The same type of objects, e.g. muons, electrons, jets,... are reconstructed and more complicated and stringent criteria than L1 are applied to obtain the final selection of events for data analysis.

The hardware of the HLT consists of a server farm with commercial computers running Scientific Linux. There are two types of computer units with a different purpose: filter and builder units. Builder units receive the event fragments coming from the individual detector parts and assemble them to form a complete event. An event is then taken over by a filter unit where the data is unpacked and the actual object reconstruction and trigger filtering happen at the same time. Builder and filter units communicate via shared memory space for increased processing speed. In total, the server farm consists of approximately 13000 CPU cores [53].

The input rate that the HLT can handle in order to conduct itself properly, is $100kHz$. This limits the output of the L1 trigger. Since 2012 (there was an upgrade in CPU power), the time budget for every event is $175ms$ allowing for event reconstruction that comes very close to offline standards [54]

The process of the HLT is very algorithmic. It is structured around HLT paths, a set of computing steps that are run in a predefined order. Physics object reconstruction and trigger decisions on those objects are alternated. The steps increase in complexity and level of refinement. Unlike at L1, all detector signals are used at HLT. This primarily means that the Silicon tracker will be used, allowing for more accurate reconstruction of objects since this is by far the most precise detector system of CMS. But in the HLT paths, the tracker reconstruction always constitutes the final steps of the path, as it is also the most time-consuming process. Since a significant number of events have been rejected by earlier decisions in the path, it can be allowed here.

As mentioned before, the size of a single event data sample is approximately $1MB$. The available bandwidth limits the output rate of the HLT system to a rate of $1kHz$. Events that are accepted by the HLT trigger system are sent to the storage manager, a process with the only task of storing the data. Eventually the data is transferred to the CMS Tier-0 computing center for offline processing [55].

4.5.4 Prospectives for 2017

In the summer of 2017, the LHC will operate at an increased luminosity compared to 2016. This has two effects, firstly pileup will increase, more secondary collisions will happen during each bunch crossing, increasing the amount of particle tracks in the detector and complicating subsequent reconstruction and identification. Secondly, the probability of a high energy interaction increases. The rate of events that will pass the triggers will increase conjointly. Since the rate is still limited by the bandwidth of the electronics, the trigger p_{T} thresholds will have to be raised. Table 4.1 gives an overview which triggers will no longer be kept at certain luminosities. For most analyses an increase in p_{T} threshold of the triggers is not a dire problem. However this puts a strain on the Heavy neutral lepton analysis discussed in the previous chapter. In several mass scenarios the p_{T} spectrum of the leptons was quite compressed. If the trigger thresholds are increased, this means that signal regions will be covered less and sensitivity will decrease. The next chapter explores a possible solution for this problem.

L1 trigger	**1.45e^{34}** $[cm^{-2}s^{-1}]$	**1.7e^{34}** $[cm^{-2}s^{-1}]$	**2.0e^{34}** $[cm^{-2}s^{-1}]$
Muon triggers			
L1_SingleMu22 OR 20er	✓	✓	✓
L1_DoubleMu_12_5	✓	✓	–
L1_DoubleMu_12_8 OR 13_6 OR 15_5	✓	✓	✓
L1_TripleMu_5_0_0	✓	–	–
L1_TripleMu_5_5_3	✓	✓	✓
L1_QuadMu0	✓	✓	✓
E/γ triggers			
L1_SingleIsoEG32er OR isoEG34 OR EG36	✓	–	–
L1_SingleIsoEG34er OR isoEG36 OR EG38	✓	✓	-
L1_SingleIsoEG36er OR isoEG38 OR EG40	✓	✓	✓
L1_DoubleEG_24_17 OR 25_12	✓	✓	✓
L1_TripleEG_18_17_8	✓	✓	✓

Table 4.1: A brief L1 Trigger overview for Muon and EG triggers from 2016 and plans for 2017 in higher luminosity scenarios [50]. $1.45e^{34}cm^{-2}s^{-1}$ was the peak luminosity used in 2016 and 1.7 and $2.0e^{34}cm^{-2}s^{-1}$ are scenarios that are expected in 2017 where the second one is the ideal scenario. This is not the entire L1 menu, but is meant to be indicative of the type of triggers and energy thresholds that exist at Level 1 and which ones can be held on to in 2017.

4.6 Event simulation

Just as essential as the data-taking of the CMS detector, is the correct simulation of the physics behind the events. Without a model that correctly describes the known physics and a theory that needs to be tested, the data would be a collection of meaningless numbers. Simulated events are useful in a variety of situations, e.g. to determine backgrounds or to predict signal yields for new physics phenomena. For all simulation purposes, the Monte Carlo(MC) technique lies at the basis. The Standard Model is proven to be a successful model thus it is used to simulate all processes that will happen during the proton-proton collisions. Simulations are not extremely important in this thesis and are thus discussed shortly.

The simulation of events happens in several steps, beginning with the hard process that forms the primary interaction vertex. Two protons are chosen that will collide. The partons are modeled using the parton distribution functions and the interacting partons are chosen by the Monte Carlo process. The actual process is then simulated resulting generally in several unstable particles whose subsequent decay is simulated next. Colored states, e.g. free quarks will undergo hadronization, a process in which the nature of QCD will give rise to the creation of quark anti-quark pairs until all final state hadrons are colorless states. This can be an elaborate process where the result can contain a large amount of particles. After all physics processes are simulated, it is necessary to simulate the detector reaction to the simulation, otherwise there is still no method to compare data and simulation. Again MC techniques are used to model the detector signals. Ultimately the same dataformat is reached as the one data-taking provides. The same reconstruction algorithms used on data are finally applied on the Monte Carlo samples. In the future, simulated events will often be referred to as MC events.

Chapter 5

Heavy Neutral Lepton Search Strategy

5.1 Heavy neutrino production process

In order to motivate the work done for this dissertation, it is necessary to know what the broader research subject is that is currently happening in the CMS research group at the UGent [62]. To recapitulate, it is still unclear if the SM neutrinos are Majorana particles or not. The Majorana nature could possibly explain the low masses of neutrinos through the seesaw mechanism. In that case, heavy Majorana neutrinos could exist in nature. They fall under the collective search for heavy neutral leptons. They would only couple with the SM through oscillation with the other neutrino species. As a result they would be very hard to detect as the cross section for their production is quite small. The production rate can be related to the coupling the heavy neutrino exhibits with reference to the SM neutrinos $|V_{N\nu}|^2$. Low coupling will indicate a smaller rate, but also a longer lifetime. The analysis that is being carried out by the Ghent group aims to exploit the longer lifetime by taking into account that the Majorana neutrino can travel a significant distance before decaying. By accounting for this, the sensitivity of the analysis is significantly enhanced.

The parameter space that can be studied at the LHC is restricted by the center-of-mass energy the accelerator can reach. Currently the LHC is operating at $\sqrt{s} = 13\,TeV$ but might scale up in the coming years to $\sqrt{s} = 14\,TeV$. As a result, the masses of the neutrinos that can be studied are confined to orders of magnitude ranging from $1-10^3 GeV$. The simplest production mechanism for Majorana neutrinos is displayed in Figure 5.1. W bosons are produced in great numbers at the LHC and provide the highest cross section to study neutrino production. The W decays into a charged lepton (e, μ or τ) and a Majorana neutrino, which in turn decays into a second W boson and a second lepton. Finally the W is allowed to either decay leptonically or hadronically, adding respectively a lepton and a SM neutrino or two jets from quarks to the event signature. The final state thus consists either of ($l^{\pm}l^{\pm}l^{\mp}\nu_l$), ($l^{\pm}l^{\pm}jj$) or ($l^{\pm}l^{\mp}jj$). There are only a small number of rare SM processes that produce similar final states, mainly due to the number of leptons, making this decay channel an exceptionally interesting one to study.

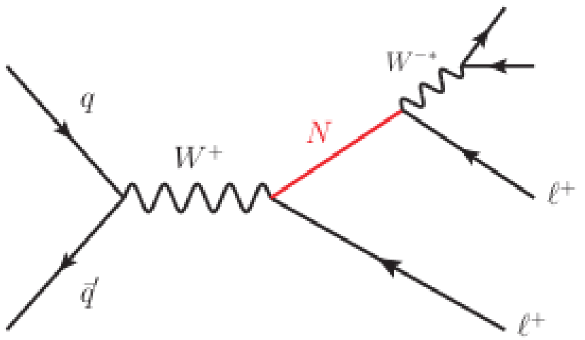

Figure 5.1: Heavy neutrino production channel at the LHC for masses of N below the mass of the W boson. When the mass of N is above the W mass, the first W will be a virtual boson and the second one will be a real W.

During the previous run of collisions at $\sqrt{s} = 7\,TeV$ and $8\,TeV$, there were already extensive searches for heavy neutrinos in the channel $(l^{\pm}l^{\pm}jj)$ at both CMS and ATLAS [56, 57, 58, 59, 60]. The channel $(l^{\pm}l^{\pm}l^{\mp}\nu_l)$ on the other hand has never been studied before. This provides a chance to explore an untouched region of the parameter space. On top of that, there is a novel aspect to the research that has not been executed before, accounting for the long neutrino lifetime and subsequent non-negligible travel distance before decaying. This means that the signature of the event will change considerably: only one lepton will originate from the primary vertex and the other two leptons or the lepton and 2 jets will originate from a secondary vertex a small distance removed from the primary one. Pile-up prevents us from looking at longitudinal displacements too close along the beam line since the secondary vertex could just as well stem from a completely different interaction. Therefore only displacements in the transverse plane will be considered. The new signature of the final state allows to significantly reduce the amount of background events. This technique would allow to look for Majorana neutrinos with coupling constant $|V_{N\nu}|^2$ orders of magnitude below previous searches. Figure 5.2 shows the extended reach of the two new analyses, next to the SHiP experiment [68], a planned experiment that also searches for heavy neutral leptons using the SPS at CERN. It gives an indication what reach could be achieved with the full Run II dataset that is expected to be available in a few years.

5.2 Triggers

In this thesis, two separate studies have been performed on the triggers used in the HNL analysis. The first study consisted of finding out whether or not a modified single lepton trigger could be designed that would better fit the need of the analysis, more specifically in the case of displaced vertices when the di- and trilepton triggers will have to be discarded.

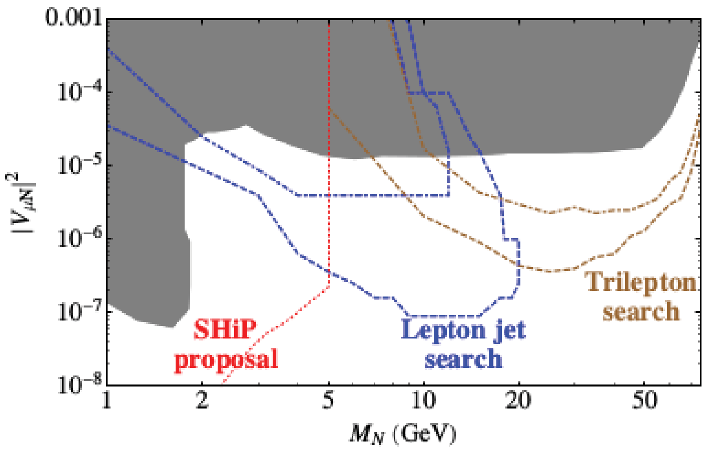

Figure 5.2: The grey area represents the excluded region of parameter space with 95% confidence level. Three experiments and their expected increased sensitivity are displayed. The red line shows the SHiP experiment [68]. The blue and brown line are relevant for this research. The dot-dashed lines represent the expected reach for $\sqrt{s} = 8\,TeV$ and $20fb^{-1}$, while the dashed lines represent $\sqrt{s} = 13\,TeV$ and $300fb^{-1}$ of data.

In the second part of this thesis, the efficiency of the triggers used by the current analysis of the final state ($l^{\pm}l^{\pm}l^{\mp}\nu_l$) are determined. The goal here was to determine whether simulation of the triggers happens correctly and they produce the same results as in data. Both studies are explained more in-depth in their respective chapters.

The triggers that are in use for analysis of the final state ($l^{\pm}l^{\pm}l^{\mp}\nu_l$) can be found in table 5.1. Events that pass any one of these triggers define the total dataset where the heavy neutral lepton search will be performed. The specific requirements are all mentioned in the name of a trigger, a simple example is HLT_IsoMu24 which requires a muon that passes $p_T > 24GeV$ and an additional isolation requirement. Most requirement names give a good idea what they do, e.g. 'CaloIdL' is a loose identification requirement on the calorimeter deposit.

5.3 Event reconstruction and identification

Muons and electrons are the important objects in this analysis, since the final state consists of three leptons and a neutrino. Tau's are not considered at this moment, although they could be added at a later point. In order for a muon or electron to be considered as a 'good' analysis object, it needs to pass several identification criteria. Three working points (WP) of increasing tightness are defined for different purposes, the Loose, Fakeable Object (FO) and Tight working points. The Loose working point is used for cleaning muons from electrons. Electrons are left out if they are too close to a loose muon in the detector, the limit is put at $\Delta R < 0.05$. The FO definition is used to determine the background of

# leptons	Trigger path
Single	HLT_Ele27_WPTight_Gsf HLT_IsoMu24 HLT_IsoTkMu24
Double	HLT_Ele23_Ele12_CaloIdL_TrackIdL_IsoVL_DZ HLT_Mu8_TrkIsoVVL_Ele23_CaloIdL_TrackIdL_IsoVL_DZ HLT_Mu23_TrkIsoVVL_Ele8_CaloIdL_TrackIdL_IsoVL_DZ HLT_Mu23_TrkIsoVVL_Ele12_CaloIdL_TrackIdL_IsoVL_DZ HLT_Mu8_TrkIsoVVL_Ele23_CaloIdL_TrackIdL_IsoVL HLT_Mu23_TrkIsoVVL_Ele8_CaloIdL_TrackIdL_IsoVL HLT_Mu17_TrkIsoVVL_Mu8_TrkIsoVVL_DZ HLT_Mu17_TrkIsoVVL_TkMu8_TrkIsoVVL_DZ HLT_TkMu17_TrkIsoVVL_TkMu8_TrkIsoVVL_DZ HLT_Mu17_TrkIsoVVL_Mu8_TrkIsoVVL HLT_Mu17_TrkIsoVVL_TkMu8_TrkIsoVVL HLT_TkMu17_TrkIsoVVL_TkMu8_TrkIsoVVL
Triple	HLT_Ele16_Ele12_Ele8_CaloIdL_TrackIdL HLT_Mu8_DiEle12_CaloIdL_TrackIdL HLT_DiMu9_Ele9_CaloIdL_TrackIdL HLT_TripleMu_12_10_5

Table 5.1: An overview of the HLT trigger paths that constitute the dataset used in the analysis.

non-prompt leptons. Lastly the Tight definition serves to define the signal region. The selection criteria that define the working points can be found in tables 5.2 and 5.3. These come from the analysis note on the Heavy neutral lepton analysis [62]. Some explanation of the requirements is necessary. The η cut limits the muons and electrons to the barrel and endcap regions. The p_T cuts have a significant effect on the signal efficiency, ideally they are as low as possible. The triggers do introduce limits on how low the cuts are possible. The cuts on d_{xy}, d_z and SIP_{3D} are related to the distance that the lepton originates from the primary vertex. d_{xy} is the distance in the transverse plane, d_z is the longitudinal distance and SIP_{3D} is the total distance d_0 divided by the uncertainty on the distance σ_d. The relative isolation I_rel is defined as the ratio of the scalar p_T sum of charged and neutral hadrons and photons in a cone $\Delta R < 0.3$ around the lepton, where the charged hadrons must originate from the primary vertex, divided by the transverse momentum of the lepton. The relative isolation is required to be small to reduce the contribution of non-prompt leptons. The concept of PF muon, global muon and tracker muon were explained previously in the section on reconstruction and identification in CMS. A POG medium muon is a baseline definition of a muon made by the muon Physics Object Group at CERN [69]. For electrons, the POG MVA ID is a multivariate discriminator used to identify electrons, more information can be found at [70]. The next four requirements are technical trigger-related variables. Lastly the conversion rejection requirement is used to exclude electrons originating from photon conversion and the number of missing hits limits the number of allowed missed hits in the tracker.

Cut	Loose	Fakeable Object	Tight
$\lvert\eta\rvert < 2.4$	✓	✓	✓
p_{T}	> 5	> 5	> 5
$\lvert d_{xy}\rvert < 0.05$ (cm)	✓	✓	✓
$\lvert d_z\rvert < 0.1$ (cm)	✓	✓	✓
$\mathrm{SIP}_{3D} < 4$	–	✓	✓
I_{rel}	< 0.6	< 0.6	< 0.1
is PF Muon	✓	✓	✓
is Global or Tracker Muon	✓	✓	✓
is POG Medium Muon	–	✓	✓

Table 5.2: Requirements to pass each definition of the muon selection[62]

Cut	Loose	Fakeable Object	Tight
$\lvert\eta\rvert < 2.5$	✓	✓	✓
p_{T}	> 10	> 10	> 10
$\lvert d_{xy}\rvert < 0.05$ (cm)	✓	✓	✓
$\lvert d_z\rvert < 0.1$ (cm)	✓	✓	✓
$\mathrm{SIP}_{3D} < 4$	–	✓	✓
I_{rel}	< 0.6	< 0.6	< 0.1
POG MVA ID ($p_{\mathrm{T}} <$ 15 GeV)	–	$> (-0.02, -0.52, -0.52)$	$> (0.77, 0.56, 0.48)$
POG MVA ID ($p_{\mathrm{T}} >$ 25 GeV)	–	$> (-0.02, -0.52, -0.52)$	$> (0.52, 0.11, -0.01)$
$\sigma_{i\eta i\eta} < (0.011, 0.011, 0.030)$	–	✓	✓
H/E $< (0.10, 0.10, 0.07)$	–	✓	✓
$\Delta\eta_{in} < (0.01, 0.01, 0.008)$	–	✓	✓
$\Delta\phi_{in} < (0.04, 0.04, 0.07)$	–	✓	✓
$-0.05 < 1/E - 1/p < (0.010, 0.010, 0.005)$	–	✓	✓
conversion rejection	✓	✓	✓
Number of missing hits	< 2	$== 0$	$== 0$

Table 5.3: Requirements for an electron to pass each of the defined working points. Two POG MVA thresholds are given for respectively 15, and 25 GeV . Electrons above 25 GeV or below 15 GeV are required to pass the corresponding working point, while a linearly decreasing cut between the two working points is applied to electrons with a p_{T} inbetween these values. For every MVA working point three values are given corresponding to electrons with $0 < \lvert\eta\rvert < 0.8$, $0.8 < \lvert\eta\rvert < 1.479$, and $1.479 < \lvert\eta\rvert < 2.5$.[62]

5.4 Baseline event selection

The signal region for the final state ($l^{\pm}l^{\pm}l^{\mp}\nu_l$) is defined by three leptons satisfying the tight working point criteria described above. But a set of additional requirements is set, aimed to reduce background contamination from SM processes that also produce this final state. The Majorana neutrino signal itself is a rare process, so the background has to be as minimal as possible for it to be distinguishable.

Events with three same sign leptons are excluded since the signal process produces two same-sign leptons and a lepton of the opposite sign. If the event contains a fourth FO lepton it is also vetoed to suppress processes that generally yield four leptons, e.g. ZZ. An algorithm exist that can identify b-quark jets, the Combined Secondary Vertex (CSV) algorithm [71]. If a jet in the event with $p_T > 25GeV$ passes the loose working point of this algorithm, the event is vetoed to reduce the background of the $t\bar{t}$ process.

On the three selected tight leptons, the p_T cuts are motivated by the triggers. They are put as low as possible where the triggers are still able to cover the signal region. In order of decreasing transverse momentum, the three leptons are called the leading, subleading and trailing lepton. They respectively have to pass a threshold of 15, 10 and 5(10) GeV, when the trailing lepton is a muon(electron). In the case of some configurations concerning flavour, the thresholds are adapted to conform to the trigger thresholds:

- For three electrons, either the leading and subleading electron need to pass $p_T > 19, 15GeV$ or the leading electron needs to pass $p_T > 30GeV$.
- For two electrons and a muon where the trailing lepton is an electron, either the trailing electrons $p_T > 15GeV$ or the leading lepton needs $p_T > 23GeV$.
- For two electrons and a muon, but where the trailing lepton is a muon, the case is split between whether the trailing muon has $p_\mathrm{T} <$ or $> 8GeV$. If $p_\mathrm{T} < 8GeV$, then the leading and subleading lepton need $p_\mathrm{T} > 25, 15GeV$. When the trailing $p_\mathrm{T} > 8$, either the leading one needs $p_\mathrm{T} > 23GeV$ or the subleading one needs $p_\mathrm{T} > 15GeV$.
- For one electron and two muons, if the trailing lepton is a muon, either the trailing muon has to pass $p_\mathrm{T} > 9GeV$ or the leading lepton has $p_\mathrm{T} > 23GeV$.

Two distinct analysis regions exist, one that is optimised for the low mass scenario's of the HNL, and one for the high mass scenario's. The split happens at the mass of the W boson. These regions are categorized further but these specific categories are no longer relevant to this thesis. In the low mass signal region, it is required that the missing transverse momentum $E_T^{\mathrm{miss}} < 75GeV$ to distinguish the HNL process, which has relatively low missing transverse momentum, from backgrounds such as $t\bar{t}$ and WZ processes where this variable can have rather large values. Secondly, the invariant mass of the three leptons M_{3l} must be smaller than $80GeV$. This is motivated by its suppression of $Z + \gamma$ and $DY + jets$, where the photon can originate from asymmetric external and internal conversions, meaning it is radiated by a real or virtual lepton and converts into a lepton pair, giving most of its energy to one lepton causing the other one to be below the selection thresholds. The three leptons that result from this will have an invariant mass approximately equal to the mass of the Z boson. Lastly events with a lepton pair of opposite-sign and same-flavour (OSSF) are vetoed. This reduces the size of the signal region greatly, but it cuts large background processes even more. Especially Drell-Yan + jets, asymmetric conversion and WZ backgrounds are reduced significantly because they always have an OSSF lepton pair. Lastly, the p_{T} of the leading lepton must be below $55 GeV$. This cut is meant to provide a distinction between the low mass and high mass region. If they are orthogonal to each other, the regions can be interpreted simultaneously which is advantageous.

The high mass region implements different cuts compared to the low mass region. The leading lepton p_{T} is now required to be above $55 GeV$. The subleading and trailing lepton p_{T} cuts are increased a bit, to 15 and $10 GeV$ to reduce the fake lepton background. Events with an OSSF pair are rejected if the invariant mass of two leptons M_{ll} closest to the Z boson mass, is within a range of $15 GeV$ around the Z mass. This rejects WZ background. For M_{3l}, the same off-Z requirement aims to reduce background from asymmetric internal and external conversions, mainly from Z + γ.

More information on event selection can be found in the analysis note of the HNL analysis [62]. For the study of the trigger efficiency, only the p_{T} cuts described here were implemented. The other cuts, designed to reduce background, would hinder the trigger efficiency study since for data the study will happen in a MET primary data set, formed by triggers for high missing transverse energy, while for MC it will be determined in WZ events, which would be cut almost entirely by these requirements. The chapter on the HLT trigger efficiencies will provide further information.

Chapter 6

A new non-inclusive Single Lepton Trigger

6.1 Motivation

As mentioned a couple times by now, a major concern for the Heavy neutral lepton search is the p_T-threshold of the lepton triggers. The analysis targets a wide range of possible masses for the Heavy neutral lepton, or HNL, going from 1 GeV up to 1 TeV. And while the high mass scenarios usually contain at least a hard leading lepton allowing the signal region to be easily covered by single lepton triggers, this is not the case for low mass scenarios or masses around the mass of the W. In the case of low masses, the leading p_{T} spectrum is dominated by the first W decay. The lepton originating here has a lot of phase space for itself since the HNL, due to its low mass, only takes up part of the phase space. The second and third lepton will be compressed since they come from a low mass HNL. If the mass of the HNL is close to the mass of the W, the HNL that needs to be produced leaves only a small window of phase space for the first lepton to decay in. The leading p_{T} spectrum will now be dominated by the third lepton from the second W decay. It is seen that in the low mass scenarios, the leading lepton p_{T} spectrum will look very much like the spectrum in W+jets events. The spectra are illustrated in figure 6.1 where several mass scenarios are simulated using MC. As a result of the compression, single lepton triggers are not able to completely cover the signal region. To increase the sensitivity of the analysis, di- and trilepton triggers are added to cover as much of the phase space as possible, inevitably complicating the analysis. In the next phase of the analysis, when the HNL is long lived, two of the leptons will originate from a vertex displaced from the beam axis and will not be reconstructed by the standard algorithms implemented in the triggers. As a result only single lepton triggers will be viable for providing data, or new multi lepton triggers must be designed that are adapted to account for the displaced vertex. To make matters worse, the L1 and HLT trigger thresholds will go up in 2017 to accomodate for the increase in beam luminosity. This contradicts the wish of the HNL search and will result in even less coverage of the signal phase space. The question is posed whether it is somehow possible to lower the p_T thresholds already at L1 without harming the phase space.

6.2 Back to back veto

The main idea is to look whether it is at all possible to lower the p_T -threshold at L1 of the single lepton triggers. Only the electron and muon channel are taken into consideration. Taus are briefly discussed at the end of this section but will not be included in this study. The single lepton triggers are defined as inclusive, meaning only one lepton passing the conditions is sufficient and the other objects are at that point obsolete for the trigger. This is exactly where the possibility for improvement might lie.

6.2.1 Single lepton production at the LHC

Hard leptons in the LHC arise from a variety of sources. The most important are described in what follows. The first and foremost source is through electroweak processes where W or Z bosons are produced and subsequently decay leptonically. Usually they are accompanied by jets formed by the remains of the proton breaking up and hadronizing. They are often the basis of searches for new physics. W's have a larger cross section in the LHC than Z's [65]. Furthermore the branching ratios into leptons are [9]:

$$BR\left(W \to l^{\pm}\nu_l\right) \approx (10.8 \pm 0.09)\,\% \tag{6.1}$$

$$BR\left(Z \to l^{\pm}l^{\mp}\right) \approx (3.3658 \pm 0.0023)\,\% \tag{6.2}$$

A lepton from a W decay is always accompanied by MET due to the neutrino. A Z boson decay produces leptons in pairs with opposite sign and same flavour. We will focus on preserving W+jets events.

Several other sources of leptons within the SM are mostly seen as background and are unwanted by the majority of analysis groups. These include photon conversion, where a photon interacts with the electromagnetic calorimeter material to convert into an electron-positron or muon-antimuon pair. If a track from another particle matches the produced lepton signal, it is wrongly identified as a good lepton. Misidentified hadrons can cause similar problems while they traverse the ECAL. Muons only suffer very little from these type of backgrounds as the muon chambers are never reached by other particles. These unwanted sources of leptons will further on be collectively referred to as fake or non-prompt leptons. The majority of fake leptons are from QCD events, a very large fraction of which appears in the detector as two jets, usually back to back, since momentum in the transverse plane must be conserved.

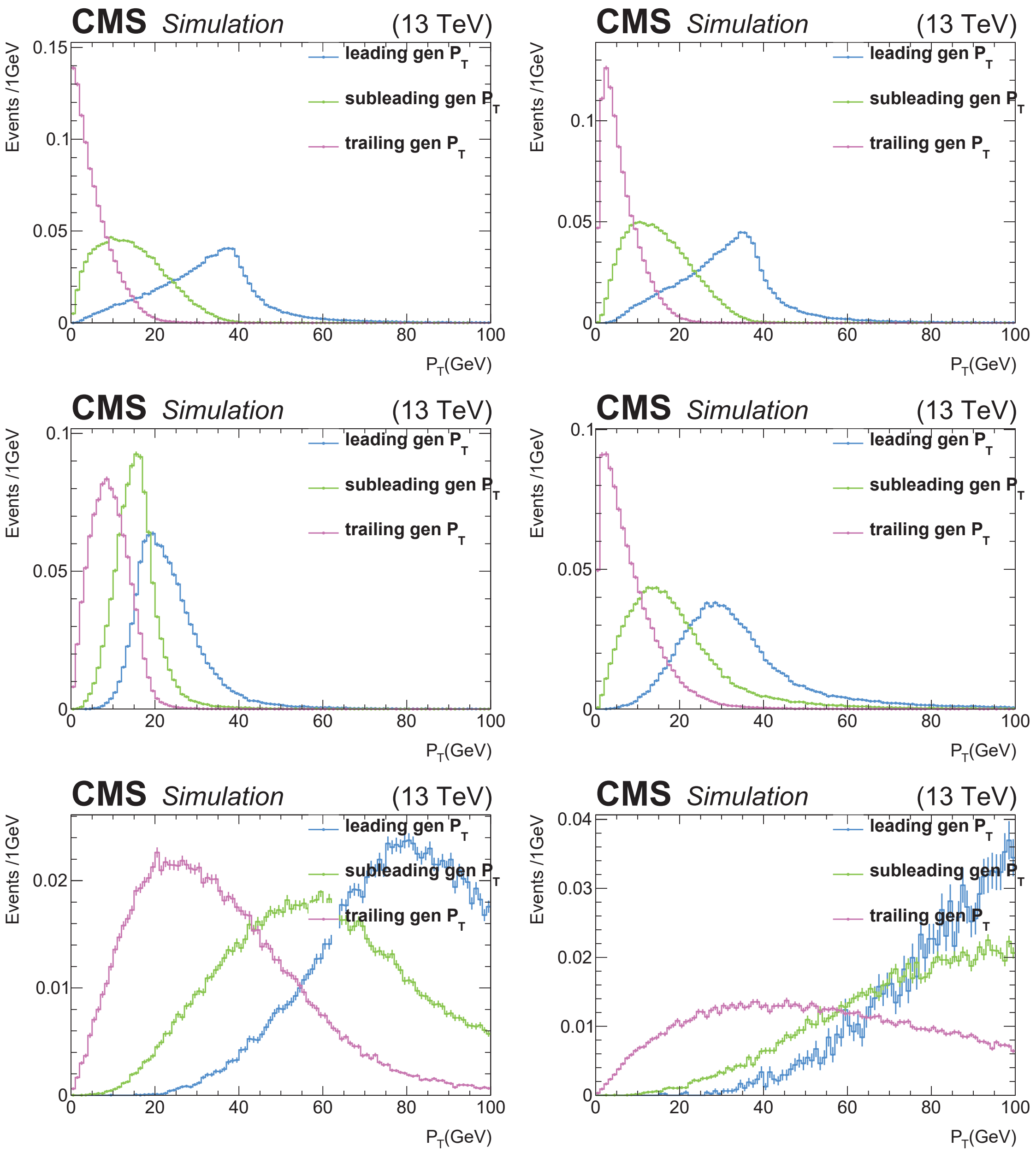

Figure 6.1: p_T spectrum of the three hardest generator-level leptons in the signal simulation of several HNL masses. From top left to bottom right the HNL mass scenarios for which the spectrum is shown are 5 GeV (a), 20 GeV (b), 60 GeV (c), 80 GeV (d), 200 GeV (e), 400 GeV (f) [62].

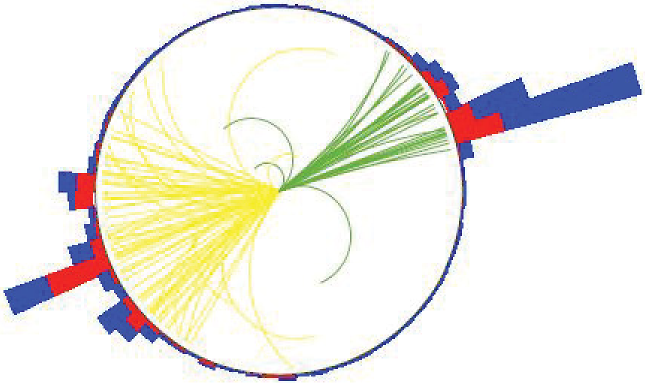

Figure 6.2: A sketch of tracks and energy depositions of two back to back jets

The tau triggers and reconstruction mechanism were only implemented at the beginning of Run II and reconstructing taus is a complex process. Their thresholds are even higher than for electrons and muons, which would indicate that they could certainly benefit from new trigger methods to lower these. The problem for tau triggers however lies elsewhere. Their efficiency at lower momentum is still very low as the taus are hard to distinguish from other jets. It does not make sense to do complicated advancements yet while the trigger algorithms can still be developed for better efficiency [66, 67].

6.2.2 Vetoing back to back events

An improved single lepton trigger would be able to distinguish between W+jets events and other dijet events. We propose to do this by introducing a back to back veto in the L1 trigger. The trigger will no longer be inclusive, but after finding a lepton with sufficient transverse momentum, will look for jets in the opposite direction of the lepton, called 'back to back' and nicely demonstrated in figure 6.2. If such a jet is found, the event will be rejected. This extra rejection mechanism will reduce the rate of the trigger, since more non-prompt leptons are rejected, allowing to compensate this by accepting leptons with lower p_{T} . The hypothesis behind this is that more dijet events are rejected than W+jets. This is far from an obvious point and requires extensive investigation.

6.3 Methodology

6.3.1 Zero bias and Minimum bias

In order to find out how a trigger performs on the data that LHC produces, a dataset is needed that represents the online environment without bias. Datasets collected by certain triggers are not suited since they are clearly biased by the triggers that were fired. CMS therefore employs triggers that randomly select events to store, specifically for this type of research. The first type is a ’zero bias’ trigger [63]. This is completely without bias and events, both inelastic and elastic collisions, are randomly selected. The cross section for elastic collisions is however orders of magnitude higher than inelastic collisions and dominates the dataset. This makes the zero bias dataset not feasible to study many regions of phase space.

Another trigger is introduced that employs a minimal selection, called minimum bias. Minimum bias tries to capture only non-single diffractive collisions. Collisions can be subdivided into four categories: elastic scattering, single diffractive, double diffractive and non-diffractive collisions. In elastic scattering both protons remain intact after collision and are seen in the detector as single tracks. Single diffractive means one of the protons is broken up by the collision but will still produce a collimated jet of particles. This jet is still identifiable as resulting from a proton. In double diffractive colllisions, both protons are broken up in the way explained for single diffractive. Finally, there are non-diffractive collisions, where both protons are broken up, but in the resulting detector signatures there is very little structure remaining. Particle tracks cover the entire detector. Double diffractive and non-diffractive interactions are collectively known as non-single diffractive interactions. The minimum bias trigger succeeds in detecting these events with good efficiency [63] by using the forward calorimeter (HF). This calorimeter covers the region $3 < |\eta| < 5$ at both ends of the beamline. If the HF entails a trigger tower with enough activity in both directions, the event is viable for minimum bias triggering. A large prescale is applied to the minimum bias trigger (as well as for zero bias) in order to manage the rate that fires the trigger. A prescale different from 1 means not all events that pass the trigger are stored. It determines a chance that an event is kept. For example, if the prescale of a certain trigger is 100, this means only 1 in a 100 events are stored.

The minimum bias dataset used in this analysis contains 20.7 million events. It consists of the minimum bias data gathered in 2016 for the high luminosity scenario that will likely be used in 2017. The bunches are spaced at 25ns. As the study will look at L1 triggers, the dataset contains both the RAW information available at L1 and the RECO information available after full reconstruction of the event. the RAW information is less accurate than RECO because at L1 the (partial) reconstruction of an event must happen before the next bunch crossing. It is still imperative for this study as the online decisions of triggers are made based on this information.

6.3.2 Simulation samples

This analysis uses additional monte carlo generated simulation samples. More specifically two processes are simulated. The W+jets process, where a W boson is produced in the proton-proton collision. The W will be accompanied by a number of jets, coming from the remainder of the proton, as well as initial state radiation (ISR) or final state radiation

(FSR). ISR and FSR are extra gluons that are radiated by resp. the initial state particles or the final state particles. Therefore this process is called W+jets. Secondly, Majorana neutrino processes, of the form of figure 5.1 were also generated by the Ghent particle physics group. Monte carlo samples with several Majorana masses were studied. This was done to make sure the analysis for which the new trigger is specifically developed, is not harmed.

6.3.3 Object identification

This section explains what offline criteria are required before objects in the detectors are accepted as valid analysis objects. At L1, the available objects are:

- Jets
- EG
- Muons
- Taus
- Missing Transverse Energy
- Energy Sums

Except for EG and Missing Transverse Energy, these objects are quite similar to what is available after reconstruction. Jets, Muons, Taus and Energy Sums need no further explanation. EG stands for 'Electron Gamma'. Since the tracker information is left out at L1 in order to save time, it is impossible to distinguish between electrons and photons at this stage. For the same reason, information from the muon chambers is not combined with information from the calorimeters. Therefore the L1 stage will use a form of missing transverse energy where muons are not taken into consideration. In this offline study, the missing transverse energy will be correctly recalculated using the calorimeter trigger towers and muon objects. The objects after reconstruction were described earlier.

A number of criteria are applied before an object is used for analysis. This is done in order to cut away background objects that arise in every event due to for example pile-up. Or leave out objects with less accuracy for example in the endcap part of the detector The three main objects used here are jets, electrons and muons. Jets are only considered if they have $p_T > 30GeV$ and $|\eta| < 2.5$. The p_{T} threshold has to be reasonable because the amount of jets increases quickly with lower p_{T} . The η condition makes sure only jets in the barrel and endcap detector are selected. Furthermore, jets are cleaned by requiring that no electrons or muons (that pass their corresponding criteria) are present in a range $\Delta R < 0.4$ around the jet. For electrons, on top of the basic requirements $|\eta| < 2.5$ and $p_T > 20GeV$, additional identification requirements are used. At L1, the only possible (and crude) identification requirement is related to the isolation of the ECAL signal, a variable called 'egIso'. At reco, electrons have three ID working points, loose, medium and tight. The medium working point is selected in this analysis as a good compromise between tightness of the identification and number of events passing the working point. Because it will be seen further that statistical uncertainties become a problem on the minimum bias dataset due to the low number of events passing the requirements on leptons. Lastly, muons are selected according to $|\eta| < 2.4$ (the muon chambers cover a marginally smaller range in $|\eta|$ than the calorimeters), $p_T > 20GeV$ and at L1 a variable muonQual, related to the quality of the tracks in the muon chambers, is required to be 8 or 12. These values indicate a medium (8) and tight (12) selection, respectively used in all present L1 dimuon triggers and L1 single muon triggers. At first sight, the values 8 and 12 seem arbitrary values, but the interstitial values were left open to leave the possibility for future design of intermediate working points. At reco, three working points are again available, loose, medium and tight and the medium one is chosen for the same reasons as for electrons.

6.4 Results

The idea for the improved trigger is to veto 'back to back events', by which events are meant that entail a lepton and a jet that are emitted in opposite directions. Before anything practical is designed a proof of principle is first needed. It has to be seen whether or not the new trigger excludes a sizeable fraction of W+jets events and lowers the efficiency too much. The Minimum bias and the W+jets datasets are central to this end. They are studied both at L1 and at reco. While the information at reco level gives a better insight in the physics behind the mechanism, the trigger will work with the less accurate L1 information. The proposed improvement needs to work on both levels.

6.4.1 P_{T} threshold

Previously, the p_{T} thresholds for the planned single electron and muon triggers were discussed. Now a working point needs to be chosen for the following study. This could later be adapted to more suitable values based on the rate of the trigger. The rate of a trigger is the amount of events that pass this trigger over time, as discussed in the section on the online data selection mechanism. Figures 6.3 and 6.4 show the p_{T} of the leading electron or muon in Minimum bias and W+jets events. Three curves are drawn, one where only one lepton is required, one with a lepton and one jet and finally one with a lepton and two jets. As the veto would require a lepton and a jet, it is interesting to see what fraction of events remains when additional jets are required.

It can be seen that the amount of events in Minimum bias increases rapidly with decreasing momentum, hence why the p_{T} thresholds have to be high enough. The plots of the L1 level also contain much higher number of events than reco level. This is due to the considerably looser ID criteria at L1. A lot of dijet events are able to pass the criteria at L1, especially at a p_{T} of $\approx 20GeV$. Meanwhile, in W+jets the amount of events is of the same order of magnitude at reco and at L1. The events with a leptonically decaying W have a hard clean lepton that is likely to also pass the medium working point at L1, so this is expected. The fact that there are so little events passing the medium working point at reco in Minimum bias is a first indication that the L1 level contains a lot of dijet events on top of the W+jets events. Another interesting thing to notice is that in W+jets, the events are peaked around 40 GeV, half of the mass of the W boson. This is expected as approximately half of the energy of the W will be transfered to the muon or electron in the decay. In the W+jets MC events this peak is very pronounced. But it appears as well at reco for Minimum bias, although it is quite small. Based on these arguments, the p_{T} working point was chosen at 30 GeV. This is below the threshold of single electron triggers and a little above the threshold for single muon triggers planned to be used in 2017. It reduces the amount of events significantly compared to 20 GeV but will leave a large fraction of W+jets as they are peaked around 40 GeV.

6.4.2 Number of Jets

Before taking a closer look at the kinematics of the lepton and jets, the number of jets that accompany a lepton are studied in more detail in figures 6.5 and 6.6. The piecharts detail the fraction of events at L1 level with a certain number of jets. The events are required to have an electron or muon with the previously established working point of 30 GeV. Both the number of cleaned jets (on the left) and the uncleaned jets (on the right) are shown. It is important to remember the cleaning only happens for leptons passing the ID criteria. As electron signals are counted as a jet at L1 but muons are not, it appears that the cleaned jets are generally shifted by one jet compared to the uncleaned jets for electrons. For muons the fractions are generally the same. The bin with 5 jets is used as an overflow bin, where events with more than 5 jets are also put in here.

Taking a look first at electrons, an important thing that is directly noticed, is that half of the events in W+jets do not include any cleaned jets. This can be explained by the p_{T} and η cut. Either the jets fall below the p_{T} cut of 30 GeV or they fall outside of the $|\eta|$ range of 2.5. Approximately half of the W+jets events has no cleaned jets. These will be included in the trigger since the veto can not apply on these events. A second important thing that these piecharts show is that W+jets has a larger fraction of events with 2 uncleaned jets than Minimum bias, 28.4% vs 23.8%. These are important as 2 hard jets generally should mean that they are back to back in the transverse plane of the detector. It might thus be assumed that W+jets will have more back to back events than Minimum bias. This will turn out not to be the case, and could be explained by other lower p_{T} jets present in the event and the presence of transverse missing energy from the neutrino. For muons, generally the same conclusions can be drawn as for electrons. Half of the W+jets events have no jets above 30 GeV and the fraction of events with 2 jets is

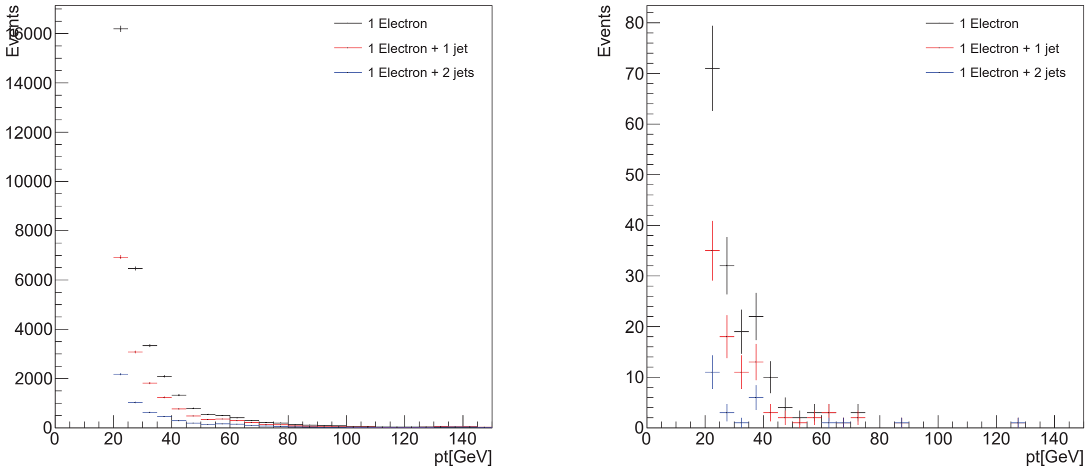

(a) Minimum bias L1 **(b)** Minimum bias reco

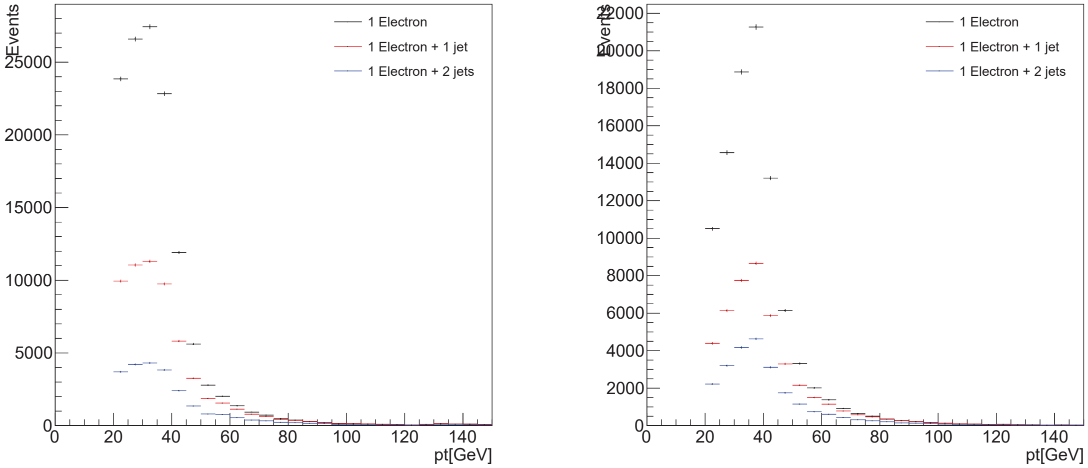

(c) W+jets L1 **(d)** W+jets reco

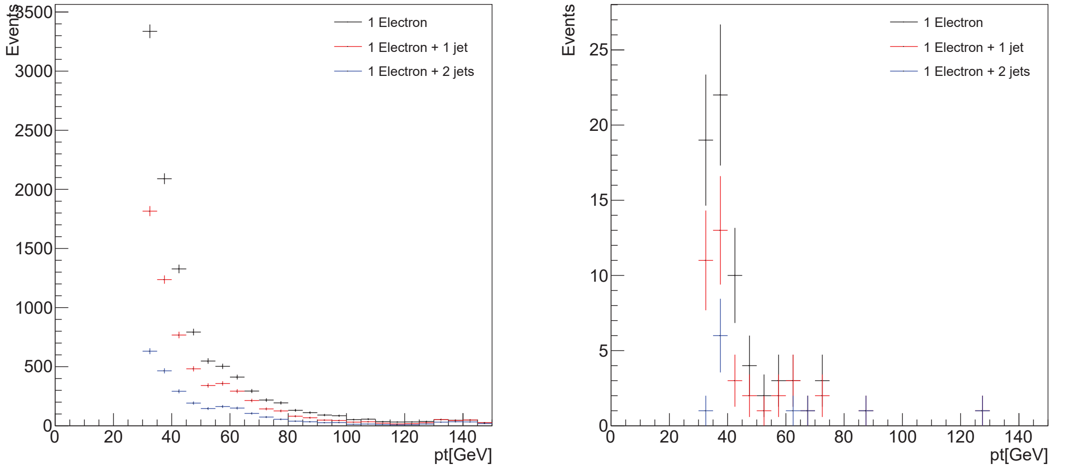

(e) Minimum bias L1 **(f)** Minimum bias L1

Figure 6.3: Leading Lepton p_{T} for electrons, with the threshold at 20 GeV for (a),(b),(c),(d) and at 30 GeV for (e),(f)

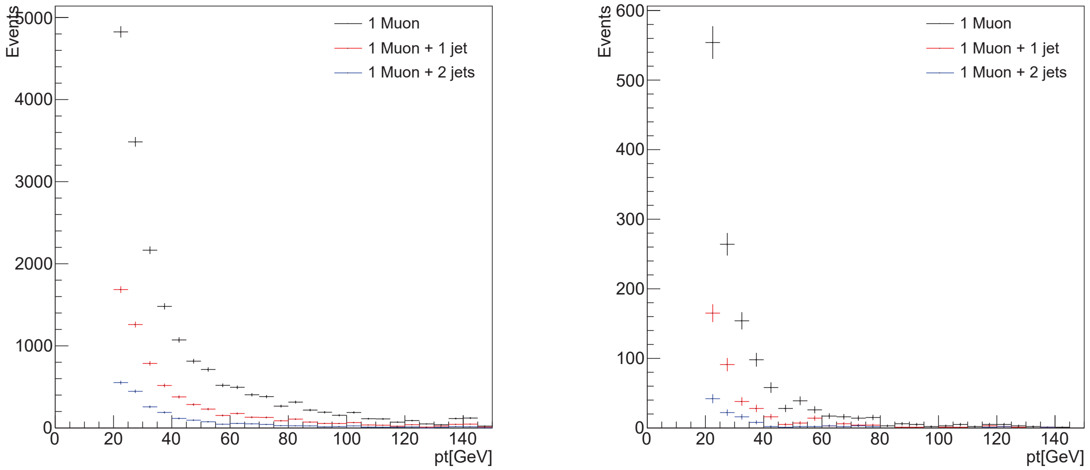

(a) Minimum bias L1 **(b)** Minimum bias reco

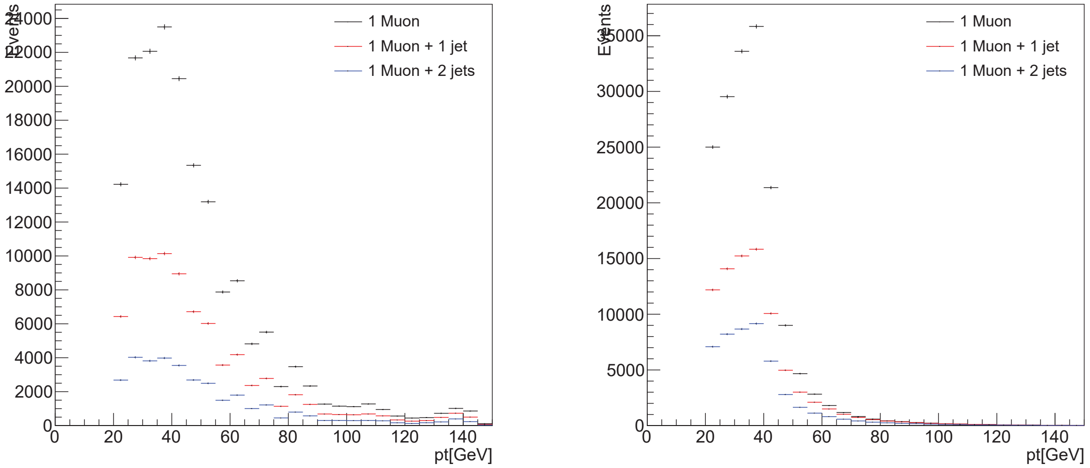

(c) W+jets L1 **(d)** W+jets reco

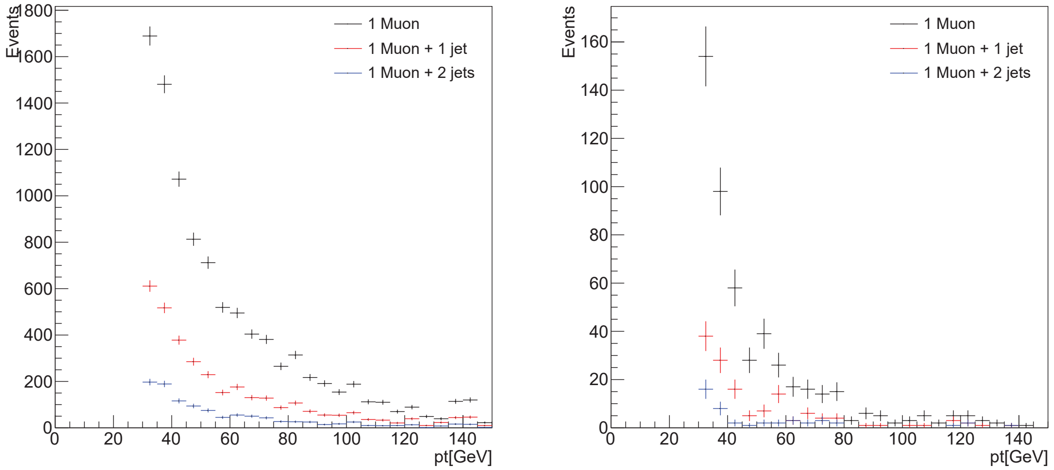

(e) Minimum bias L1 **(f)** Minimum bias L1

Figure 6.4: Leading Lepton p_T for muons, with the threshold at 20 GeV for (a),(b),(c),(d) and at 30 GeV for (e),(f) [62]

here approximately the same, 27.2% vs 27.4%.

6.4.3 Kinematics

In order to study the relative kinematics of the lepton and jet, at least one jet is required together with an electron or muon. Figure 6.7 shows the difference in ϕ, η and R for the leading jet and lepton in the event. The plots of the difference in pseudorapidity, $\Delta\eta$, do not provide new information but are included in order to provide a complete picture. R can be calculated by $R = \sqrt{\phi^2 + \eta^2}$. For electrons, the $\Delta\phi$ plots show something promising. At values of $\Delta\phi$ close to π, indicating back to back orientation in the transverse plane, both the minimum bias and W+jets dataset begin to show a peak. But this peak is more pronounced in minimum bias. This would mean that by excluding events when $\Delta\phi$ reaches a certain value, it would be possible to increase the fraction of W+jets events in minimum bias. This is a positive result, although it is important to keep in mind that W+jets also features a peak, and the danger would consist of cutting away a large fraction of W+jets, even though minimum bias would become more 'pure'. The muon $\Delta\phi$ plot features the same kind of peaks at high values, although less pronounced. Unfortunately, minimum bias does not seem to have a larger peak than W+jets as was the case for electrons. This indicates already that the dijet veto will not be feasible in the muon case. The difference between both leptons could be explained by the fact that electrons are expected to have more background from other types of events than muons as was mentioned already.

The ΔR plots lead to essentially the same conclusions that were already drawn. The electrons have a larger peak in minimum bias than in W+jets for the back to back topology. Muons do not show this behaviour. It can be seen that $\Delta\phi$ appears to be a better discriminator than ΔR, the discrimination between signal and background in minimum bias is clearer for $\Delta\phi$. This variable could provide a handle to distinguish between W+jets events and dijet events for electrons.

A problem with $\Delta\phi$ as a discriminator between W+jets and dijets, is that for higher p_{T} jets, the topology is expected to be increasingly more back to back, because for example for W+jets, if a jet is going in one direction with high momentum, the W has the same momentum in the opposite direction. After decaying, the lepton and neutrino should combine to have the same momentum. The lepton is therefore likely to be ejected somewhere in a cone around the momentum of the W. For increasing p_{T} of the jet, this cone becomes smaller and the lepton and jet become increasingly more back to back. Figure 6.8 clearly demonstrates this effect. The events are classified according to the p_{T} of the leading jet. With increasing jet p_{T} the peaks become larger both in minimum bias and W+jets. For jets with p_{T} higher than 70 GeV, it is unreasonable to still apply a veto for back to back events as almost no W+jets events would survive. It is questionable whether or not it should be applied for jets above 50 GeV. This limits the potential for

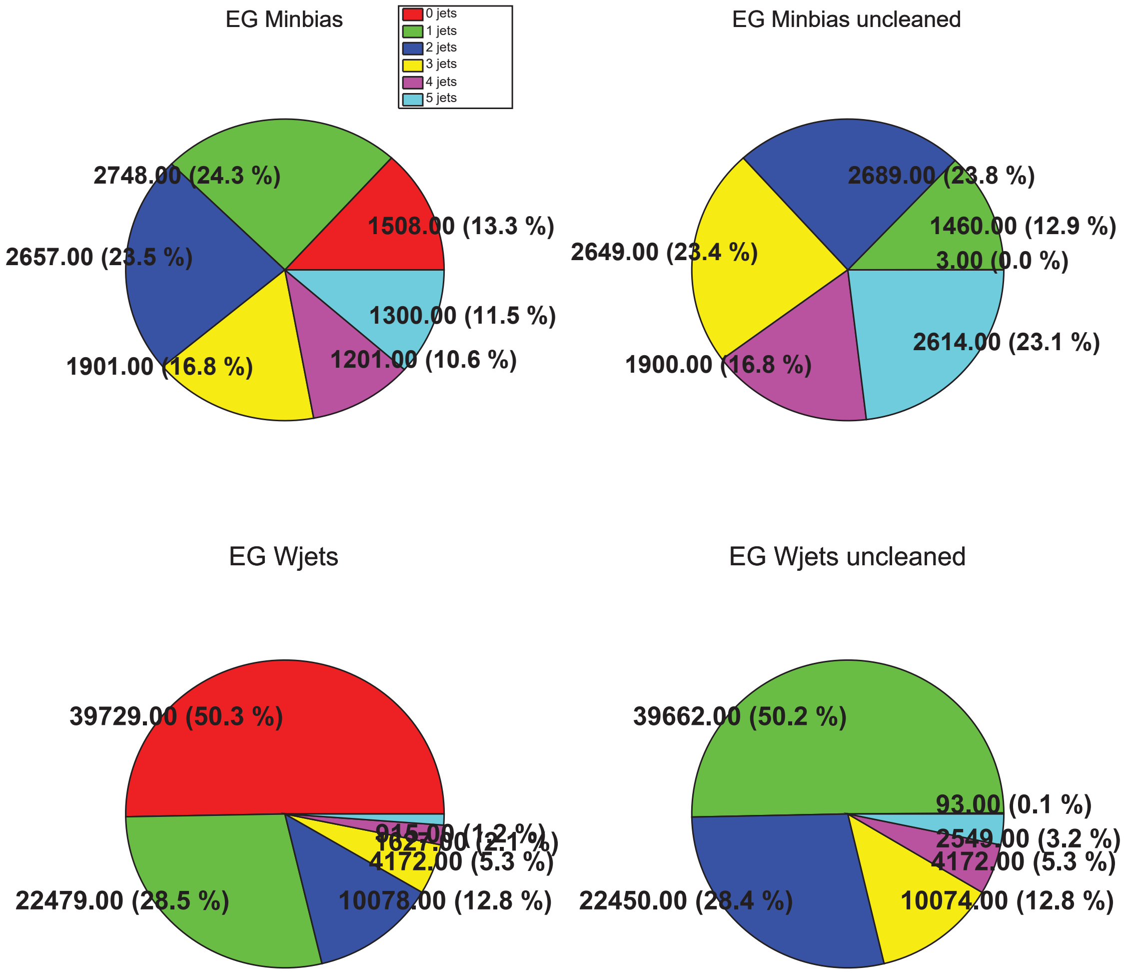

Figure 6.5: The number of jets that accompany an electron, called EG (Electron Gamma), the way they are detected at L1. plots (a) and (c) show cleaned jets, plots (b) and (d) show uncleaned jets.

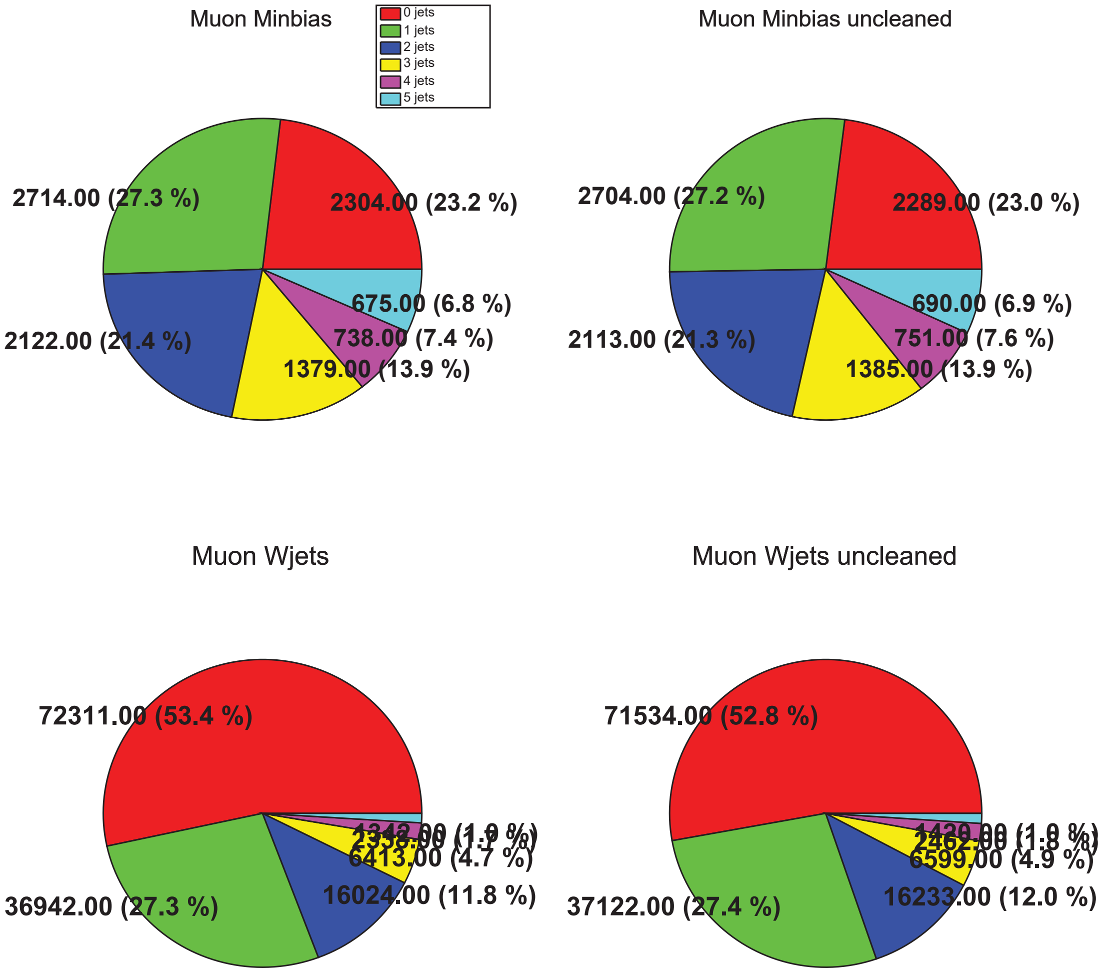

Figure 6.6: The number of jets that accompany a mouon at L1. plots (a) and (c) show the cleaned jets, plots (b) and (d) show uncleaned jets.

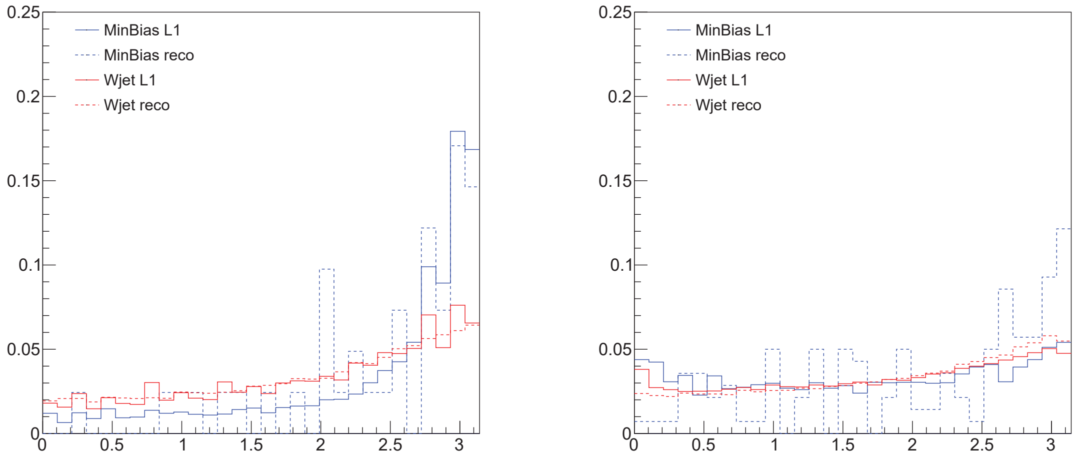

(a) Electron $\Delta\phi$ **(b)** Muon $\Delta\phi$

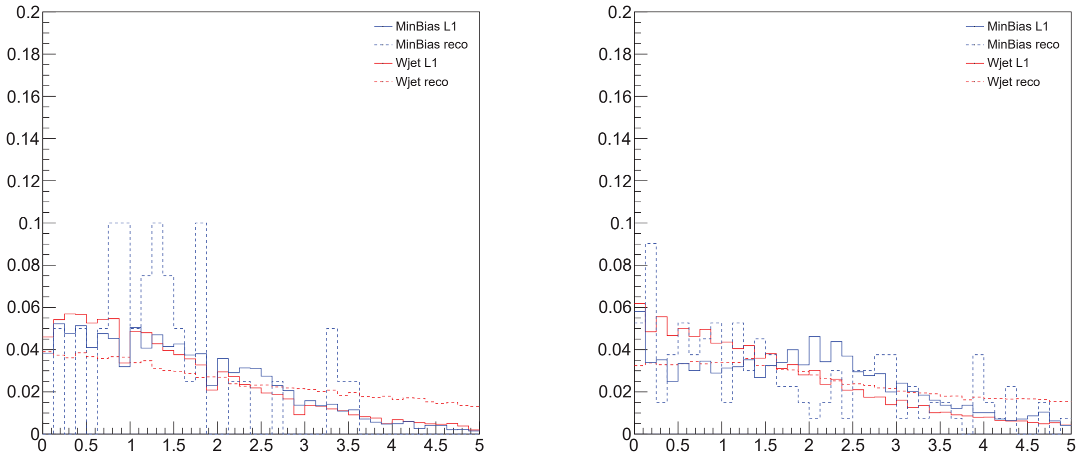

(c) Electron $\Delta\eta$ **(d)** Muon $\Delta\eta$

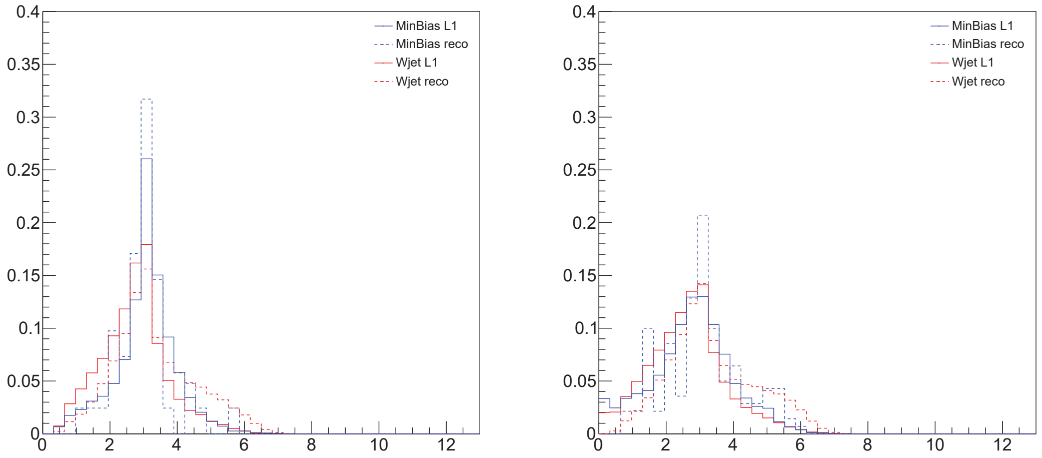

(e) Electron ΔR **(f)** Muon ΔR

Figure 6.7: Relative orientation of leading lepton and leading jet.

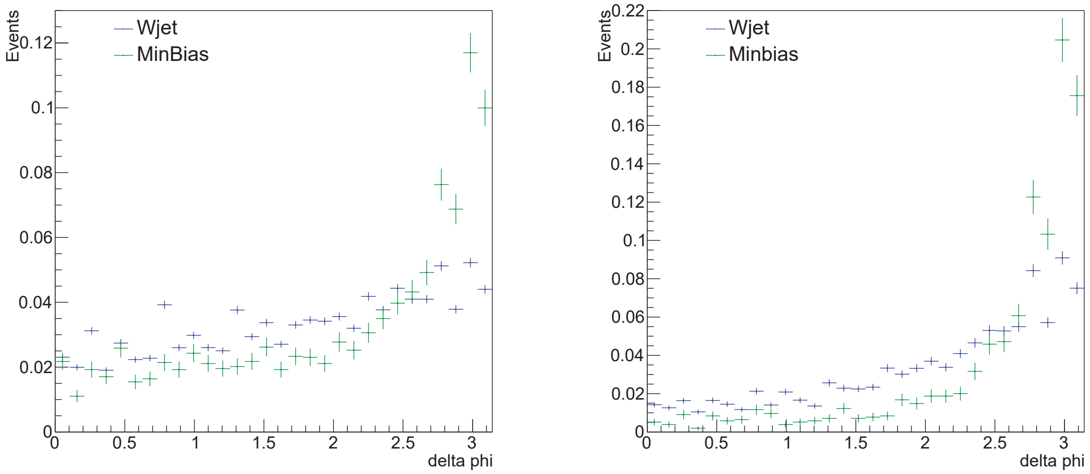

(a) $30GeV < P_T < 50GeV$ **(b)** $50GeV < P_T < 70GeV$

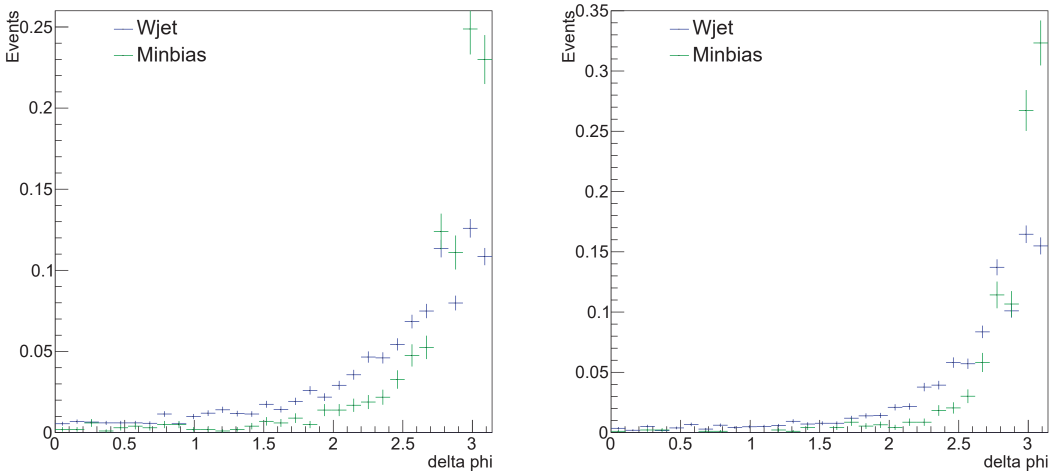

(c) $70GeV < P_T < 100GeV$ **(d)** $100GeV < P_T$

Figure 6.8: $\Delta\phi$ between electron and jet. The p_{T} of the jet has been divided in four regions: $30GeV < P_T < 50GeV$, $50GeV < P_T < 70GeV$, $70GeV < P_T < 100GeV$ and $100GeV < P_T$.

rate reduction again, the distinction between W+jets and dijet events can only be made with moderate p_{T} jets. Figure 6.9 shows the p_{T} division for muons. Something strange happens here. For high energy jets, it would be expected that the peaks at high values of $\Delta\phi$ are much more pronounced. They remain however relatively equally spread over different values. No satisfying explanation for this effect was found.

6.4.4 Transverse Mass

From the figures of the transverse momentum of the lepton it was already cautiously deduced that a considerable fraction of events in minimum bias with a lepton passing ID criteria is W+jets. This assertion can be made harder by calculating the transverse

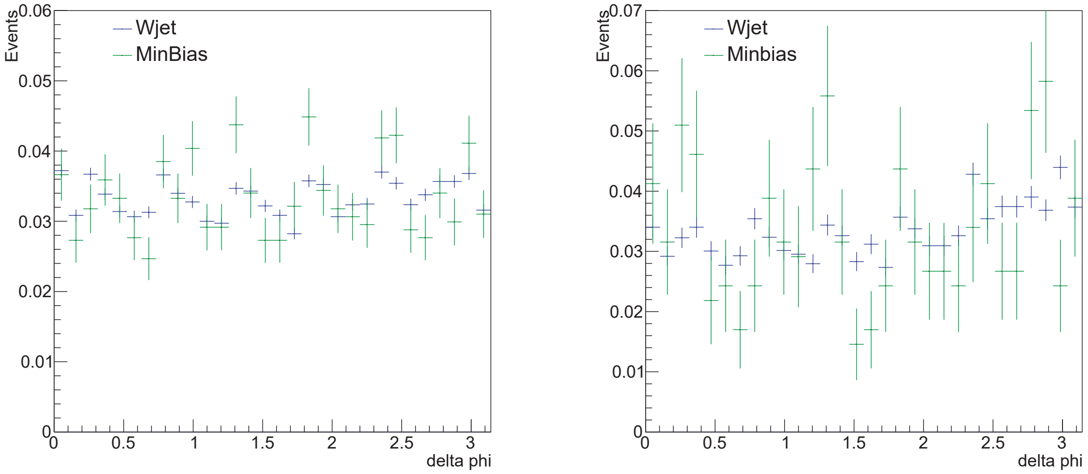

(a) $30GeV < JetP_T < 50GeV$ **(b)** $50GeV < JetP_T < 70GeV$

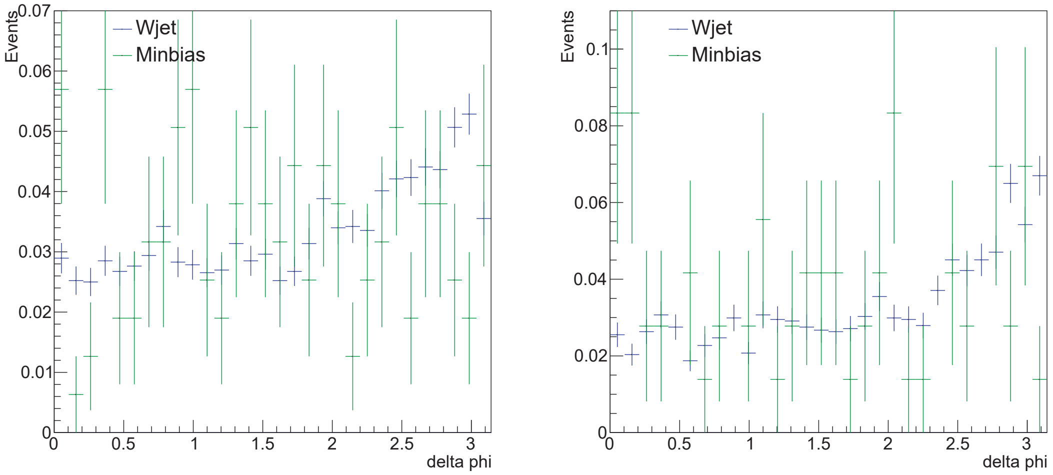

(c) $70GeV < JetP_T < 100GeV$ **(d)** $100GeV < JetP_T$

Figure 6.9: $\Delta\phi$ between muon and jet. The p_{T} of the jet has been divided in four regions: $30GeV < P_T < 50GeV$, $50GeV < P_T < 70GeV$, $70GeV < P_T < 100GeV$ and $100GeV < P_T$.

mass of the combination of the lepton and the missing transverse energy. A leptonic decay of the W produces an electron or muon (or tau, which is not considered here) and its corresponding neutrino. The neutrino leaves the detector as a source of missing transverse energy. Therefore the transverse mass of lepton + MET should give the mass of the W boson, being $\approx 80.4GeV$. At L1, two options are possible for MET, one that includes the forward calorimeter and one without. The first one is chosen because it is more complete and the MET at reco level also incorporates the forward calorimeters. Figures 6.10 and 6.11 show the transverse mass in four situations: Lepton with $p_{\mathrm{T}} > 30$ GeV, lepton with $p_{\mathrm{T}} > 30$ and a jet (which always satisfy $p_{\mathrm{T}} > 30$ GeV), lepton with $p_{\mathrm{T}} > 20$ GeV and finally lepton with $p_{\mathrm{T}} > 20$ GeV and a jet.

In the electron case, it becomes clear that the statistics are very small at reco for minimum bias. Unfortunately this already uses the complete dataset for minimum bias. If more data would be available, a quantitative answer might be possible to the question what the fraction of W+jets events in minimum bias is. This could be done by making a fit of the transverse mass spectrum of minimum bias where one lepton is selected to the curves from W+jets and the complete minimum bias, which can be considered to be dominated by QCD events. The low statistics only allow for a qualitative conclusion. The muons have a little better statistics, but not enough to draw more than qualitative conclusions. Figure 6.10a and 6.10b show decent overlap between minimum bias and W+jets. At L1, where a lot more events remain due to loose ID, the curve is shifted to lower values and smeared out a bit. This indicates that other types of events contribute sizeably. Figures 6.10c and 6.10d where the electron p_{T} threshold is lowered to 20 GeV shows a shift to even lower values, indicating even more background events. This matches the conclusions that were drawn from figure 6.3. Lowering the p_{T} threshold results in a lesser fraction W+jets events in minimum bias. This is a fact that works in the favor of the inclusive single lepton triggers that will raise their p_{T} threshold in the coming run of LHC.

Figure 6.11 shows that muons consist of a higher fraction W+jets, because the curves in 6.11a and 6.11b do not show the shift to lower values that were found for electrons. The curve is still smeared out a bit. Figures 6.11c and 6.11d feature a little shift that can be attributed to the lower p_{T} threshold and the same effect as seen with electrons.

6.4.5 Efficiency

The performance of a trigger that requires a lepton, a jet and a prototype of the dijet veto are determined here. The dijet veto is implemented by requiring the difference in azimuthal angle between the lepton and jet to be $\Delta\phi < 2.5$ and in a second prototype the value is chosen to be $\Delta\phi < 2.7$. In the section on kinematics, it was seen that at high p_{T}, this veto would exclude the majority of lepton + jet events, both in minimum bias and in W+jets. In W+jets we want to keep as many events as possible. The remaining

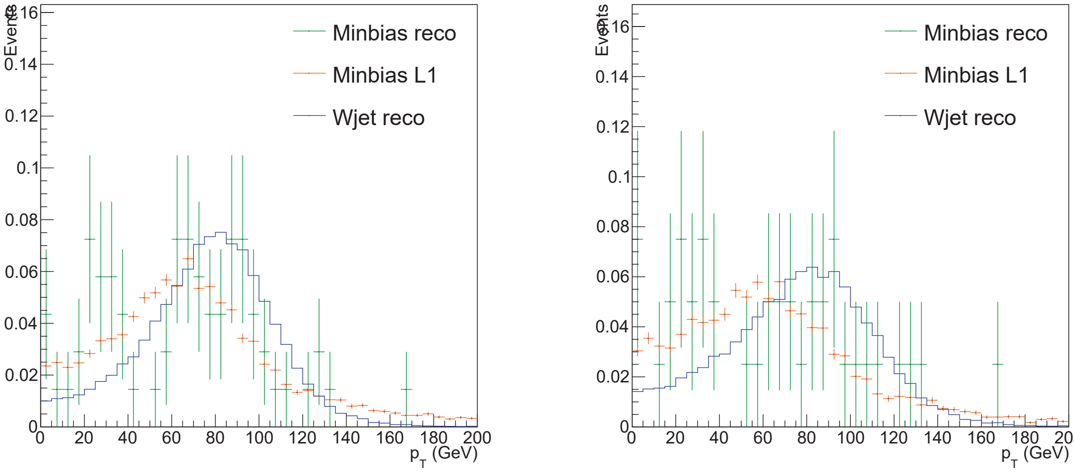

(a) Electron $p_{\mathrm{T}} > 30$ GeV **(b)** Electron $p_{\mathrm{T}} > 30$ GeV, Jet $p_{\mathrm{T}} > 30$ GeV

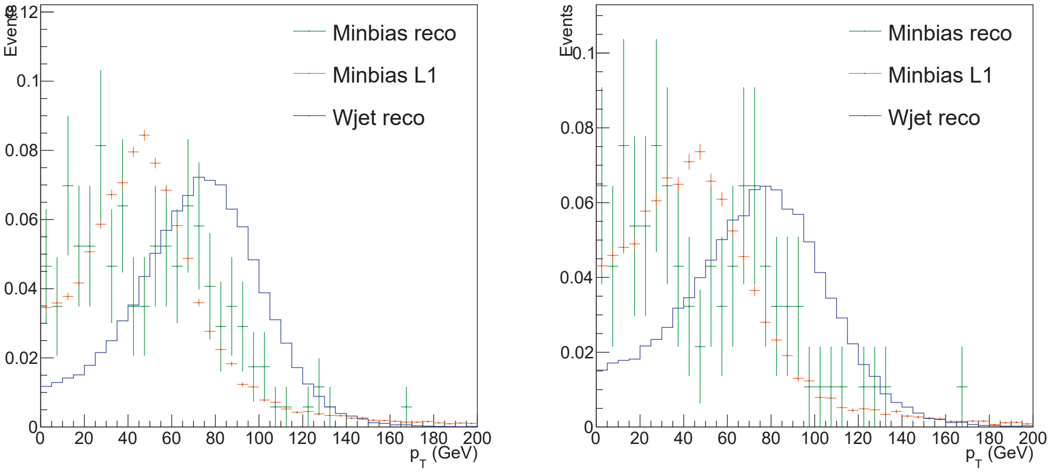

(c) Electron $p_{\mathrm{T}} > 20$ GeV **(d)** Electron $p_{\mathrm{T}} > 20$ GeV, Jet $p_{\mathrm{T}} > 30$ GeV

Figure 6.10: The transvers mass of muon + MET. This gives a qualitative indication of the amount of W+jets events in minimum bias.

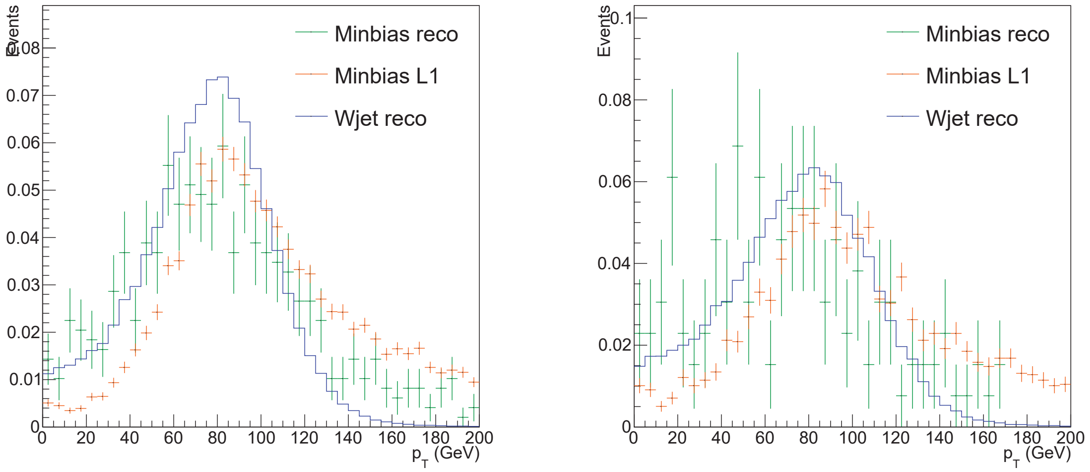

(a) Muon $p_{\mathrm{T}} > 30$ GeV **(b)** Muon $p_{\mathrm{T}} > 30$ GeV, Jet $p_{\mathrm{T}} > 30$ GeV

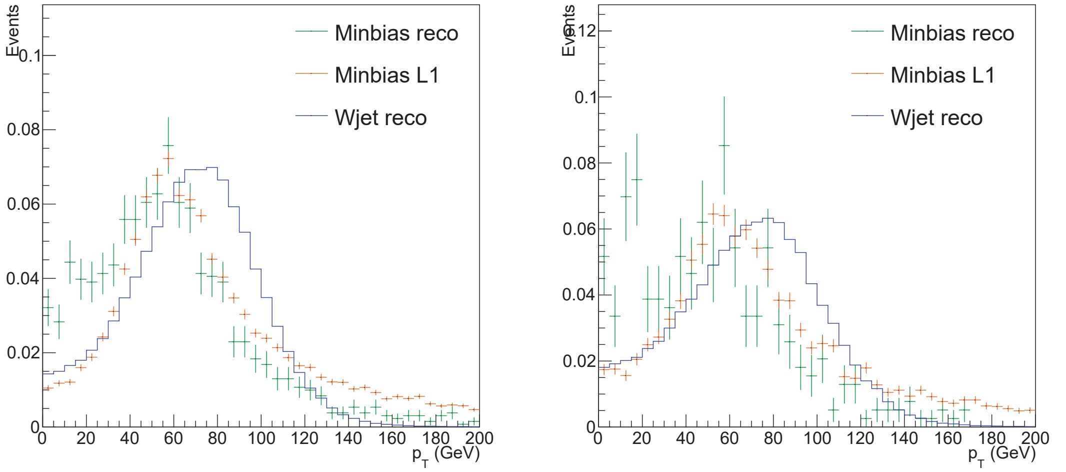

(c) Muon $p_{\mathrm{T}} > 20$ GeV **(d)** Muon $p_{\mathrm{T}} > 20$ GeV, Jet $p_{\mathrm{T}} > 30$ GeV

Figure 6.11: The transvers mass of muon + MET. This gives a qualitative indication of the amount of W+jets events in minimum bias.

fraction of lepton + jet events after applying the veto can be determined by comparing it to the efficiency that a lepton + jet trigger without the veto would have.

In Figure 6.12 and 6.13, the blue curve shows the efficiency of a lepton + jet trigger without a dijet veto, as a function of lepton p_{T} . The efficiency of a trigger is the ratio between the amount of events that are accepted by that trigger and the amount of events that, after offline reconstruction, contain the required physical objects and satisfy the conditions of that trigger. In the ideal case, the efficiency of a trigger equals 1 everywhere, meaning all events that should have fired the trigger, did so. But due to the less accurate reconstruction that happens online compared to offline, the efficiency will be worse most of the time. To be clear, this is not the efficiency of an existing trigger, but is a construction of a trigger using the L1 data. No actual trigger bit information was used.

The typical pattern of the efficiency as a function of p_{T} is followed by the blue curve. At the p_{T} threshold defined by the trigger, or very close to it, the efficiency starts out low, but rises steadily with increasing p_{T} . Eventually it approaches 1 or a value close to 1 for high p_{T} and remains constant after that. Now we want to compare what remains of the events with a lepton and jet if the dijet veto is added. To get an indication of how much W+jets events are thrown away by the veto, we should look at the ratio between the amount of events that pass the dijet veto trigger at L1 and the amount of events that, after offline reconstruction, contain the objects and satisfy the conditions of the trigger but without the dijet veto. By using this ratio, we have accounted for the efficiency of a normal lepton + jet trigger being different from 1 and we can determine clearly what fraction of W+jets is excluded by comparing with the efficiency curve of the lepton + jet trigger.

The results of the dijet veto trigger prototypes are drawn as the red and cyan curves in figures 6.12 and 6.13. First looking at electrons, the fraction of W+jets events is lowered significantly by both vetos. The important indicator is the difference in value between the blue curve of the efficiency and the curves of the dijet veto triggers. Only for a small window in lepton p_{T} is the difference between the additional dijet veto and normal trigger reasonable. Even from momenta of 50 GeV it has already become quite large. This is another motivation to stop applying the veto at a certain p_{T} threshold. While previously this was shown for momentum of the jet, these figures make the same point for momentum of the lepton. The best scenario for a dijet veto should probably apply a threshold to both momenta after which the veto should not be applied anymore.

6.4.6 Conclusion

At this point in the investigation, it was decided to stop the development of the dijet veto trigger. Several arguments combined led to the conclusion that the idea is unfeasible after all. To summarize, the number of jets accompanying a lepton showed that half of W+jets

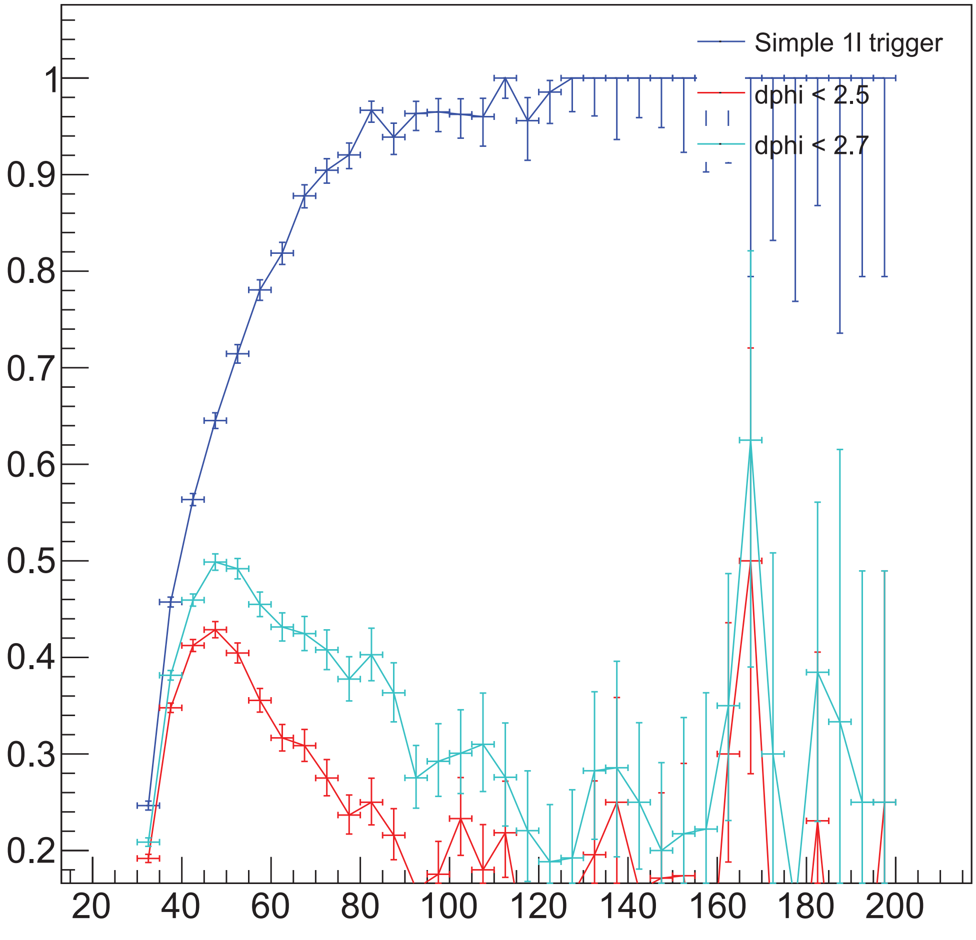

Figure 6.12: Efficiency of a normal single electron plus jet trigger and two prototype dijet veto triggers for electrons as a function of electron p_{T}

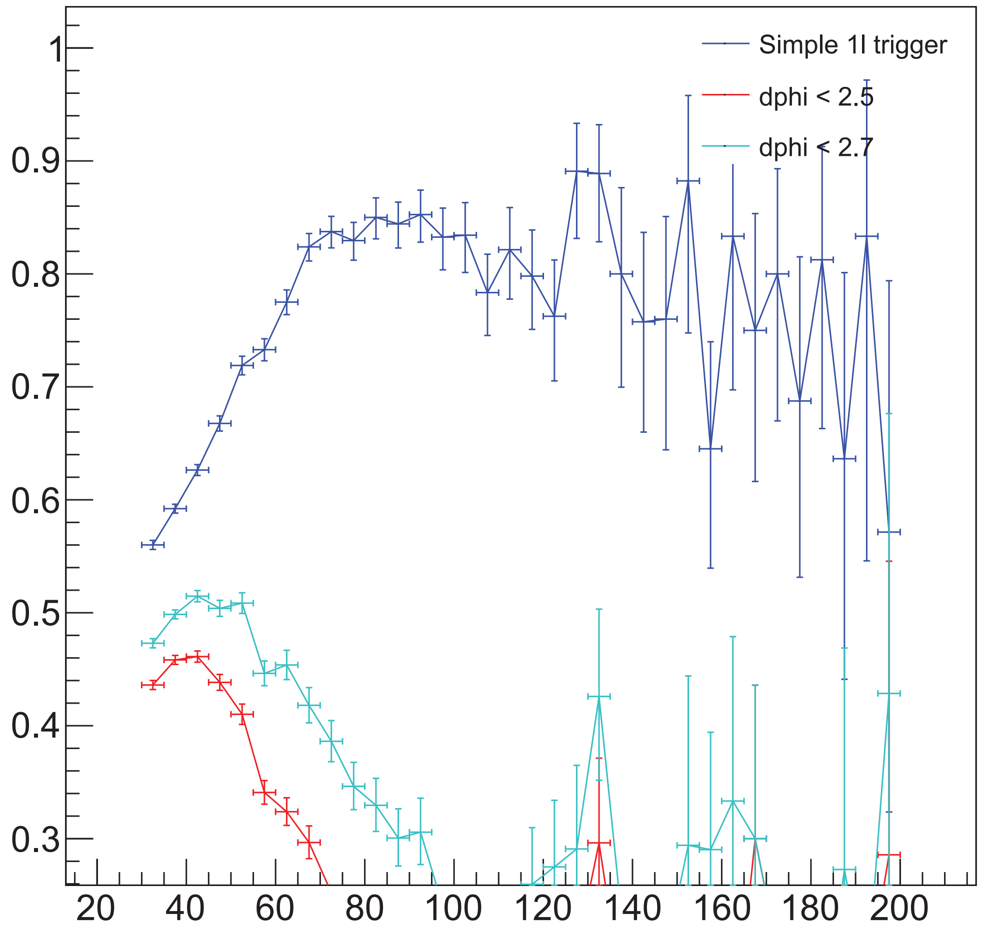

Figure 6.13: Efficiency of a normal single muon plus jet trigger and two prototype dijet veto triggers for muons as a function of muon p_{T}

events had no jet with moderate p_{T} . This meant that it was not possible to exclude events with a lepton and no jet. Next, the division of the jet p_{T} in bins showed that events become more back to back for higher p_{T} and, combined with the efficiency plots showed that the dijet veto could only be applied for a small interval of lepton and jet p_{T} up to approximately 50 GeV. For muons the $\Delta\phi$ plots showed that there is no possibility to improve the fraction of W+jets in minimum bias. For electrons, there is a possibility. Nevertheless, the combination of all these limiting factors lead to the conclusion that the rate reduction that could be realised without harming W+jets too much is going to be of another order of magnitude than the increase in rate due to lowering the p_{T} threshold, which was the original intention of the improved trigger. After reaching these conclusions, the development of the dijet veto trigger was halted.

Chapter 7

Lepton Trigger Efficiencies

7.1 Introduction

In the second part of this thesis, the focus lies on the triggers that are employed in the HNL analysis. Table 5.1 contains a full list of all the triggers. These are subdivided into single lepton triggers, dilepton triggers and trilepton triggers. The reason for using this many different triggers is that the signal region is covered as optimally as possible. The signal region consists of three tight leptons that pass the baseline event selection requirements discussed in the chapter on the HNL analysis. The applied p_{T} cuts were chosen as low as allowed by the triggers. In the analysis, simulated samples are used for a variety of purposes, from determining the expected HNL signal yield in the different signal region categories to predicting the backgrounds from several processes. The simulated events are put through a simulated version of the detector and the triggers, in order for them to be applicable and comparable to data. In the ideal case the simulated version behaves exactly like the real detector, however the simulation is not infallible and minor differences do appear. If the differences are significant, they have to be adjusted before application. This thesis aims to study the trigger efficiencies in data and simulation to see how they compare.

7.2 Methodology

7.2.1 MET primary dataset

The efficiency has to be measured in a dataset that has zero bias with reference to lepton triggers. A MET primary dataset is used for this purpose. The dataset contains events that have passed MET triggers, triggering on high missing transverse energy. The only SM source of MET are neutrinos. MET due to detector anomalies is removed as best as possible [72], but remains still a small source of high MET events. Neutrinos in the detector result from electroweak processes involving W and Z bosons. In decay of W, a lepton is also produced. Thus high MET events are often accompanied by leptons. In the signal region with three leptons, the two dominating SM processes will be WZ and $t\bar{t}$. A little more on this will follow in the section on results.

7.2.2 Simulation samples

Simulated events are again created using Monte Carlo techniques. The chosen process to simulate is WZ production. This type of event has the largest cross section for the final state with three leptons, making it ideal to study performance of the triggers. In the legends of the plots, WZ MC will always be referred to simply as 'Monte Carlo'.

7.2.3 Baseline event selection

The aim of this study is to look at the efficiency of MC and data in the actual signal region of the analysis. This means three tight leptons are selected in the same way as is done in the baseline event selection. The baseline p_{T} cuts are also implemented as they were described in section 5.4. The other conditions described in section 5.4 are however not applied as the goal is not to discriminate background versus signal. We would want to keep as many events in the selection in order to minimize statistical uncertainty. The MC events are all WZ and data consists of WZ and $t\bar{t}$ when three leptons are selected. These are the background events that are eliminated by the extra conditions on b-tags, M_{ll}, etcetera.

7.3 Results

7.3.1 Differences between Data and Simulation

It is first and foremost interesting to look at possible kinematic differences between the data and MC events. These can be important to explain phenomena and discrepancies later on. From here on, The plots in figure 7.1 show the number of b-quark jets that are tagged by the CSV algorithm, normalized to unity. The signal region is split according to the flavour of the channels. This results in 4 channels: $\mu\mu\mu$, $e\mu\mu$, $ee\mu$ and eee. It can be seen clearly that data contains generally more b-quark jets than WZ MC. This is a clear indication that $t\bar{t}$ processes are significant and that data is not purely dominated by WZ, otherwise it would look much more like WZ. The contribution of $t\bar{t}$ will lead to significant differences in the leading lepton p_{T} spectrum.

Figure 7.2 shows the p_{T} of the leading lepton in the event for both data and MC. The curves are again normalized to unity in order to be easily comparable. A significant difference between data and MC becomes apparent. MC, being pure WZ, has a softer p_{T} spectrum compared to data. This can be attributed to the fraction $t\bar{t}$ in data. A top-quark decays practically always into a W and a b-quark. Due to the high mass of

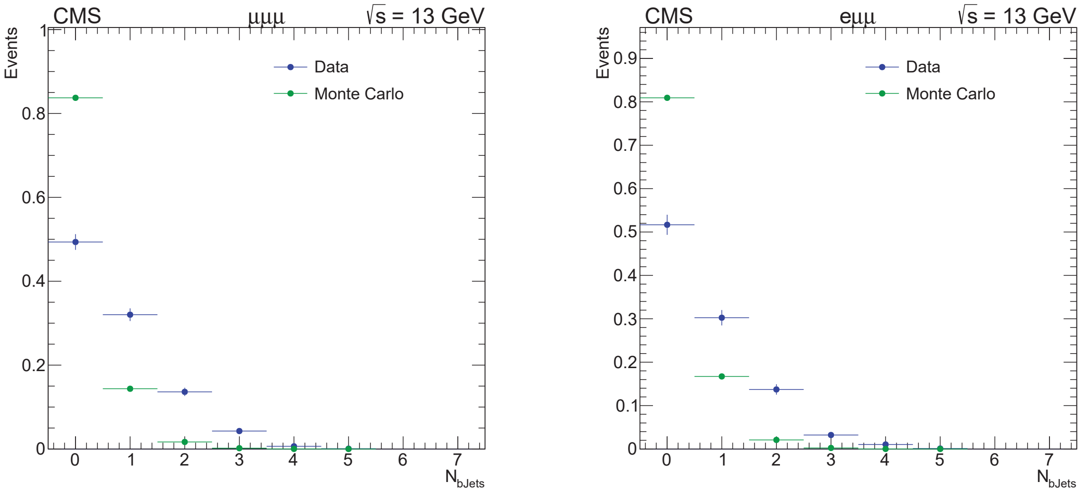

(a) Channel $\mu\mu\mu$ **(b)** Channel $e\mu\mu$

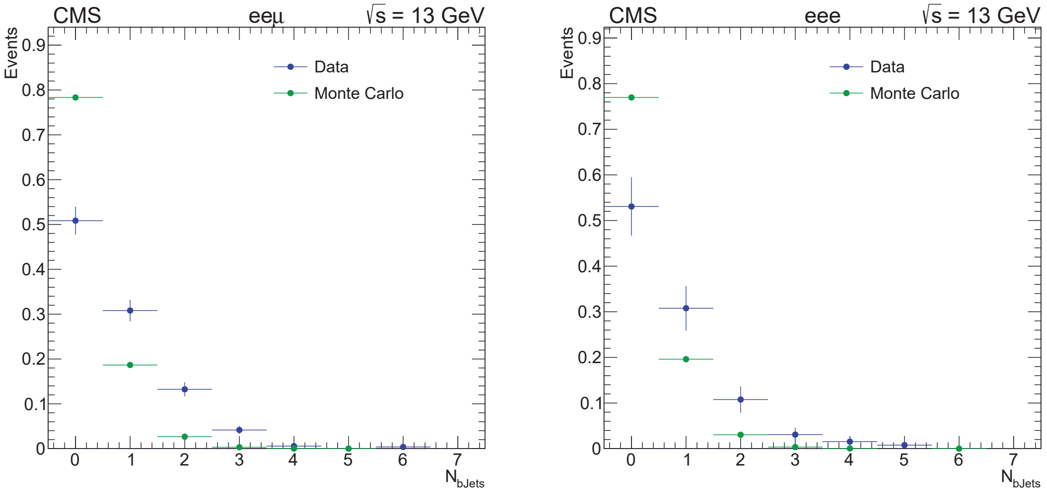

(c) Channel $ee\mu$ **(d)** Channel eee

Figure 7.1: The number of b-tagged jets in data and WZ MC. The four flavour channels are plotted separately.

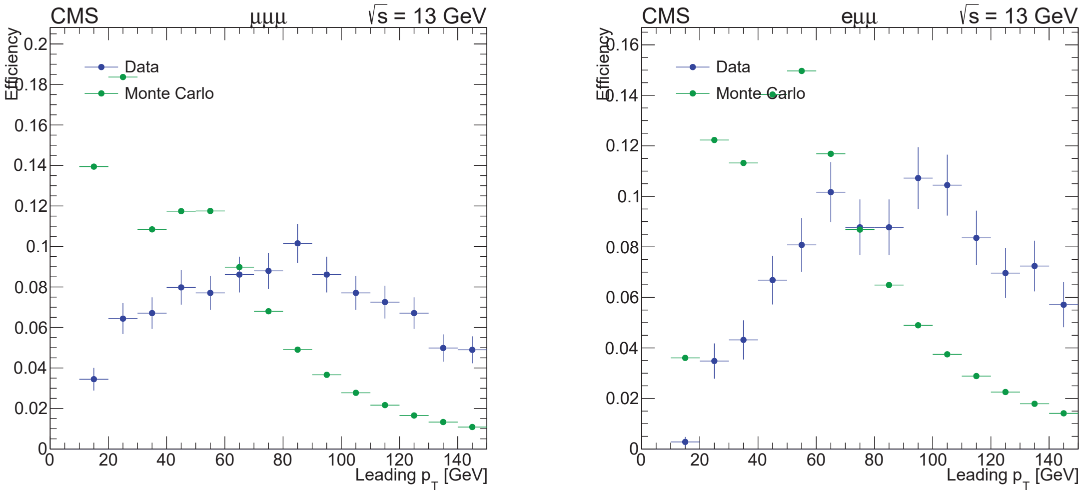

(a) Channel $\mu\mu\mu$ **(b)** Channel $e\mu\mu$

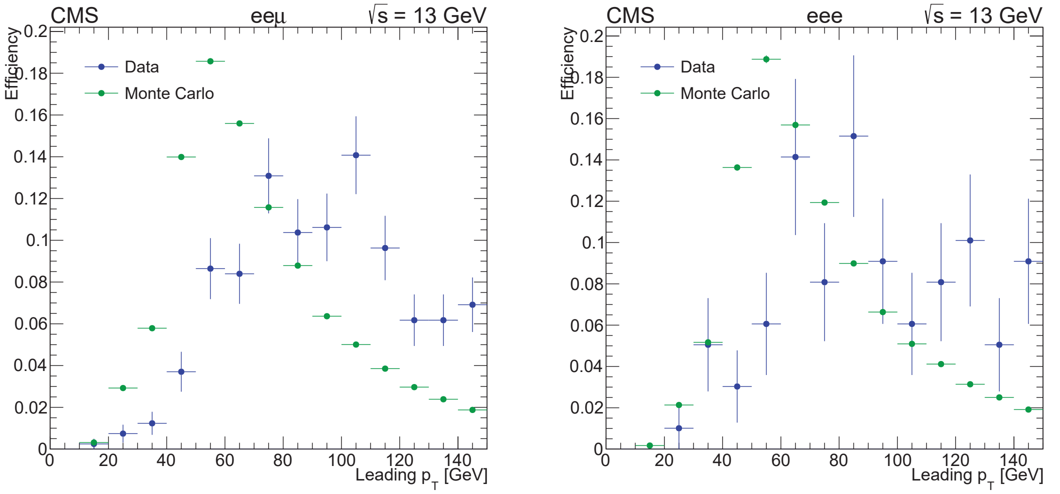

(c) Channel $ee\mu$ **(d)** Channel eee

Figure 7.2: p_{T} of the leading lepton in data and WZ MC. The four flavour channels are plotted separately.

the top, far above the W mass, the W boson can be quite boosted in the transverse momentum, meaning it has considerable p_{T} . In leptonic decay of the W, this can lead to high momentum leptons. The bosons in WZ processes can also be boosted, but not at the same energy the top quark can provide. This explains why the p_{T} spectrum in data is harder than in MC. It will be seen later that this has an effect on the trigger efficiencies.

As a last check, the trailing p_{T} spectrum is also plotted in figure 7.3 for data and MC. In all four channels, similar behavior is seen. The spectrum is peaked at $\sim 20, 25 GeV$. It can be noted that data shows a slightly harder spectrum than MC although it is not a large effect.

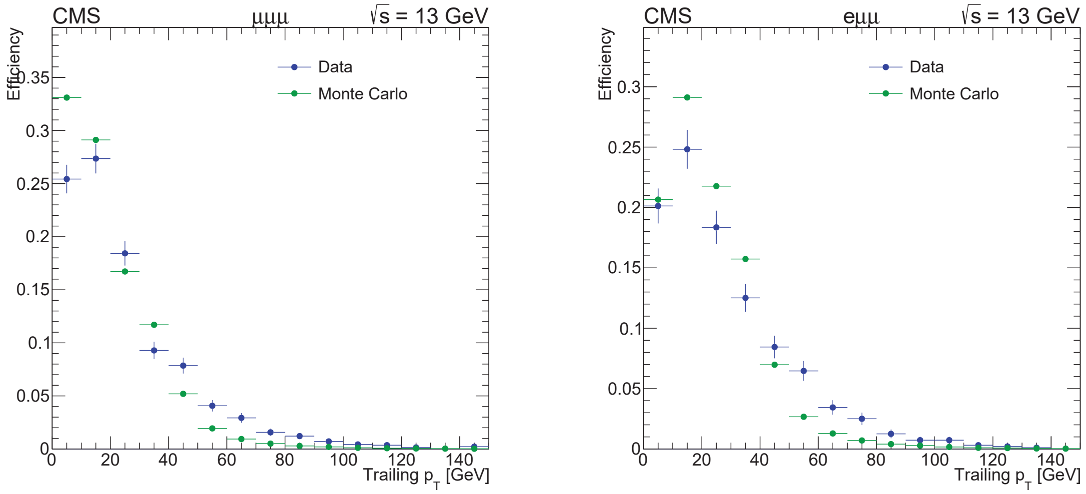

(a) Channel $\mu\mu\mu$ **(b)** Channel $e\mu\mu$

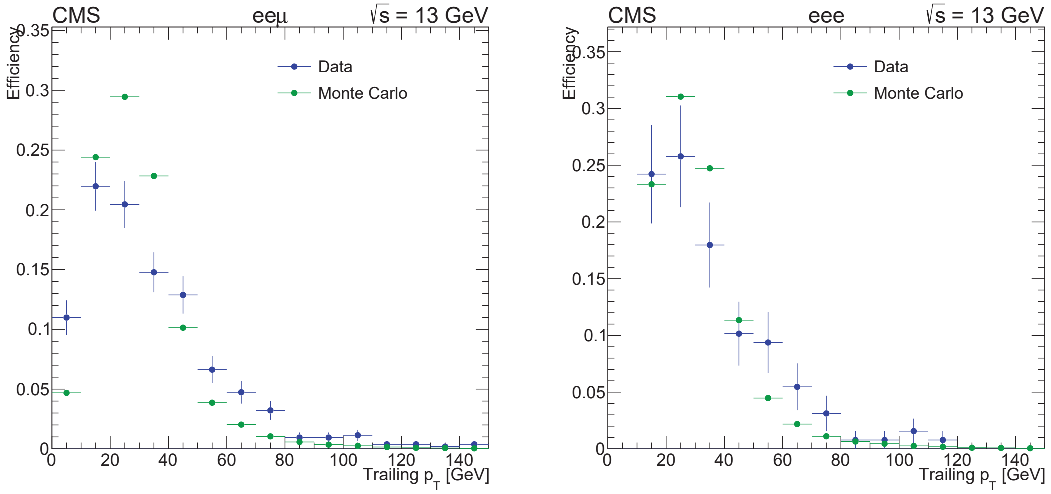

(c) Channel $ee\mu$ **(d)** Channel eee

Figure 7.3: p_{T} of the trailing lepton in data and MC. The four flavour channels are plotted separately.

7.3.2 Efficiency per channel

The full table of triggers can be found in 5.1. The full signal region is defined by using all triggers parallel, meaning if at least one of the triggers is passed, the event is included. As mentioned in the previous chapter, the efficiency of a trigger is the fraction of events that pass the trigger out of all events that, after offline reconstruction, fulfill the conditions set by that trigger.

The efficiency is studied separately for the low and high mass region of the signal region. A distinction based on flavour is also important as different trigger thresholds apply to electrons and muons. In all plots, the four channels will be studied. Lastly, the triggers themselves are subdivided in groups. The single lepton triggers are grouped together, as well as the dilepton triggers and the trilepton triggers. Essentially, the single lepton triggers cover the majority of the signal region and are supplemented by the dilepton and trilepton triggers to obtain even better coverage. Figure 7.4 shows the total efficiency in each channel. The top plots show the Single lepton trigger efficiency, followed by the dilepton and trilepton triggers. Finally, figure 7.5 shows the efficiency for all triggers combined.

It can be seen that the trigger efficiencies are everywhere higher in the high mass region than in the low mass region. This can simply be attributed to the higher p_{T} thresholds for leading, subleading and trailing leptons. Especially the condition on leading $p_{\mathrm{T}} > 55GeV$ makes for a big difference. This allows for the single lepton triggers to have efficiencies close to 1 already with only slight improvement by adding the di- and trilepton triggers. The MC efficiencies are always slightly higher than the data efficiencies in the high mass region, but for all triggers they match quite well, which is a sign that the simulation happens properly in this region.

In the low mass region, it is not expected that the efficiencies are as high as in the high mass region. Starting with the single lepton trigger efficiency, the values for data and MC do not match very well. For the eee channel, the statistics are unfortunately low, making it hard to draw decisive conclusions. The channel $ee\mu$ has lower uncertainties, although they are still of the order of the discrepancy between data and MC. The channels $e\mu\mu$ and $\mu\mu\mu$ suffer a lot less from bad statistics. MC efficiency is actually lower than for data in these channels. This can be explained by the leading p_{T} leptons from before. Looking in detail at these plots, it seems that the difference in spectra is way more significant for $e\mu\mu$ and $\mu\mu\mu$ than for the two others, which suffer from large uncertainties. The difference in the p_{T} spectra can explain the discrepancies seen here. For dilepton and trilepton triggers it can be seen that sometimes the efficiencies match a lot better, especially for $e\mu\mu$ and $\mu\mu\mu$. This results in the total trigger efficiency of figure 7.5a matching quite well for $\mu\mu\mu$. For $e\mu\mu$, there is a gap between both efficiencies, with MC being lower. The gap for eee is quite large, but could be attributed to the large statistical uncertainty.

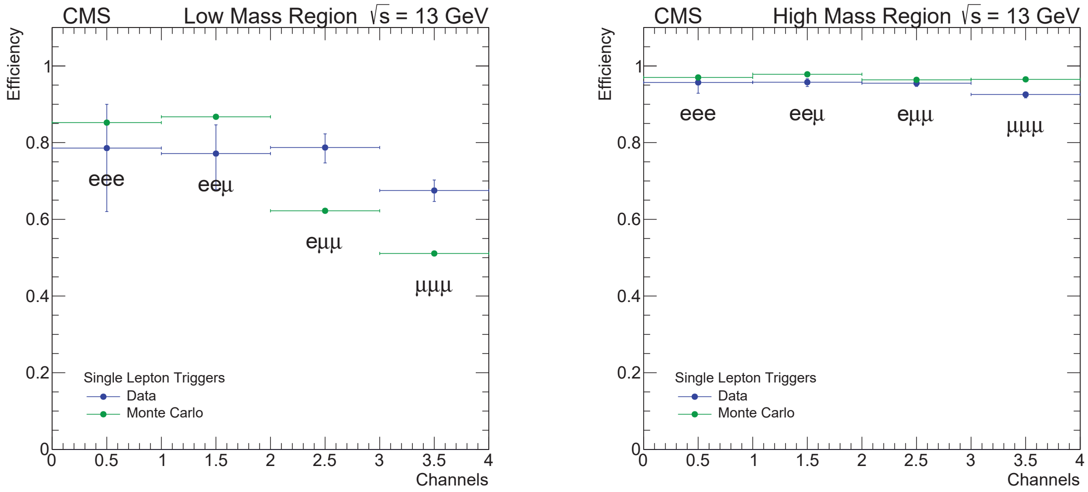

(a) Single lepton trigger efficiency **(b)** Single lepton trigger efficiency

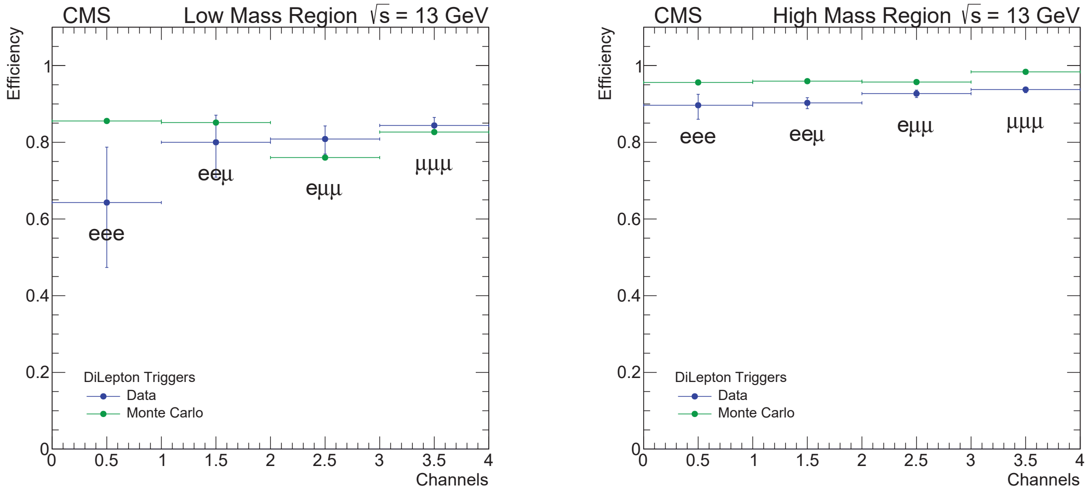

(c) Dilepton trigger efficiency **(d)** Dilepton trigger efficiency

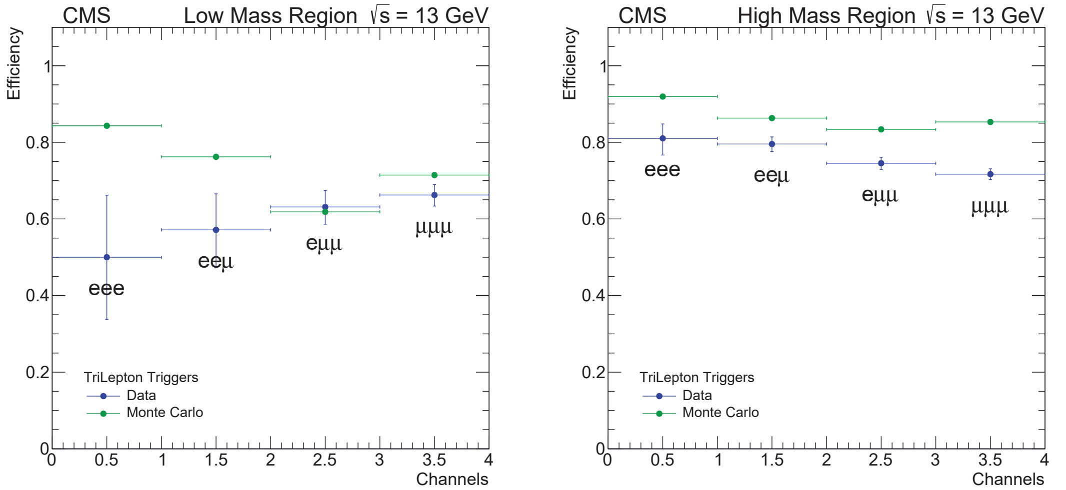

(e) Trilepton trigger efficiency **(f)** Trilepton trigger efficiency

Figure 7.4: Trigger efficiency of Single, Di- and Tri- lepton triggers combined. The total efficiency in each of the four channels is plotted.

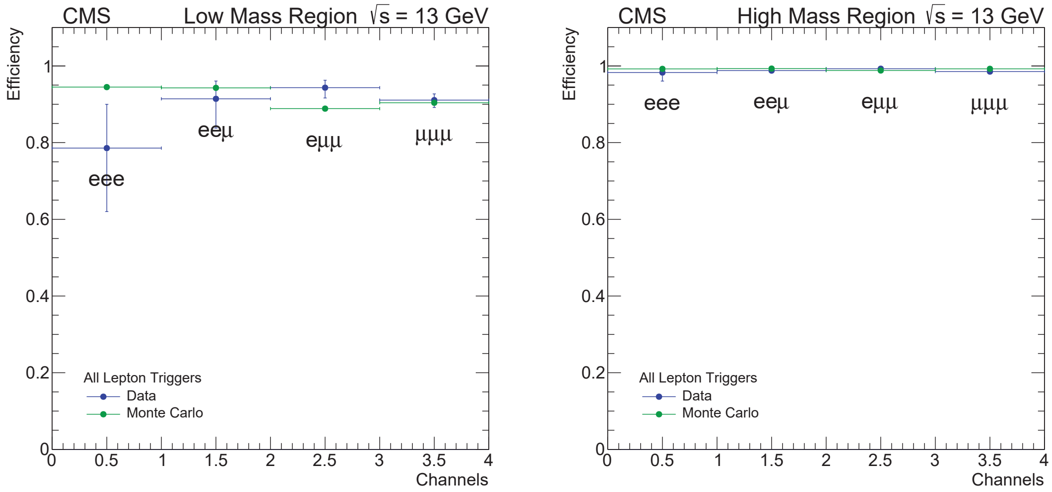

(a) All lepton triggers efficiency **(b)** All lepton triggers efficiency

Figure 7.5: Trigger efficiency of all the triggers combined. The total efficiency in each of the four channels is plotted.

7.3.3 Efficiency as a function of leading and trailing p_T

In a final step, it can be interesting to plot efficiencies as a function of leading and trailing lepton p_T . This way the turn on pattern of the triggers becomes apparent. Figures A.5 and A.6 show these for both the low and high mass regions plotted together. We only show the plots for the channel $\mu\mu\mu$ here as showing all four channels would be too elongated. The figures for the other three channels can be found in appendix A. In the leading p_T plots, the low and high mass region do not overlap as they are separated by this variable. In the trailing p_T plots however, new colors had to be introduced to distinguish the two mass regions. The trailing p_T plots show a higher efficiency at a certain momentum compared with the leading p_T plots. This is expected as when the trailing p_T reaches a certain value, this means there are already three leptons above this value on which can be triggered. The typical pattern can be recognized in all plots, around the trigger thresholds, the efficiency starts to rise and quickly reaches a saturation point in the vicinity of 1. It can be seen that there are discrepancies between data and MC, these are expected. They are mostly within reasonable bounds and as can be seen on figure A.6, when all triggers are combined, they match a lot better. This is mostly because the efficiency is close to one everywhere. If the efficiency is very good in both data and MC, discrepancies must vanish on their own. It can thus be assumed that the simulation manages to provide good results compared with actual data.

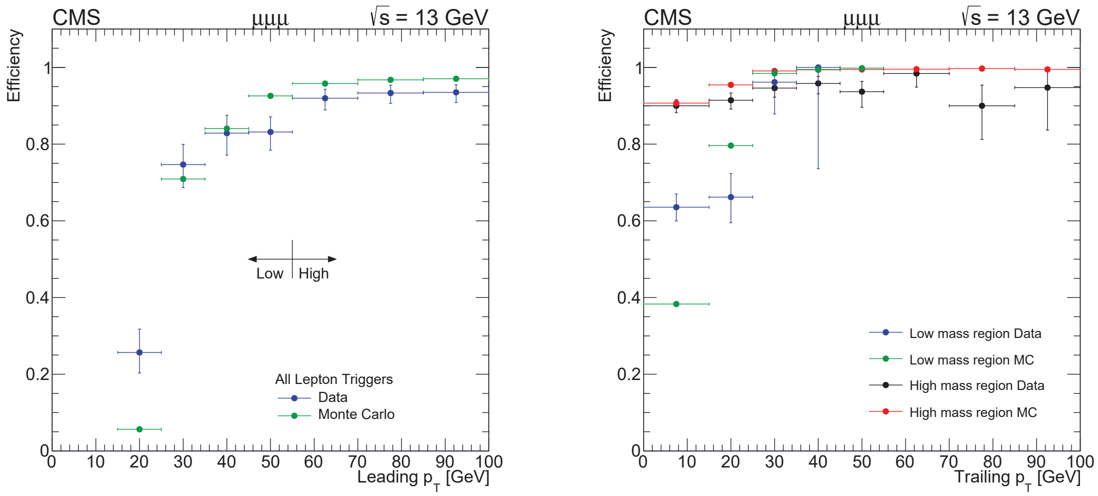

(a) Single lepton triggers in leading p_{T} **(b)** Single lepton triggers in trailing p_{T}

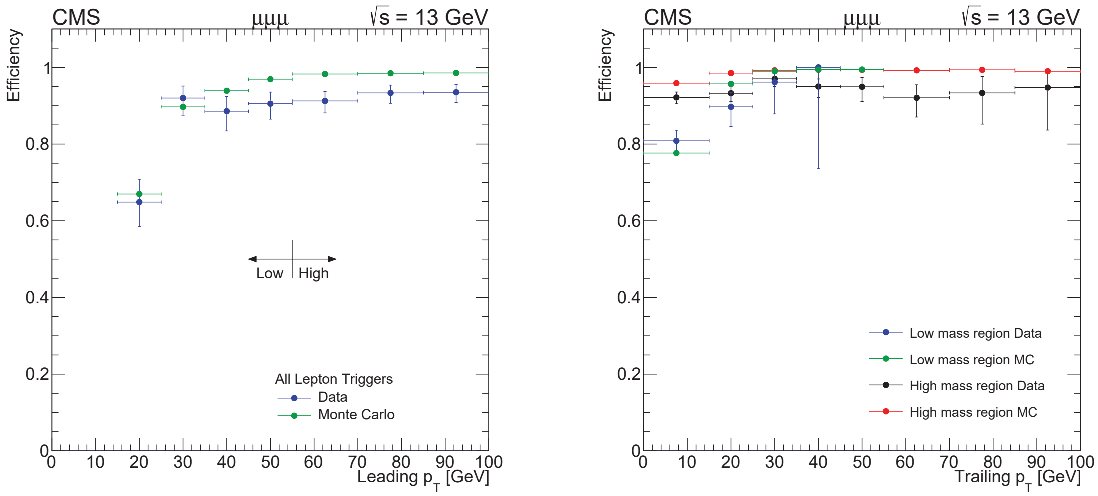

(c) Dilepton trigger efficiency **(d)** Dilepton trigger efficiency

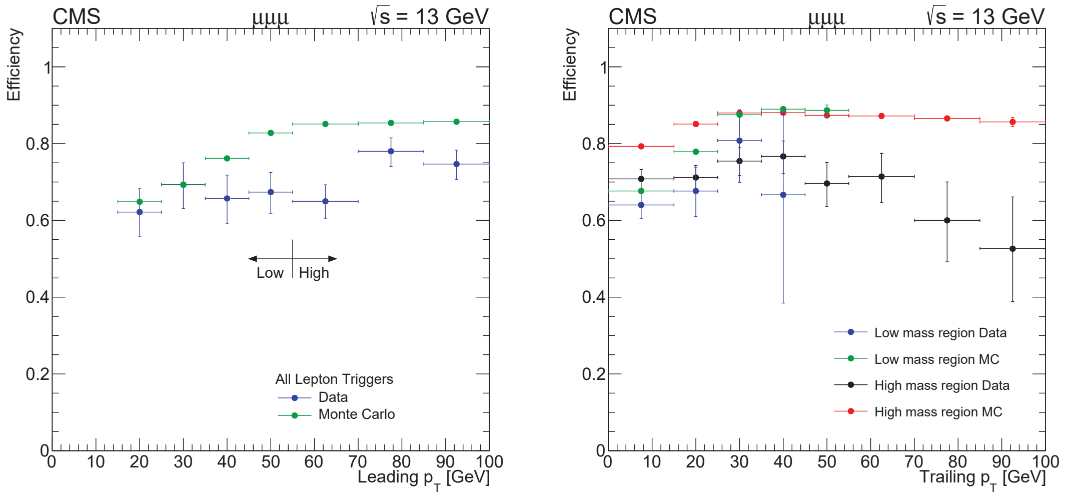

(e) Trilepton trigger efficiency **(f)** Trilepton trigger efficiency

Figure 7.6: Trigger efficiency of Single, Di- and Tri- lepton triggers combined. The efficiency is plotted as a function of leading and trailing p_{T} for the channel $\mu\mu\mu$.

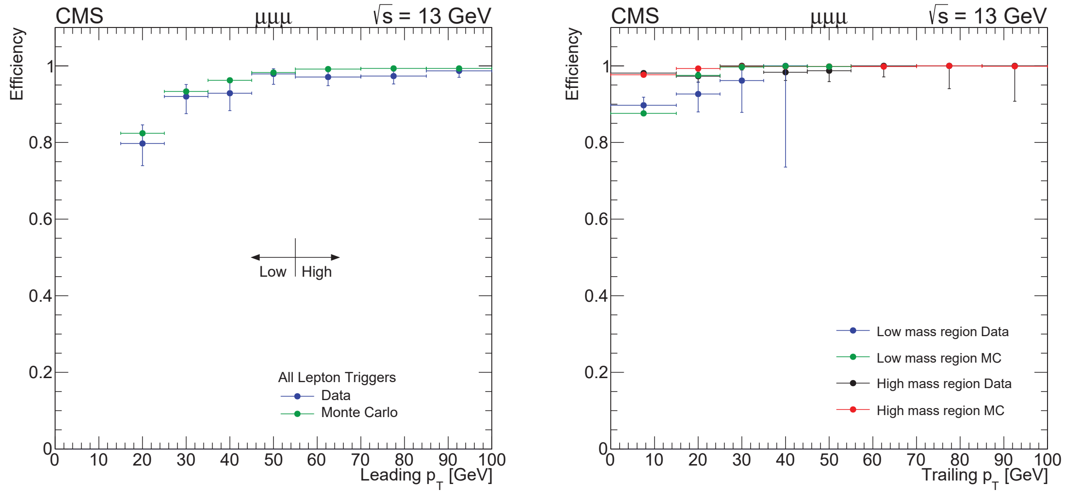

(a) All lepton triggers efficiency **(b)** All lepton triggers efficiency

Figure 7.7: Trigger efficiency of all triggers combined. The efficiency is plotted as a function of leading and trailing p_{T} for the channel $\mu\mu\mu$

7.4 Conclusion

To recapitulate, our aim was to verify that the simulated triggers manage to emulate the online triggers. The trigger efficiency is determined in a dataset based on MET triggers and MC events of the WZ process. The search region consists of three tight leptons that pass the baseline event selection. This was all discussed in chapter 5 at length. The channels are separated according to the flavours of the leptons. The low and high mass region are studied separately. Unless we have reached the plateau of maximum efficiency, discrepancies are expected between data and simulation. On one side because they do not consist of identical physical processes, MC being pure WZ and data being a mixture of different sorts of events, primarily WZ and $t\bar{t}$ (in the signal region). From the trigger efficiency plots data and MC seem to match rather well, although there are small discrepancies: in most cases, the efficiency in MC is slightly larger than in data. But when all triggers are combined these are relatively small and it seems that the simulation samples can be applied to data without a scale factor.

Chapter 8

Conclusion

This thesis was executed as a part of the CMS Collaboration at CERN, Geneva. The experimental particle physics group at the UGent has been researching heavy neutral leptons using the LHC with emphasis on the Majorana neutrino explanation. The nature of this analysis has led to high relevance for the triggers that are used. Two distinct studies have been performed in this thesis regarding the triggers. Firstly a new idea was tested that might have been able to lower the p_T threshold of the single electron and muon triggers. Due to the increased luminosity, these thresholds will be elevated. The idea, although it unfortunately did not work, was to try and exclude QCD dijet events in favor of W+jets and Majorana neutrino signal events by vetoing events with a single lepton and a jet exactly opposite to one another. It turned out that in this way, indeed a larger fraction of fake events from QCD could be excluded than from W+jets. The rate of the trigger could thus be reduced, but the cost was that the efficiency of real leptons from e.g. W+jets was lowered significantly, ultimately leading to the conclusion that the new trigger was not feasible and would not be pursued further.

In the second part, the triggers that were already used in the analysis were studied. A variety of triggers is used because of the compressed p_T spectra of the leptons in the signal process. The triggers require a dedicated study of their efficiency as it is important to know the coverage of the signal region. The efficiencies of data and MC are compared to each other. In the ideal case the MC simulated detector and triggers provide similar physics as the actual data. In reality there are often differences in the efficiencies between data and simulation. It is seen that e.g. when only the single lepton triggers are studied, that the discrepancies can become large. Here they can be attributed to the different p_T spectrum in data and simulation. For only the dilepton or only the trilepton triggers the difference is large in some cases. But when all triggers are combined the efficiency approaches one everywhere. It is seen that the small fraction of events that does not pass the triggers when it should are events with low p_T leptons as expected. It can be concluded that no correction is necessary for simulated events.

Chapter 9

Extended Abstract

The nature of neutrinos is one of the most compelling unanswered questions in physics. Due to being such an elusive particle, it is not yet determined if it is a Dirac fermion like all other fundamental Standard Model (SM) particles, or if it is in fact a Majorana fermion, in which case it could be the solution to several existing problems that the SM currently has no answers for. The Large Hadron Collider (LHC) [28] at CERN, Geneva, is the largest particle accelerator in the world and produces proton-proton collisions at an unprecedented centre-of-mass energy, currently reaching $13\,TeV$. It provides the experimental means to study the nature of the neutrino.

This thesis is carried out in function of the Heavy Neutral Lepton (HNL) analysis performed by the UGent experimental particle physics group [62], in collaboration with the Compact Muon Solenoid (CMS) experiment[30], one of the four detectors at the LHC. If the neutrinos are of Majorana nature, it would come with heavy sterile neutrino partners in certain scenarios [27]. The Majorana analysis studies collisions that produce three leptons, a signature where the heavy neutral lepton (HNL) would also contribute.

An essential part of experiments at the LHC are the triggers [51]. Triggers are the online data selection mechanism that CMS employs. They are explained further on. This dissertation contains two separate trigger studies. First, an analysis is made of a new idea for a trigger using a back-to-back veto. In the second part, the triggers used by the Majorana analysis are studied in detail.

The CMS Trigger system consists of 2 levels, the Level 1 (L1) trigger [51] and the High-Level trigger (HLT) [52]. They bring the collision rate down from $40MHz$ to approximately $1kHz$ of interesting physics events. L1 is the first step which brings the rate down to $100kHz$. Due to the very limited amount of processing time, it is mostly based on hardware electronics designed to make rough reconstructions of physics objects and fast decisions based on a menu of events that are wanted by physics analysis groups. The HLT system is a server farm of several thousand commercial computers. They execute a more thorough reconstruction, which is similar to the actual reconstruction that happens offline. They reduce the rate to the final $1kHz$.

The idea for a new trigger is motivated by the increase of the momentum threshold of the single lepton triggers at CMS in 2017. The thresholds are raised to account for the increase in luminosity, which will result in a higher interaction rate and thus an increase of events passing the trigger. Instead of raising the p_{T} threshold of the triggers, a new idea is proposed where instead back-to-back events are excluded in the single lepton triggers. To clarify, back-to-back events entail events with a lepton and a jet that are emitted back-to-back in the detector. The physical motivation for this is that it would eliminate a large fraction of fake or non-prompt leptons originating from QCD dijet events, while at the same time not harming important physics signals e.g. W+jets. This idea is thoroughly studied for muons and electrons. The veto is analyzed in minimum bias data sets [64] that represent (almost) random events in the CMS detector and W+jets Monte Carlo (MC) samples, that represent the type of process that we do not want to harm. Ultimately, it is decided that, although fake or non-prompt leptons are more efficiently excluded than W+jets, it does not seem feasible to design a back-to-back veto trigger that would reduce the rate considerably while keeping W+jets relatively intact. The p_{T} threshold could not be lowered considerably, therefore the idea was concluded.

In the second part of this dissertation, the HLT triggers used in the HNL analysis [62] are studied. A variety of triggers are used to provide the signal region where HNL signals can be sought. It consists of a mixture of single lepton, dilepton and trilepton triggers that all help to cover part of the parameter space of the HNL signal. The aim of the study is to make sure that the efficiency of the triggers in the signal region is high and that the efficiencies in data and simulation match well enough. If they do not match, corrections might need to be applied to simulation before they can be used correctly. To recapitulate, the signal region consists of three leptons, on which several conditions are imposed to make a stringent selection. The efficiency of the triggers are studied in a MET primary dataset and WZ MC. It is seen that when looking at e.g. all single lepton triggers or all di- or trilepton triggers combined, there are some discrepancies in the efficiencies between data and simulation. In some places this can be attributed to low statistics or low efficiency. When combining all triggers, it can be seen that the total efficiency reaches the plateau and the discrepancies between data and MC vanish almost everywhere. This is a good sign, the signal region is covered and no scale factor is necessary for simulation.

Bibliography

[1] SNO Collaboration, *The Sudbury Neutrino Observatory*, arXiv:1602.02469

[2] C. W. Walter, *The Super-Kamiokande experiment*, arXiv:0802.1041

[3] https://home.cern/

[4] S. F. Novaes, *Standard Model: An Introduction*, (2000), Proceedings of the X J. A. Swieca Summer School, arXiv:hep-ph/0001283

[5] H. Nicolai, *Quantum Gravity: the view from particle physics*, (2013), arXiv:1301.5481

[6] X. Calmet, *A review of Quantum Gravity at the Large Hadron Collider*, (2010), Mod. Phys. Lett. A25:1553-1579, arXiv:1005.1805

[7] F. Englert and R. Brout, *Broken Symmetry and the Mass of Gauge Vector Mesons*, (1964), Phys. Rev. Lett. 13(9) 321-323

[8] P. Higgs, *Broken Symmetries and the Masses of Gauge Bosons*, (1964), Phys. Rev. Lett. 13(16) 508-509

[9] Particle Data Group, http://pdg.lbl.gov/

[10] CMS Collaboration, *Observation of a new particle in the search for the Standard Model Higgs boson with the ATLAS detector at the LHC*, Phys. Lett. B 716 (2012) 1, doi:10.1016/j.physletb.2012.08.020, arXiv:1207.7214.

[11] CMS Collaboration, *Observation of a new boson at a mass of 125 GeV with the CMS experiment at the LHC*, Phys. Lett. B 716 (2012) 30, doi:10.1016/j.physletb.2012.08.021, arXiv:1207.7235.

[12] Mark Thomson, *Modern Particle Physics*

[13] Alessandro Bettini, *Introduction to Elementary Particle Physics*, 2nd edition

[14] Franz Mandl, Graham Shaw, *Quantum Field Theory*, 2nd edition

[15] S. Oshima, S. Kanemaki and T. Fujita, *Problems of Real Scalar Klein-Gordon Field*, (2005), arXiv:hep-th/0512156

[16] P. A. M. Dirac, *The Quantum Theory of the Electron*, Proceedings of the Royal Society, vol.117 (1928) 778

[17] E. Majorana, *A Symmetric Theory of Electrons and Positrons*, Il Nuovo Cimento, vol.14 (1937) 171-184

[18] R. P. Feynman, *Space-Time Approach to Quantum Electrodynamics*, Phys. Rev. 76 (1949) 769

[19] The LEP Collaborations, *A Combination of Preliminary Electroweak Measurements and Constraints on the Standard Model*, (2006) CERN-PH-EP/2006-042

[20] S. Weinberg, *A Model of Leptons*, Phys. Rev. Lett. vol. 19 n.21 (1967)

[21] F. J. Hasert et al., *Observation of neutrino-like interactions without muon or electron in the Gargamelle neutrino experiment*, Phys. Lett. 46B (1973) 138

[22] F. J. Hasert et al., *Search for elastic muon-neutrino electron scattering*, Phys. Lett. 46B (1973) 121

[23] C. S. Wu *et al.*, *Experimental Test of Parity Conservation in Beta Decay*, (1957) Phys. Rev. 105, 1413

[24] G. C. Nayak, *General Form of Color Charge of the Quark*, (2012), Eur. Phys. J. C. 73:2442

[25] LHCb collaboration, *Observation of $J/\psi p$ resonances consistent with pentaquark states in $\Lambda_b^0 \to J/\psi K^p$ decays*, (2015), *Phys. Rev. Lett.* 115, 072001

[26] C. Jarlskog, *On particle-antiparticle mirror symmetry*, (1989), Int. J. of Quantum Chemistry, vol. 35, n.6, p.769-778

[27] E. Franco, *Type I+III Seesaw Mechanism and CP Violation for Leptogenesis*, (2015), Phys. Rev. D 92, 113010, arXiv:1510.06240

[28] Lyndon Evans and Philip Bryant, *LHC Machine*, (2008), JINST 3 S08001

[29] O. Brüning and P. Collier, *Building a behemoth*, Nature 448, 285-289, (2007)

[30] CMS Collaboration, S Chatrchyan *et al.*, *The CMS experiment at the CERN LHC*, (2008), JINST 3 S08004

[31] S. Myers and E. Picasso, *The design, construction and commissioning of the CERN large Electron-Positron collider*, (1990), Contemporary Physics, vol.31 issue 6 387-403

[32] R. Perin, *The superconducting magnet system for the LHC*, (1991), IEEE Transactions on Magnetics, vol.27 issue2 1735-1742

[33] https://home.cern/about/accelerators/linear-accelerator-2

[34] https://home.cern/about/accelerators/proton-synchrotron-booster

[35] https://home.cern/about/accelerators/proton-synchrotron

[36] https://home.cern/about/accelerators/super-proton-synchrotron

[37] https://home.cern/about/engineering/radiofrequency-cavities

[38] M. J. Barnes et al., *Injection and extraction magnets: kicker magnets*, (2011), CERN-2010-004, arXiv:1103.1583

[39] D. E. Soper, *Parton Distribution Functions*, (1997), Nucl. Phys. B, vol.53 issue 1-3 69-80

[40] R. Bailey and P. Collier, *Standard Filling Schemes for Various LHC Operation Modes*, (2003), LHC-PROJECT-NOTE-323

[41] https://twiki.cern.ch/twiki/bin/view/CMSPublic/LumiPublicResults#2016_Proton_Proton_13_TeV_Collis

[42] https://home.cern/about/experiments/atlas

[43] CMS Collaboration, *Precise Mapping of the Magnetic Field in the CMS Barrel Yoke using Cosmic Rays*, (2010), JINST 5 T03021

[44] M. Mannelli et al., *The CMS tracker system project*, (1997), CMS-TDR-5

[45] CMS Collaboration, *The CMS electromagnetic calorimeter project: Technical Design Report*, (1997), CMS-TDR-4

[46] CMS Collaboration, *The CMS hadron calorimeter project: Technical Design Report*, (1997), CMS-TDR-2

[47] CMS Collaboration, *The CMS muon project: Technical Design Report*, (1997), CMS-TDR-3

[48] CMS Collaboration, D. J. Lange, *The CMS Reconstruction Software*, (2011), Journal of Physics: Conference Series vol.331 n.3

[49] CMS Collaboration, *Particle-Flow Event Reconstruction in CMS and performance for Jets, Taus and* E_T^{miss}, CMS Physics Analysis Summary(PAS) PFT-09-001

[50] https://twiki.cern.ch/twiki/bin/viewauth/CMS/GlobalTriggerAvailableMenus

[51] CMS Collaboration, *The CMS trigger system*, (2017), CMS-TRG-12-001

[52] CMS Collaboration, *The CMS High level trigger*, Eur. Phys. J. C 46 (2006) 605

[53] G. Bauer et al., *Recent experience and future evolution of the CMS High Level Trigger System*, (2012), Real Time Conference, 18th IEEE-NPSS

[54] CMS Collaboration, *Commissioning of the CMS High-Level Trigger with cosmic rays*, JINST 5 (2010) T03005

[55] D. Hufnagel, *CMS Tier-0: Preparing for the future*, Journal of Physics: Conference Series, vol. 396 part 2

[56] CMS Collaboration, *Search for heavy Majorana neutrinos in mu+mu+[mu-mu-]+jets and e+e+[e-e-]+jets events in pp collisions at sqrt(s) = 7 TeV*, Phys. Lett. B 717 (2012) 109, arXiv:1207.6079

[57] CMS Collaboration, *Search for heavy Majorana neutrinos in mu+/- mu+/- + jets events in proton-proton collisions at sqrt(s) = 8 TeV*, Phys. Lett. B 748 (2015) 144, arXiv:1501.05566

[58] ATLAS Collaboration, *Search for heavy Majorana neutrinos with the ATLAS detector in pp collisions at* $\sqrt{s} = 8$ *TeV*, JHEP 1507 (2015) 162, arXiv:1506.06020

[59] CMS Collaboration, *Search for new physics with same-sign isolated dilepton events with jets and missing transverse energy at the LHC*, JHEP 1106, 077 (2011), arXiv:1104.3168

[60] CMS Collaboration, *Search for new physics in events with same-sign dileptons and b-tagged jets in pp collisions at sqrt(s) = 7 TeV*, JHEP 1208, 110 (2012), arXiv:1205.3933

[61] J. Almond *et al.*, *Search for Heavy Majorana Neutrinos in Events with Same-Sign e,μ Lepton Pairs in pp Collisions at* $\sqrt{s} = 8TeV$, (2015), CMS AN-15-050

[62] D. Dobur *et al.*, *Search for heavy neutral leptons in multi-lepton final states using proton-proton collision data collected at* $\sqrt{s} = 13TeV$, (2017), CMS AN-17-014

[63] CMS Collaboration, *Zero bias and HF-based minimum bias triggering for pp collisions at 14 TeV in CMS*, (2007), CMS-PAS-QCD-07-002

[64] Yuan Chao, *Minimum-Bias and Underlying Event Studies at CMS*, (2008), arXiv:0810.4819

[65] CMS Collaboration, *Measurement of inclusive W and Z boson production cross sections in pp collisions at* $\sqrt{s} = 8$ *TeV*, (2014), CERN-PH-EP/2013-217

[66] L. Mastrolorenzo, *The CMS Level-1 Tau identification algorithm for the LHC Run II*, (2016), Nuclear and Particle Physics Proceedings, vol. 273-275 p. 2518-2520

[67] CMS Collaboration, *CMS L1 tau trigger performance in 2016 data*, (2016), CMS DP-2016/021

[68] W. Bonivento et al., *Proposal to Search for Heavy Neutral Leptons at the SPS*, (2013), arXiv:1310.1762

[69] https://twiki.cern.ch/twiki/bin/view/CMS/MuonPOG

[70] https://twiki.cern.ch/twiki/bin/view/CMS/MultivariateElectronIdentificationRun2

[71] CMS Collaboration, *Identification of b-quark jets with the CMS experiment*, (2013), CMS-BTV-12-001, arXiv:1211.4462

[72] CMS Collaboration, *Performance of the CMS missing transverse momentum reconstruction in pp data at* $\sqrt{s} = 8TeV$, (2015), CMS-JME-13-003, arXiv:1411.0511

1

Appendices

Appendix A

Single, Di- and Trilepton Trigger Efficiencies for the HNL analysis.

This appendix contains the trigger efficiency plots for the channels $e\mu\mu$, $ee\mu$ and eee as a function of leading and trailing p_{T}. In section 7.3.3 they were discussed for the channel $\mu\mu\mu$ but since similar arguments apply to all channels, the other channels are put here for information.

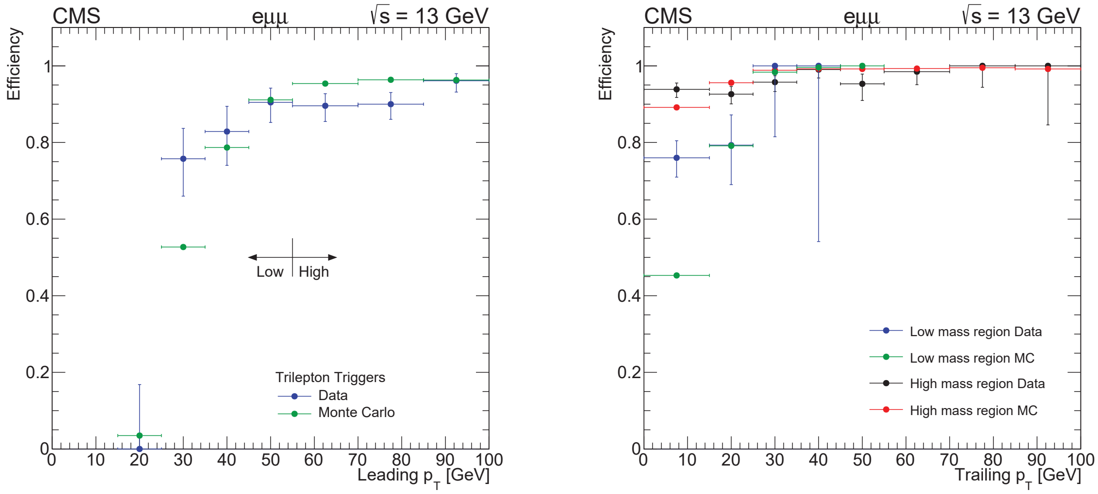

(a) Single lepton triggers in leading p_T **(b)** Single lepton triggers in trailing p_T

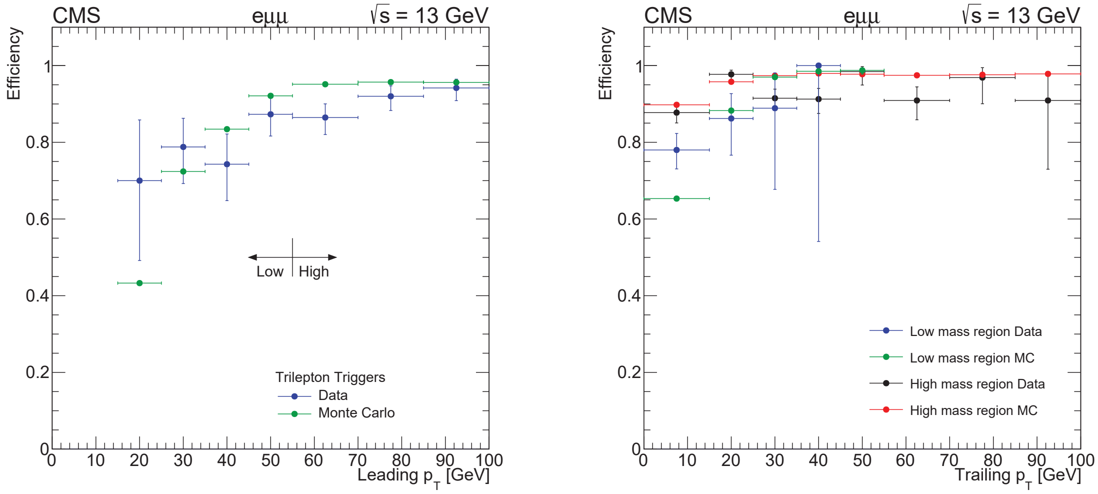

(c) Dilepton trigger efficiency **(d)** Dilepton trigger efficiency

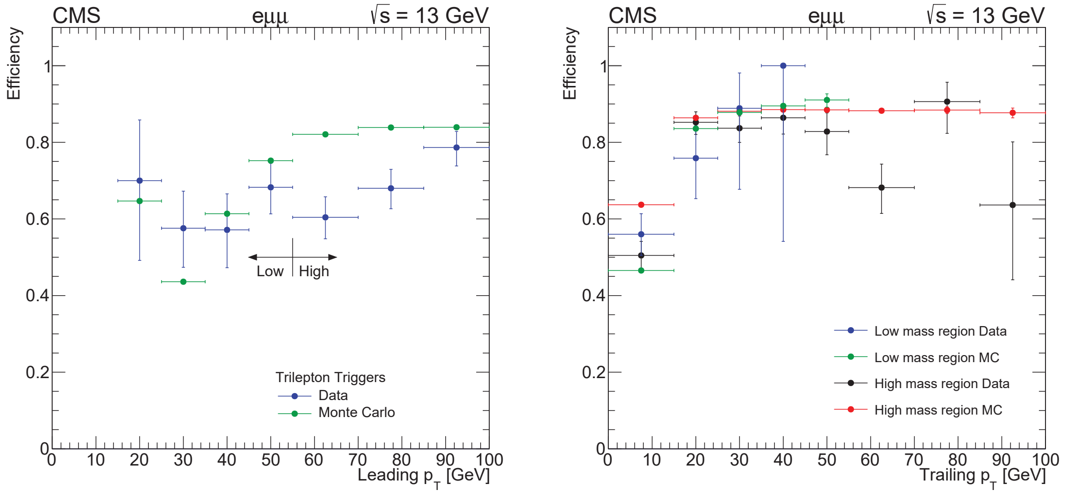

(e) Trilepton trigger efficiency **(f)** Trilepton trigger efficiency

Figure A.1: Trigger efficiency of Single, Di- and Tri- lepton triggers combined. The efficiency is plotted as a function of leading and trailing p_T for the channel $e\mu\mu$.

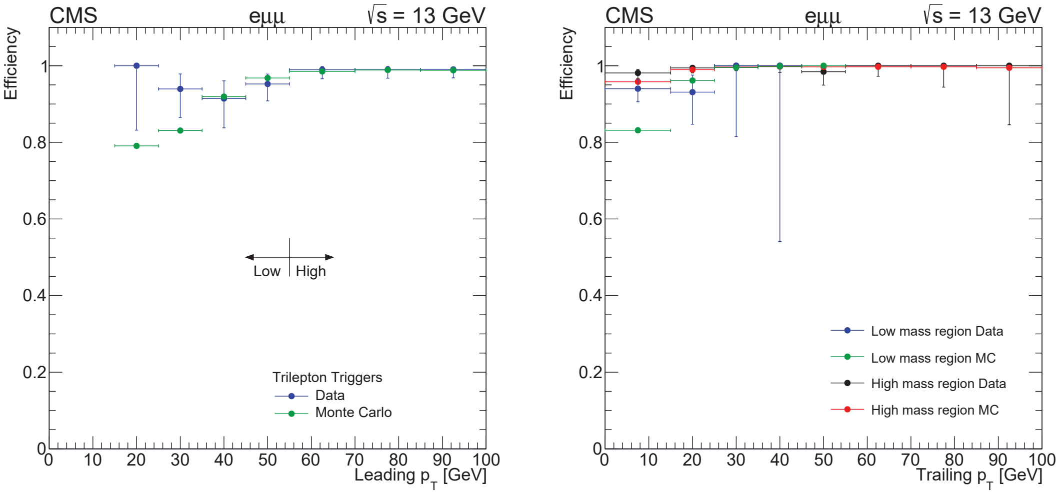

(a) All lepton triggers efficiency

(b) All lepton triggers efficiency

Figure A.2: Trigger efficiency of all the triggers combined. The efficiency is plotted as a function of leading and trailing p_{T} for the channel $e\mu\mu$.

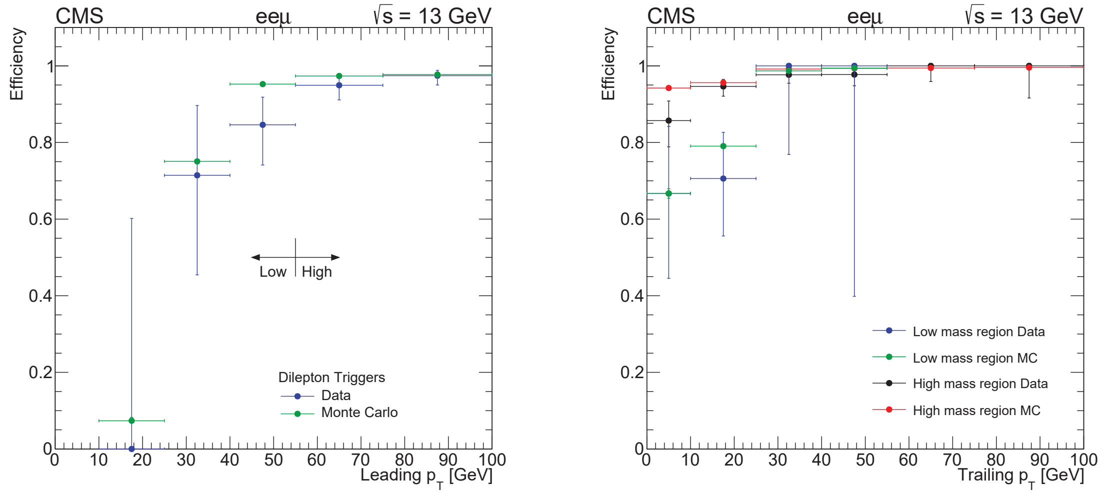

(a) Single lepton triggers in leading p_{T} **(b)** Single lepton triggers in trailing p_{T}

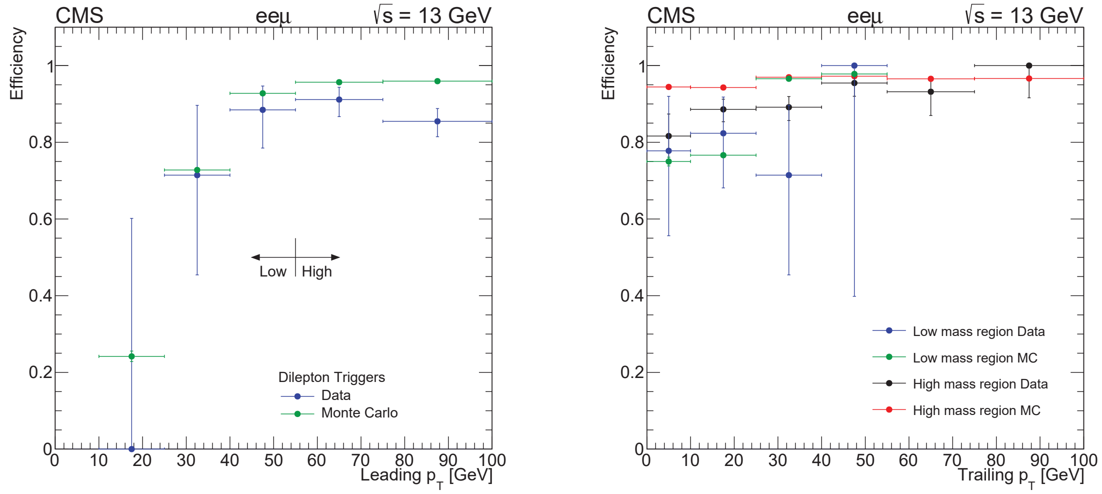

(c) Dilepton trigger efficiency **(d)** Dilepton trigger efficiency

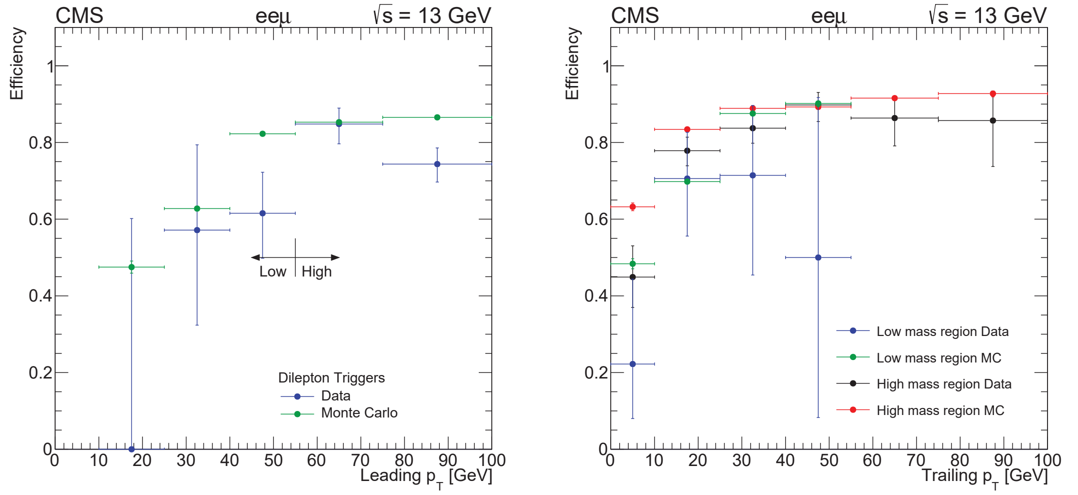

(e) Trilepton trigger efficiency **(f)** Trilepton trigger efficiency

Figure A.3: Trigger efficiency of Single, Di- and Tri- lepton triggers combined. The efficiency is plotted as a function of leading and trailing p_{T} for the channel $ee\mu$.

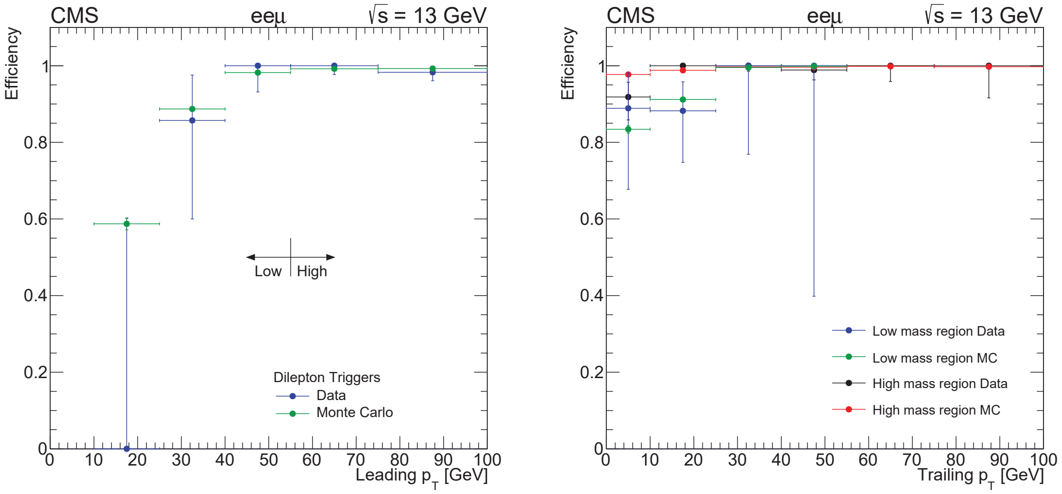

(a) All lepton triggers efficiency

(b) All lepton triggers efficiency

Figure A.4: Trigger efficiency of all the triggers combined. The efficiency is plotted as a function of leading and trailing p_{T} for the channel $ee\mu$.

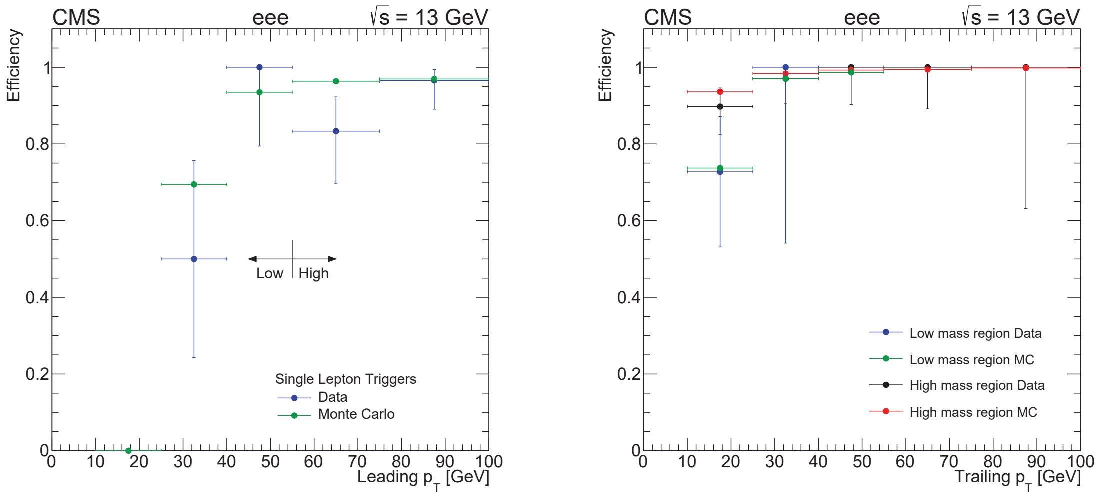

(a) Single lepton triggers in leading p_{T} **(b)** Single lepton triggers in trailing p_{T}

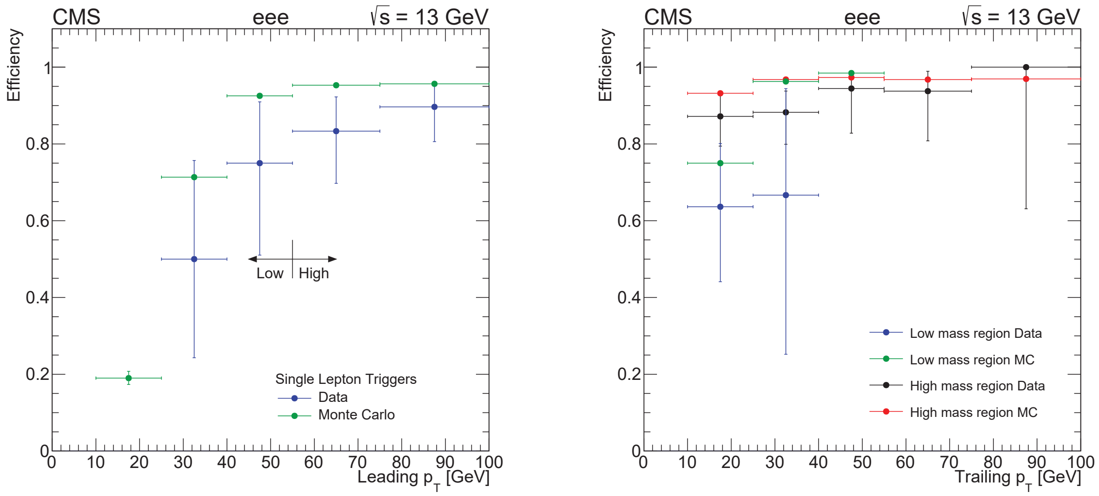

(c) Dilepton trigger efficiency **(d)** Dilepton trigger efficiency

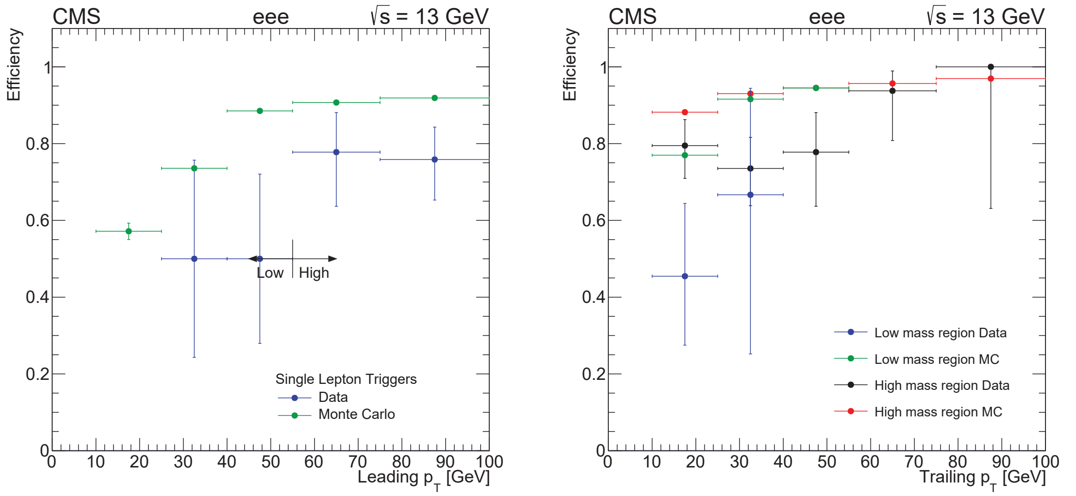

(e) Trilepton trigger efficiency **(f)** Trilepton trigger efficiency

Figure A.5: Trigger efficiency of Single, Di- and Tri- lepton triggers combined. The efficiency is plotted as a function of leading and trailing p_{T} for the channel *eee*.

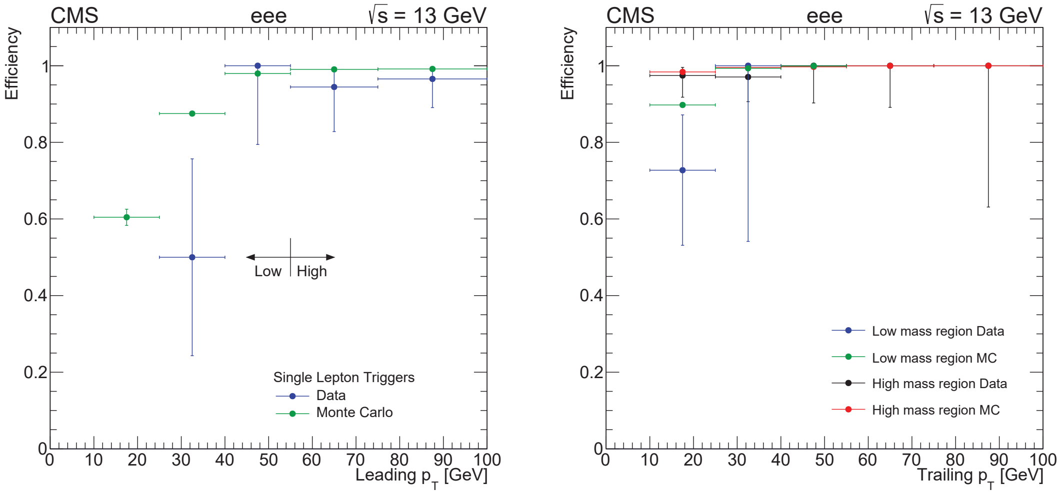

(a) All lepton triggers efficiency **(b)** All lepton triggers efficiency

Figure A.6: Trigger efficiency of all the triggers combined. The efficiency is plotted as a function of leading and trailing p_{T} for the channel eee.